Title	Spatiotemporal evolution of magmatic pulses and regional metamorphism during a Cretaceous flare-up event: Constraints from the Ryoke belt (Mikawa area, central Japan)
Author(s)	Takatsuka, Kota; Kawakami, Tetsuo; Skrzypek, Etienne; Sakata, Shuhei; Obayashi, Hideyuki; Hirata, Takafumi
Citation	Lithos (2018), 308–309: 428-445
Issue Date	2018-05
URL	http://hdl.handle.net/2433/231107
Right	© 2018. This manuscript version is made available under the CC-BY-NC-ND 4.0 license http://creativecommons.org/licenses/by-nc-nd/4.0/ The full-text file will be made open to the public on 01 May 2020 in accordance with publisher's 'Terms and Conditions for Self-Archiving'.This is not the published version. Please cite only the published version. この論文は出版社版でありません。引用の際には出版社版をご確認ご利用ください。
Type	Journal Article
Textversion	author

Spatiotemporal evolution of magmatic pulses and regional metamorphism during a Cretaceous flare-up event: constraints from the Ryoke belt (Mikawa area, central Japan)

Kota Takatsuka[1], Tetsuo Kawakami[1,*], Etienne Skrzypek[1], Shuhei Sakata[1, 2], Hideyuki Obayashi[1], Takafumi Hirata[1,†]

[1]Department of Geology and Mineralogy, Graduate School of Science, Kyoto University, Kitashirakawa-Oiwake-cho, Sakyo-ku, Kyoto 606-8502, Japan

[2]Department of Chemistry, Faculty of Science, Gakushuin University, 1-5-1 Mejiro, Toshima-ku, Tokyo 171-8588, Japan

*Corresponding author: T. Kawakami (e-mail: t-kawakami@kueps.kyoto-u.ac.jp)

[†]Present address: Geochemical Research Center, Graduate School of Science, The University of Tokyo, 7-3-1 Hongo, Bunkyo-ku, Tokyo 113-0033, Japan

Abstract

The spatiotemporal relationship between granitoid intrusions and low-pressure/temperature type regional metamorphism in the Ryoke belt (Mikawa area) is investigated to understand the tectono-thermal evolution of the upper- to middle-crust during a Cretaceous flare-up event at the Eurasian active continental margin. Three plutono-metamorphic stages are recognized; (1) 99−84 Ma: intrusion of granitoids (99−95 Ma pulse) into the upper crust and high-*T* regional metamorphism reaching sillimanite-grade (97.0 ± 4.4 Ma to 88.5 ± 2.5 Ma) in the middle crust, (2) 81−75 Ma: intrusion of gneissose granitoids (81−75 Ma Ma pulse) into the middle crust at ~19−24 km depth, and (3) 75−69 Ma: voluminous intrusions of massive to weakly-foliated granitoids (75−69 Ma pulse) at ~ 9−13 km depth and formation of contact metamorphic aureoles. Cooling of the highest-grade metamorphic zone below the wet solidus of granitic rocks is estimated at 88.5 ± 2.5 Ma. At ca. 75 Ma, the upper-middle crustal section underwent northward tilting, resulting in the exhumation of regional metamorphic zones to ~ 9−13 km depth. Although the highest-grade metamorphic rocks and the 99−95 Ma pulse granitoids preserve similar U-Pb zircon ages, the absence of spatial association suggests that the regional metamorphic zones were mainly produced by a transient thermal anomaly in the mantle and thermal conduction through the crust, supplemented by localized advection due to granitoid intrusions. The successive emplacement of granitoids into shallow, deep and shallow levels of the crust was probably controlled by the

combination of change in thermal structure of the crust and tectonics during granitoid intrusions.

Keywords

Continental crust formation, flare-ups, plutono-metamorphic evolution, granite, U−Pb zircon dating, low-P/T type metamorphism

1. Introduction

Continental arcs are extended belts where the production, upward migration, eventual solidification at depth or eruption of magma contributes to form new continental material. Arcs appear to be mainly built during periods of increased magma production (‘flare-ups’) punctuated by stages of relatively lower magmatic activity (‘lulls’) (e.g. Ducea, 2001). Estimates of magma addition rates in the Sierra Nevada Batholith (USA) indicate that 100–1000 times more magma is added to continental arcs during flare-ups than during lulls, and that the ratio of plutonic to volcanic material is about 30/1 (Paterson and Ducea, 2015). The latter ratio emphasizes the wealth of information that can be gathered from relatively deep levels of eroded arc systems, where plutonic rocks are widely exposed. This episodic nature of arc magmatism has a fractal character; at a shorter (< 50 Ma) and smaller (< 50 km wide) scale, a ‘flare-up’ event involves discrete ‘pulses’ of increased magmatic activity (e.g. de Silva et al., 2015) while the depth of pluton emplacement or the location of eruption centers varies with time (Tibaldi et al., 2013; de Saint Blanquat et al., 2011). Thus, understanding the origin and evolution of a flare-up event and its associated crustal response requires deciphering its history in a shorter time-scale.

The Ryoke plutono-metamorphic belt, exposed in southwest to central Japan, is an appropriate target to decipher the intricate history of a flare-up. First, it represents the upper- to mid-crustal section of a continental arc in which voluminous I-type plutonic rocks (e.g. Nakajima, 1994; Shibata and Ishihara, 1979a) and thick ignimbrite sequences (e.g. Yamada and Koido, 2005) testify for the occurrence of a Cretaceous flare-up event (Sato et al., 2016). From a comprehensive set of sensitive high resolution ion microprobe (SHRIMP) zircon dating results, Tani et al. (2014) revealed that granite pulses in SW Japan occurred at 85, 60 and 35 Ma and were separated by 25 million year lulls. The flare-up event recorded in the Ryoke belt corresponds to the 85 Ma pulse. Second, the Ryoke belt hosts low-pressure/temperature (low-P/T) type metamorphic rocks which were variably affected by successive plutonic intrusions (Brown, 1998; Ikeda, 1998a, b; Kawakami, 2001; Kawakami and Suzuki, 2011; Miyake et al., 1992; Miyashiro, 1961; Miyazaki, 2010; Okudaira et al., 1993). Thanks to the tectono-metamorphic record of these metasedimentary rocks, constraints on the timing, depth and temperature of individual intrusions (e.g. Endo and Yamasaki, 2013; Miyake et al., 2016) are much more accessible than for exclusively plutonic regions.

The current challenge is to gather reliable time estimates of the magmatic activity and metamorphic events in the Ryoke belt. For granitoids, the earliest geochronological results involved whole-rock Rb–Sr ages and K–Ar or Rb–Sr ages on biotite and hornblende (Kawano and Ueda, 1967; Nozawa, 1975; Shibata and Ishihara, 1979b), and their compilation revealed an eastward younging from ca. 100 Ma to ca. 70 Ma over ~800 km (Nakajima, 1994). With the assumption that these ages correspond to pluton solidification, the younging trend was explained by a migration of magmatic activity due to the oblique subduction of the Kula-Pacific ridge beneath the Eurasian continent (Nakajima, 1994; Kinoshita, 1995). However, chemical Th−U−total Pb isochron method (CHIME) monazite ages subsequently obtained on high-grade metamorphic rocks and granitoids turned out to be older than K−Ar biotite ages and were ascribed to prograde metamorphism and pluton solidification, respectively (Suzuki et al., 1996; Suzuki and Adachi, 1998). Following this view, the eastward younging of K−Ar biotite ages was ascribed to a difference in the denudation rate rather than in magmatic activity, with the western part of the belt having been eroded more rapidly than the eastern part (Suzuki and Adachi, 1998). More recently, the growing number of available U−Pb zircon ages for the Ryoke granitoids revealed discrepancies between U−Pb zircon, CHIME monazite and K−Ar biotite ages (Murakami et al., 2006; Skrzypek et al., 2016; Takatsuka et al., 2018). The current tendency is to consider zircon as the best tool to constrain the age of pluton solidification. The first advantage of zircon is its high closure temperature near or above the solidus of granitic rocks. The second advantage is its robustness with respect to secondary alteration/recrystallization compared to monazite and biotite (e.g. Bosse et al., 2009; Kawakami et al., 2014). The third advantage is that it is the most representative accessory mineral that can be dated in allanite-bearing granitoids where monazite is virtually absent, as is the case for most granitoids in the Mikawa area so far (Takatsuka et al., 2018).

In the present study, we aim to detail the spatial distribution and timing of plutonic activity and regional metamorphism during the Cretaceous flare-up event which occurred at the active continental margin of Eurasia. The solidification age of the so-called 'Younger Ryoke' granitoids exposed in the Mikawa area (Ryoke belt, central Japan) are newly determined using U−Pb zircon dating by Laser Ablation Inductively Coupled Plasma Mass Spectrometry (LA−ICP−MS). Additionally, the emplacement depth of several granitoids is estimated using Al-in-hornblende barometry and published *P*−*T* estimates for the host metasedimentary rocks. The timing of regional metamorphism is also constrained by LA−ICP−MS U−Pb zircon dating. The results are combined to reconstruct how a former accretionary complex progressively transformed to the granitoid-dominated, metamorphosed upper- to middle-crust of an arc during a flare-up event.

2. Geology of the Ryoke belt in the Mikawa area

Within the Inner Zone of SW Japan, the Ryoke belt extends for about 800 km from northern Kyushu to Tsukuba (Fig. 1a), and the Mikawa area is located in its eastern part. The Mikawa area exposes low-*P*/high-*T* metamorphic rocks and voluminous granitic rocks (Fig. 1b; Asami et al., 1982; Miyake et al., 1992, 2014, 2016, 2017; Adachi and Wallis, 2008; Miyazaki, 2010; Takatsuka et al., 2018).

The Ryoke granitoids have been classically divided into the gneissose "Older Ryoke" and massive "Younger Ryoke" granitoids based on lithology and intrusive relationships (Ryoke Research Group, 1972). In the Mikawa area, the "Older Ryoke" granitoids include the Kamihara tonalite, Tenryukyo granite and Kiyosaki granodiorite, whereas the "Younger Ryoke" granitoids correspond to the Shinshiro tonalite, Mitsuhashi granodiorite, Inagawa granite and Busetsu granite (Fig. 1b; Makimoto et al., 2004). All plutons are considered as I-type granitoids, except for the Busetsu granite which has a composition close to that of S-type granites (Ishihara and Chappell, 2007). CHIME monazite ages for the "Older Ryoke" and "Younger Ryoke" granitoids are ca. 97−87 Ma and ca. 86−75 Ma, respectively (Table 1; Nakai and Suzuki, 1996; 2003; Morishita et al., 1996; Morishita and Suzuki, 1995; Suzuki and Adachi, 1998; Suzuki et al., 1994a; 1994b; Miyake et al., 2016). Based on these CHIME monazite ages, the "Younger Ryoke" granitoids were thought to have continuously intruded one after another from ca. 86 Ma to ca. 75 Ma (e.g., Suzuki and Adachi, 1998). Recently, however, LA−ICP−MS U−Pb zircon dating revealed that the gneissose granitoids have a bimodal distribution of U−Pb zircon ages, with two groups at ca. 99−95Ma and ca. 81−75 Ma, the latter age group being further divided into the '81−75 Ma Hbl−Bt tonalite' and '78−75 Ma (Hbl)−Bt granite' (Fig. 1b; Takatsuka et al., 2018). In contrast to the U−Pb zircon and CHIME monazite ages, K−Ar ages of biotite and hornblende from the "Older Ryoke" and "Younger Ryoke" granitoids show similar values of ca. 73−66 Ma

(Table 1).

The metamorphic rocks represent equivalents of the Jurassic to Early Cretaceous accretionary complex material which is found in the northerly Mino-Tanba belt (Wakita, 1987). They are composed of metachert, metasandstone and metamudstone with scarce metabasalt (Makimoto et al., 2004). The metamorphic rocks are foliated, strike NE−SW to E−W and variably dip towards the north. In the south of the study area, both north- and south-dipping foliation planes are observed and point to km-scale upright folding. Three regional metamorphic zones and one contact metamorphic zone are defined in the Mikawa area; the former are the Bt, Kfs−Sil and Grt−Crd zones in order of increasing metamorphic grade (Fig. 1b; Makimoto et al., 2004; Miyazaki et al., 2008; Nakashima et al., 2008; Yamasaki and Ozaki, 2012). The peak $P-T$ conditions of each metamorphic zone are estimated to be 0.29−0.37 GPa, 506−593 ºC for the Bt zone, 0.37−0.43 GPa, 574−709 ºC for the Kfs−Sil zone, and 0.43−0.57 GPa, 715−801 ºC for the Grt−Crd zone (Miyazaki, 2010). The contact metamorphic zone (Kfs−Crd zone) is developed around the "Younger Ryoke" granitoids (Endo and Yamasaki, 2013; Miyazaki et al., 2008; Yamasaki and Ozaki, 2012); its $P-T$ conditions are 0.23−0.24 GPa and > 600 ºC around the Shinshiro tonalite and the Mitsuhashi granodiorite (Endo and Yamasaki, 2013), and 0.32 GPa and > 630 ºC around the Inagawa granite (Miyake et al., 2016).

Pelitic and psammitic gneiss samples from the Kfs−Crd zone give CHIME monazite ages of ca. 102–98 Ma which are interpreted as the timing of prograde monazite growth at upper amphibolite facies conditions during regional metamorphism (Suzuki et al., 1994a, b). K–Ar biotite ages of ca. 67.5 Ma and ca. 69 Ma are reported for a Bt schist sample (Kfs–Crd zone) nearby the Kiyosaki granodiorite (Ueno et al., 1969). SHRIMP U–Pb zircon ages of ca. 87 Ma are reported for a migmatite sample from the Grt–Crd zone and are correlated with the timing of peak regional metamorphism (Nakajima et al., 2013). Among mafic igneous rocks sporadically exposed in the Mikawa area (Fig. 1b), hornblende gabbro and basaltic andesite give SHRIMP U–Pb zircon ages of 72.4 ± 1.2 Ma and 71.5 ± 1.1 Ma, respectively (Nakajima et al., 2004).

3. Analytical procedures

Quantitative analyses of hornblende were performed using a JEOL JXA-8105 superprobe at Kyoto University. Analytical conditions were an acceleration voltage of 15.0 kV, a beam current of 10 nA and a beam diameter of 3 μm. The counting time for the peak and backgrounds were 30 s and 15 s for Cl, 60 s and 30 s for F, and 10 s and 5 s for other elements. Natural and synthetic minerals were used as standards and ZAF correction was applied.

Granitoid, leucosome (GY03D) and pegmatite (GY47A) samples were crushed using Selfrag Lab at the National Institute of Polar Research (NIPR), Japan. Zircon grains were separated by panning, handpicking under a stereomicroscope, and were mounted in epoxy.

Cathodoluminescence (CL) and backscattered electron (BSE) images were obtained using a JEOL JXA-8105 superprobe at Kyoto University. Inclusions in zircon were identified using a S3500H scanning electron microscope equipped with an EDAX X-ray analytical system, and Al_2SiO_5 minerals were identified by Raman spectroscopy (JASCO NRS 3100) at Kyoto University.

U–Pb zircon dating by LA–ICP–MS was performed in Kyoto University and Gakushuin University. Most analyses were done on separated zircon grains. Dating in Kyoto University was performed using a Nu PlasmaII multi-collector ICP–MS coupled to a NWR193 laser-ablation system utilizing a 193 nm ArF excimer laser. Dating in Gakushuin University was performed using an Agilent8800 single-collector ICP–MS coupled to a NWR213 laser-ablation system utilizing a 213 nm Nd:YAG laser. The 91500 zircon (Wiedenbeck et al., 1995, 2004) was used as a primary reference material for Pb/U and Th/U ratios while NIST SRM610 glass (Pearce et al., 1997; Jochum and Brueckner, 2008) was used for Pb/Pb isotope ratios. Details on the analytical procedures and data reduction schemes are summarized in Supplementary material (Table S1). Secondary standard analyses indicate that inter-laboratory differences in zircon dating results are not significant (Takatsuka et al., 2018). Isoplot 4.15 (Ludwig, 2012) was used to construct concordia diagrams and to calculate weighted mean $^{206}Pb/^{238}U$ ages. Analyses with concordance [= ($^{206}Pb/^{238}U$ age) *100 / ($^{207}Pb/^{235}U$ age)] between 97 and 103% are referred to as concordant in this study and used for calculating weighted mean $^{206}Pb/^{238}U$ ages.

4. Sample description

4.1. Shinshiro tonalite

Samples GY50A [N34.914783º, E137.455796º] and GY100A [N34.940262º, E137.548428º] are Hbl-Bt tonalites (Fig. 1), both corresponding to the main facies of the Shinshiro tonalite (Ohtomo, 1985). On the outcrops, a moderate foliation defined by the arrangement of biotite and hornblende can be recognized, and ellipsoidal mafic enclaves with their long axis oriented parallel to the foliation are present (Fig. 2a, b). This foliation has been interpreted to be magmatic in origin (Ohtomo, 1985). Both samples are composed of Qtz, Pl, Kfs, Bt and Hbl with accessory Ap, Zrn, Ilm, Ttn, secondary Ep and secondary Chl (Fig. 3a, b). Allanite is present in sample GY100A.

4.2. Mitsuhashi granodiorite

Sample GY99A [N35.047113º, E137.523850º] is a Hbl-Bt granodiorite (Fig. 1) with a weak foliation defined by the arrangement of biotite and hornblende (Fig. 2c). The granodiorite is composed of Qtz, Pl, Kfs, Bt and Hbl with accessory Ap, Zrn, Ilm, Ttn and secondary Chl (Fig. 3c).

4.3. Inagawa granite

Samples GY86A [N35.057774º, E137.256294º] and GY93A [N35.149147º, E137.301422º] are Hbl-Bt granites with Kfs megacrysts clearly showing the Carlsbad twin (Fig. 1). Sample GY86A collected from the 'gneissose porphyritic facies' (Yamasaki and Ozaki, 2013) shows a weak foliation defined by the arrangement of biotite, whereas sample GY93A collected from the 'massive facies' (Yamasaki and Ozaki, 2013) shows a faint grain-shape preferred orientation of Kfs megacrysts and amphibole (Fig. 2d, e). Both samples are composed of Qtz, Pl, Kfs, Bt and Hbl with accessory Ap, Aln, Zrn, Ilm and Ttn (Fig. 3d, e). Xenomorphic Ep is present as a matrix mineral, filling intergranular spaces between euhedral plagioclase grains together with secondary Chl in sample GY93A, whereas secondary Ep overgrowing rims of allanite, secondary Py, and Po included in Kfs are present in sample GY86A.

4.4. Busetsu granite

Samples GY51A [N34.967778°, E137.335781°] and MK02M [N34.954766°, E137.326847°] are Grt-bearing two-mica granites and sample GY89A [N35.030050°, E137.296534°] is a two-mica granite (Fig. 1). At locality GY51, biotite-rich lenses and pelitic xenoliths (2–4 cm in length) locally occur within the medium-grained granite (Fig. 2f). Sample MK02M was collected 1 m away from the discordant contact between fine-grained granite and Grt-bearing biotite metapsammite; the Busetsu granite obliquely cuts the subvertical bedding in metapsammite there (Fig. 2g). Sample GY89A was collected close to the N–S trending contact with the western edge of the Kamihara tonalite (Fig. 1). The arrangement of Bt, Ms, and Qtz ribbons define a moderate mylonitic foliation (N 152°/65° SW) which surrounds the Kfs megacrysts (Fig. 2h). Bulging recrystallization of quartz indicates low-*T* deformation during the possible fault-like reactivation of the former contact. All samples of the Busetsu granite are composed of Qtz, Pl, Kfs, Bt and Ms, and samples MK02M and GY51A additionally contain Grt (Fig. 3f−h). Accessory Ap, Mnz, Zrn, Ilm and xenotime are present in all samples.

4.5. Metasedimentary rocks between the Kamihara and Busetsu granitoids

A narrow band (< 1 km wide on map view) of metamorphic rocks occurs between the southern edge of the Kamihara tonalite and the Busetsu granite (Fig. 1). At several localities, psammitic gneiss with an E−W striking and N-dipping foliation is locally intruded by concordant sills of fine- to medium-grained granite containing Bt, Ms and Grt. At locality GY92, a pelitic gneiss sample (GY92A1) consists of And, Sil (postdating And), Crd (replacing And rims), Bt, Kfs, Pl, Qtz, secondary Ms, and subordinate Tur, Ap, Mnz, Zrn and Gr. Andalusite has a chiastolite texture and is partly transformed to prismatic sillimanite or fibrolite at the rim (Fig. 3i). Inclusion minerals defining the chiastolite texture does not define an internal foliation (cf. Adachi and Wallis, 2008). Andalusite is surrounded by and replaced by pinitized cordierite at the rim. The main foliation defined by the arrangement of biotite and fibrolite is deflected around the andalusite porphyroblasts, which indicates a pre-tectonic growth of andalusite and cordierite (Fig. 3i). Secondary muscovite grains replace fibrolite and some of them discordantly cut the foliation.

4.6. Migmatite and pegmatite from the Grt-Crd zone

A ~20 cm thick leucosome in a psammitic metatexite migmatite (GY03D) and a pegmatite concordant with migmatitic banding (GY47A) were collected from the Grt−Crd zone (Fig. 1). The leucosome in sample GY03D is subparallel to the migmatitic banding of the host psammitic migmatite (Fig. 2i), and mainly consists of Bt, Ms, Grt, Kfs, Pl and Qtz, with accessory Tur, Ap, Zrn and opaque mineral (Fig. 3k). Myrmekite is common. The pegmatite concordant with the migmatitic banding (GY47A) is found as a layer (~30−40 cm thick) below mafic lenses enclosed in metatexite migmatite (Fig. 2j). The same cm-thick pegmatite also rims the structurally upper side of the mafic lenses, and is further surrounded by the gneissose structure of the metatexite migmatite hosting them. The pegmatite mainly consists of Kfs, Qtz, Pl, Bt, Crd, Sil, and Ms, with accessory Ap, Zrn and Mnz. Fine-grained myrmekite is abundant along the grain boundaries of K-feldspar, where sillimanite and secondary muscovite are common (Fig. 3l). The rims of quartz grains are locally recrystallized into finer grains (Fig. 3l).

5. U−Pb zircon dating

Cathodoluminescence images of representative zircon grains from all granitoid samples are presented in Figures 5 and 6, and those from migmatite and pegmatite samples are presented in Figures 7 and 8. The weighted mean ages and spot ages reported below are $^{206}Pb/^{238}U$ ages unless specified.

5.1. Shinshiro tonalite

Most zircon grains from samples GY50A and GY100A have homogeneous or oscillatory-zoned cores, overgrown by oscillatory-zoned CL-bright rims (Fig. 4a, b, e, f).

Sample GY50A

A total of 61 spots on 23 grains was analyzed (Table S2; spots 1.1−2.11 and 12.1−14.13). Two data were rejected because of irregular signals. One grain has an inherited core with a concordant age of 1880 ± 37 Ma ($^{207}Pb/^{206}Pb$ age). Concordant analyses of Cretaceous domains have $^{206}Pb/^{238}U$ ages ranging from ca. 79 to ca. 68 Ma. Two grains with CL-dark oscillatory zoning (Fig. 4c, d) yield ca. 79−76 Ma and are slightly older than the other Cretaceous concordant ages (ca. 71−68 Ma). The main age population is well defined at ca. 71−68 Ma, and its weighted mean is 69.5 ± 0.3 Ma (32 spots, MSWD = 1.07, Fig. 8a).

Sample GY100A

A total of 33 spots on 14 grains was analyzed (Table S2; spots 71.7−73.13). One data was rejected because of irregular signal. The $^{206}Pb/^{238}U$ ages of all Cretaceous concordant data range from ca. 73 to ca. 69 Ma, and their weighted mean is 70.6 ± 1.0 Ma (9 spots, MSWD = 0.44, Fig. 8b).

5.2. Mitsuhashi granodiorite

Zircon grains from sample GY99A have homogeneous or oscillatory-zoned cores overgrown by oscillatory-zoned rims (Fig. 4g–h). A total of 32 spots on 15 grains was analyzed (Table S2; spots

69.1–71.6). One data point was rejected because of irregular signal. One grain has an inherited core with a concordant age of 501 ± 18 Ma. The $^{206}Pb/^{238}U$ ages of all Cretaceous concordant data range from ca. 76 to ca. 71 Ma and define a single age population (Fig. 8c). Their weighted mean is 73.2 ± 0.7 Ma (11 spots, MSWD = 0.91, Fig. 8c).

5.3. Inagawa granite

Zircon grains from samples GY86A and GY93A show homogeneous or oscillatory-zoned cores and oscillatory-zoned rims (Fig. 4i–l).

Sample GY86A (gneissose porphyritic facies)

A total of 39 spots on 17 grains was analyzed (Table S2; spots 33.1–35.13) and 25 analyses are concordant. One grain has an inherited core with a concordant age of 296 ± 13 Ma. The $^{206}Pb/^{238}U$ ages of all Cretaceous concordant data range from ca. 78 to ca. 72 Ma, and show a single age population. Their weighted mean is 74.7 ± 0.7 Ma (24 spots, MSWD = 0.61, Fig. 8d).

Sample GY93A (massive facies)

A total of 33 spots on 15 grains was analyzed (Table S2; spots 64.1–66.7), and 16 analyses are concordant. The $^{206}Pb/^{238}U$ ages of all concordant data range from ca. 72 to ca. 68 Ma, and show a single population. Their weighted mean is 69.2 ± 0.5 Ma (16 spots, MSWD = 1.02, Fig. 8e).

5.4. Busetsu granite

Zircon grains in Busetsu granite samples record four Cretaceous growth stages at (A) ca. 99 Ma, (B) ca. 95−84 Ma, (C) ca. 80 Ma and (D) ca. 70 Ma (Figs. 5; 8f−h). These age domains are associated with particular textural and compositional features. Domain A corresponds to oscillatory- or sector-zoned cores and rims with a relatively high Th/U ratio (0.34−0.52) and a ca. 99 Ma age (Fig. 5a); only one grain of this type has been found so far. Domain B corresponds to the homogeneous to weakly oscillatory-zoned parts commonly occurring in zircon mantle (i.e. between core and rim). These mantles include sillimanite needles, have a low Th/U ratio (0.02−0.12) and ages of ca. 95−85 Ma (Fig. 5b−g). Domain C corresponds to mantle or rim parts with a homogeneously bright or oscillatory-zoned CL pattern, a moderate Th/U ratio (0.22−0.44, with one exception at 0.04) and a ca. 80 Ma age (Fig. 5e−i). Domain D correspond to sector- or oscillatory-zoned cores and oscillatory-zoned rims with a variable Th/U ratio (0.06−2.38) and a ca. 70 Ma age (70.8 ± 1.4 Ma to 69.5 ± 0.4 Ma; Fig. 5b−d, h−m). Domain D is dominant in all three samples.

Sample GY51A

A total of 112 spots on 45 grains was analyzed (Table S2; spots 4.11−6.13, 15.1−20.13 and 63.5−63.9), and 51 analyses gave concordant data. Nine data were rejected because of irregular signals. The weighted mean age of domain D analyses (cores and rims) is 69.5 ± 0.4 Ma (37 spots, MSWD = 2.3, Fig. 8f). Some cores give concordant, inherited ages of 1896 ± 38 Ma and 2272 ±

35 Ma (^{207}Pb/^{206}Pb age). Zircon grains showing domain B ± domain C + domain D around some inherited cores (Fig. 5b–c; 4 grains) give a concordant age of 254 ± 6 Ma for the inherited core and ca. 95–91 Ma for domain B mantles with a low Th/U ratio (0.02–0.12). Zircon grains with domain B + domain C (3 grains) give concordant ages of ca. 86–84 Ma and ca. 80–78 Ma for domain B (low Th/U ratio, 0.06–0.09) and domain C, respectively (Fig. 5e–g). Oscillatory-zoned rims were not analyzed because they are thinner than the laser spot size. Zircon grains with domain C + domain D (2 grains) give discordant dates of ca. 78–77 Ma for both cores and mantles.

Sample MK02M

A total of 26 spots on 15 grains was analyzed (Table S2; spots 44.1–45.13). One data was rejected because of irregular signal. Domain D yields concordant ages of ca. 75–68 Ma, and the weighted mean ages is 70.9 ± 0.9 Ma (21 spots, MSWD = 1.5, Fig. 8g). An inherited core with a discordant date of ca. 1960 Ma (^{207}Pb/^{206}Pb) is also observed. In one grain preserving an inherited core ± domain B ± domain C + domain D, the mantle part (B) gives a concordant age of 89.4 ± 4.0 Ma with a Th/U ratio of 0.03 (Fig. 5d). Zircon grains with domain C + domain D (2 grains) gave concordant ages of ca. 79–77 Ma for core or mantle parts (Fig. 5h, i).

Sample GY89A

A total of 26 spots on 13 grains was analyzed (Table S2; spots 46.1–47.13). Four data were rejected because of irregular signals. Except for one grain, all analyzed domains are classified into domain D. Zircon grains with domain D cores and rims yield concordant ages of ca. 74−68 Ma, and the weighted mean age is 70.8 ± 1.4 Ma (11 spots, MSWD = 1.6, Fig. 8h). Inherited cores with concordant ages of ca. 270−191 Ma and ca. 1905−1879 Ma ($^{207}Pb/^{206}Pb$ age) are also observed. The outermost rim of one oscillatory-zoned zircon yields a concordant age of 96.6 ± 4.3 Ma (Fig. 5a) and is tentatively classified as domain A.

5.5. Migmatite and pegmatite from the Grt-Crd zone

Sample GY03D (~20 cm thick leucosome in metatexite)

Zircon grains commonly show CL-bright cores and CL-dark rims (Fig. 6). Rims are composed of CL-bright inner rims and CL-dark outer rims, and a CL-dark annulus (e.g. Kawakami et al., 2013) is commonly observed between the cores and the inner rims. Sillimanite is found as inclusions in the inner rim (Fig. 6) of two zircon grains. A total of 39 spots on 18 grains was analyzed (Table S2; spots 41.1−43.13). Four data were rejected because of mixed analysis between cores and rims, and one data was rejected because of irregular signal. Zircon cores give various inherited ages (Table S2). Rims give scattered concordant ages from ca. 103 Ma to ca. 83 Ma (Fig. 9a, b). Inner rims have a low U concentration (< 1300 ppm) and various Th/U ratio whereas outer rims are U-richer (> 2300 ppm) and show very low Th/U ratio (Fig. 9c, d). The inner rims tend to give older ages ranging from ca. 101 Ma to ca. 92 Ma (weighted mean; 97.0 ± 4.4 Ma, 6 spots, MSWD = 3.8). In contrast, the outer rims tend to give younger ages from ca. 95 Ma to ca. 83 Ma (weighted mean; 88.5 ± 2.5 Ma, 12 spots, MSWD = 4.1) (Figs. 6, 9c, d). There was no tendency for U-rich zircon domains to give older ages (cf. Skrzypek et al., 2016).

SampleGY47A (Pegmatite)

Zircon grains commonly show oscillatory-zoned cores and CL-dark rims (Fig. 7). Sillimanite is found as an inclusion in the rim (Fig. 7). A total of 19 spots on 5 grains was analyzed (Table S2; spots 9.1−9.13, 27.8−27.13). Two data were rejected because of mixed analysis between cores and rims. Zircon cores give various inherited ages (Fig. 7; Table S2). Rims give relatively clustered concordant ages from ca. 93 Ma to ca. 87 Ma with one outlier of ca. 98 Ma spot (Figs. 7, 9e, f). The concordia age for the zircon rims in this sample gave 90.1 ± 1.2 Ma (8 spots, MSWD = 4.2), excluding the ca. 98 Ma outlier (Fig. 9e−f).

6. Al-in-hornblende geobarometry

In order to estimate the crystallization depth of the '81−75 Ma Hbl−Bt tonalite' and '78−75 Ma (Hbl)−Bt granite', which are the gneissose granitoids thought to postdate regional metamorphism (Takatsuka et al., 2018), the Al-in-hornblende geobarometer (Schmidt, 1992) was applied to samples GY33A and GY81B (Fig. 1). Sample GY33A is a Hbl-Bt granite (Goyu area) while sample GY81B is a Hbl-Bt tonalite (Hazu area). Their respective U−Pb zircon ages are 78 ± 1 Ma and 81 ± 1 Ma, and their full description is given in Takatsuka et al. (2018). In both granitoids, the mineral assemblage Hbl + Bt + Pl + Kfs + Qtz + Ap + Ilm + Ep + Ttn (+ Po + Py + Zrn) permits the application of the geobarometer. Representative WDS analyses of hornblende used in the estimates are given in Tables S3 and S4. The total Al content was calculated based on O = 23, assuming total iron as Fe^{2+}.

Hornblende grains in sample GY33A are in contact with Qtz, Pl, Kfs and Bt, and are partially retrogressed to Bt and Chl at the rims or along cracks. Hornblende grains in sample GY81B are in contact with Qtz, Pl and Bt, and compositional zoning is observed under the optical microscope while it is not noticeable in BSE images. The total Al in hornblende ranges from 0.89 to 2.13 atoms per formula unit (a.p.f.u.) for sample GY33A, and from 1.66 to 2.30 a.p.f.u. for sample GY81B. Low-Al domains present along the cracks in hornblende (sample GY33A) and the local development of high-Al domains at the rims of hornblende (both samples) are considered as secondary features which do not record the timing of granitoid crystallization. Excluding these domains, the total Al content of hornblende in both samples is 1.70–2.00 a.p.f.u. for the rims (O = 23, Tables S3 and S4). For geobarometry, the total Al content of hornblende rims was used because rims are considered to have equilibrated with the final melt, fluid and other coexisting minerals at the granitic wet solidus. With the calibration of Schmidt (1992), pressure estimates are 0.50–0.64 GPa and 0.50–0.63 GPa for samples GY33A and GY81B, respectively. Geobarometry was not applied to the Kamihara tonalite and Kiyosaki granodiorite samples because appropriate mineral assemblage was not found.

7. Regional implications

7.1. Interpretation of U–Pb zircon dating results

In the Shinshiro tonalite and Mitsuhashi granodiorite samples, zircon is found included in major minerals or along grain boundaries (Fig. 3a–c), and the majority of zircon shows a CL-bright oscillatory zoning pattern (Fig. 4a–h). These magmatic features suggest that the dominant age population of each sample reflects the timing of magma crystallization, which occurred at ca. 70 Ma for the Shinshiro pluton and ca. 73 Ma for the Mitsuhashi pluton. The main facies of the Shinshiro pluton dated in this study and of Mitsuhashi pluton locally hosts allanite (Yamasaki and Ozaki, 2012) and virtually does not contain monazite. Therefore, monazite-bearing granitoid samples used for CHIME monazite dating that yielded 84–86 Ma ages (Suzuki et al., 1994a, b; Morishita and Suzuki, 1995) do not correspond to the typical facies of each pluton, and a strong interaction with the surrounding metamorphic rocks is inferred. These older monazite grains may be derived from the neighboring metamorphic rocks in which the age of high-*T* regional metamorphism was estimated at ca. 97–89 Ma based on U–Pb zircon dating in this study (see below). Similarly, the CL-dark 77 Ma zircon grains found in the Shinshiro tonalite (Fig. 4c, d) could be derived from the neighboring '78–75 Ma (Hbl)–Bt granite' (sample GY48D in Takatsuka et al., 2018).

In the Inagawa pluton, zircon analyses define a dominant population at 74.7 ± 0.7 Ma for the gneissose porphyritic facies and 69.2 ± 0.5 Ma for the massive facies (Table 2). The ubiquitous occurrence of oscillatory-zoned zircon in both samples is used to ascribe these results to magma solidification. The age of the gneissose porphyritic facies is consistent with the U−Pb zircon age of 73 ± 3 Ma reported from a similar lithology within the Asuke Shear Zone (Murakami et al. 2006; Fig. 8). Again, the absence of monazite and presence of euhedral magmatic allanite in both samples suggests that the previously reported CHIME ages (83−82 Ma; Suzuki and Adachi, 1998) are probably not related to the crystallization of the main magma batch.

Zircon ages of the metatexite migmatite and pegmatite samples from the Grt-Crd zone place important constraints on the timing of regional metamorphism in the Mikawa area. Zircon grains from the metatexite leucosome GY03D show two stages of rim growth that are texturally, chemically and chronologically distinct; CL-bright, low-U inner rims with a weighted mean age of 97.0 ± 4.4 Ma are overgrown by CL-dark, high-U outer rims with a weighted mean age of 88.5 ± 2.5 Ma (Figs. 6, 9a−d). The high MSWDs of these weighted mean ages might be due to a continuous growth of zircon rims from 102.9 ± 4.6 Ma to 83.1 ± 3.7 Ma (Figs. 6, 9a−d), but this requires confirmation by higher precision age dating. In the present study, we attach importance to the fact that zircon rims texturally record two growth stages and consider the weighted mean ages as their growth timings. There are two possible scenarios for the origin of inner rims. First, the inner rims might be resulted from prograde growth due to Ostwald ripening in the presence of melt as proposed in another part of the Ryoke belt (Kawakami et al., 2013). In the present study, the variable Th/U ratios (0.01−0.11) observed for the inner rims of zircon, compared to nearly constant values for the outer rims (Fig. 9d), may reflect the chemical variation of fine-grained detrital zircon grains consumed by the Ostwald ripening process which probably took place in isolated melt pockets with different local compositions. Variable Th/U ratio of zircon cores (0.04−1.45) is consistent with this interpretation (sample GY03D in Table S2). Alternatively, the inner rims may reflect early zircon crystallization from melt at the very beginning of the cooling stage immediately after the temperature peak. The entrapment of sillimanite might have equally occurred during prograde or retrograde zircon growth at hypersolidus conditions. In this study, the former interpretation that the inner rims represent the prograde growth of zircon is preferred based on the observation of Th/U ratios. In both cases, the outer rim age of 88.5 ± 2.5 Ma is interpreted as the timing of final zircon crystallization from melt at the granite wet solidus, and a *P-T* path with a single temperature peak is sufficient to account for the inferred zircon crystallization history (e.g., Brown, 1998; Kawakami et al., 2001). The pegmatite sample GY47A contains cordierite and sillimanite, and could be a segregated partial melt derived from the surrounding or underlying migmatites. The concordia age of 90.1 ± 1.2 Ma (Fig. 9e) represents the timing of zircon crystallization in the pegmatite in the sillimanite stability field (Fig. 7), and probably approximates the crystallization timing of the pegmatite melt. Judging from the available data above, the hypersolidus stage of Ryoke regional metamorphism in the Mikawa area started at 97.0 ± 4.4 Ma and continued until 88.5 ± 2.5 Ma.

In all samples from the Busetsu granite, zircon analyses reveal the presence of several age domains. Domain A was recognized in only one zircon from a Grt-free granite sample (GY89A) collected next to the western edge of the Kamihara pluton (Fig. 1). This grain shows a texture, age and Th/U ratio similar to those of zircon grains from the Kamihara tonalite (see Takatsuka et al., 2018), suggesting that it is a xenocryst derived from the neighboring pluton (Fig. 1). Domain B preserves homogeneous zoning and low Th/U ratios which are typical for metamorphic zircon (e.g. Rubatto, 2002). Furthermore, a few sillimanite grains are found as inclusions in this domain. Their age of ca. 95−85 Ma is in agreement with that of high-*T* regional metamorphism in the Grt−Crd zone (Fig. 9). Therefore, zircon grains with domain B were likely introduced into the Busetsu granite magma as xenocrysts originating from the assimilated metamorphic rocks that existed in the source region or along the intrusion pathway of the granite. The age of domain C (ca. 80 Ma) coincides with that of gneissose granitoids from the southern part of the Mikawa area ('81−75 Ma Hbl−Bt tonalite'; Takatsuka et al., 2018). Considering the moderate Th/U ratio of these domains, zircon grains with domain C alone could be considered as xenocrysts derived from the assimilated gneissose granitoids, but the coexistence of domains B and C in some grains points to a more complex history. Domain D are by far the most voluminous (Fig. 5); their sector or oscillatory zoning pattern and relatively high Th/U ratio indicate that they record a major event of magma crystallization which is ascribed to the solidification of the Busetsu granite at ca. 70 Ma. It is worth noting that for the Busetsu granite, in which monazite is a common accessory mineral while allanite is not observed, CHIME monazite ages (79−75 ± 5 Ma; Suzuki et al., 1994; Nakai and Suzuki, 2003) are nearly compatible with U-Pb zircon ages (71−69 ± 1 Ma).

7.2. Timing and depth distribution of granitoid intrusions in the Mikawa area

The U−Pb zircon ages of massive or foliated granitoids newly determined in this study range from ca. 75 to 69 Ma (Figs. 8, 10). Taking into account the U−Pb zircon ages of gneissose granitoids that are concordant with the main metamorphic foliation (Takatsuka et al., 2018), three magmatic pulses with a different spatial distribution and timing are recognized in the Mikawa area (Fig. 10). The oldest pulse occurred at ca. 99−95 Ma (Fig. 10); it is represented by gneissose granitoids which are mainly enclosed inside younger plutons in the central part of the area (Kamihara tonalite, Kiyosaki granodiorite). The subsequent pulse occurred at ca. 81−75 Ma (Fig. 10); it corresponds to gneissose granitoids which concordantly intruded into metamorphic rocks in the southern (deeper) part of the area ('81−75 Ma Hbl−Bt tonalite', '78−75 Ma (Hbl)−Bt granite'). The 99−95

Ma and 81−75 Ma magmatic rocks presently form elongated belts parallel to the NE−SW striking regional foliation of metamorphic rocks (Fig. 10). The youngest pulse occurred at ca. 75−69 Ma; massive to moderately-foliated granitoids intruded throughout the area and discordantly cut the metamorphic fabrics and zones (Shinshiro tonalite, Mitsuhashi granodiorite, Inagawa granite and Busetsu granite). For each pulse, the approximate surface exposure is ~ 135 km^2, ~ 110 km^2 and ~ 980 km^2 with decreasing age (Table S5).

The intrusion depth of the 99−95 Ma pulse plutons remains obscure because these oldest intrusions are either surrounded by younger granitoids (Fig. 10) or in contact with metamorphic rocks in which the contribution of contact and regional metamorphism is hard to evaluate (e.g. Miyake et al., 2016). Our best observation comes from a km-scale band of metamorphic rocks (Fig. 1) in between the gneissose Kamihara tonalite (99 Ma) and the massive Busetsu granite (70 Ma). There, pre-tectonic And (partly transformed to Sil) porphyroblasts overgrown by Crd (Fig. 3i, j) indicate low-*P* metamorphism in the andalusite stability field (< 0.38 GPa) before the intrusion of the post-tectonic Busetsu granite. If the grain size and chiastolite texture are regarded as a result of reaction overstepping due to rapid temperature increase (e.g. Waters and Lovegrove, 2002), the porphyroblasts might be correlated with contact metamorphism at the margin of the Kamihara pluton. This assumption is used to propose a relatively shallow intrusion depth (< 14 km; density of the crustal rocks is assumed to be 2.75 g/cm^3 throughout this paper) for the 99−95

Ma plutons.

For the 81−75 Ma pulse, the results of Al-in-hornblende geobarometry indicate that the '81−75 Ma Hbl−Bt tonalite' (sample GY81B) and the '78−75 Ma (Hbl)−Bt granite' (sample GY33A) intruded at a mid-crustal depth of ~19−24 km (Fig. 10). These data are consistent with the crystallization depth deeper than 17.5 km proposed for tonalitic rocks in the Hazu area (Masumoto et al., 2014), a part of the '81−75 Ma Hbl−Bt tonalite' body (Fig. 10). The youngest 75−69 Ma pulse granitoids generate contact metamorphic aureoles which allow estimating their emplacement levels (Fig. 10). Using pressure estimates from contact aureoles around the Shinshiro tonalite and the Mitsuhashi granodiorite (0.23−0.24 GPa; Endo and Yamasaki, 2013) and around the Inagawa granite (0.32 GPa; Miyake et al., 2016), the emplacement depth of these granitoids is estimated at ~ 9−12 km. The Busetsu granite is contemporaneous with these granitoids, intrudes all of them (Ryoke Research Group, 1972), and its southern margin overprints the Bt zone for which a peak pressure is estimated at 0.34 GPa (Miyazaki, 2010), suggesting that this granite intruded at a depth of ~ 13 km. Therefore, all data indicate that the 75−69 Ma pulse granitoids were emplaced at a nearly similar depth of ~ 9−13 km.

7.3. Plutono-metamorphic evolution of the Ryoke belt in the Mikawa area

The plutono-metamorphic evolution of the Ryoke belt in the Mikawa area during the Cretaceous flare-up starts with the intrusion of the 99−95 Ma pulse granitoids into the shallow levels of the crust (< 14 km) and contemporaneous high-*T* regional metamorphism at the mid-crustal depth (Fig. 11a). The similar NE−SW orientation of the gneissose structure in granitoids and the foliation in metamorphic rocks suggests that the 99−95 Ma pulse granitoids probably acquired their final structure during regional deformation after their intrusions (Fig. 11). The 99−95 Ma pulse granitoids are not affected by a strong metamorphic overprint, which supports their original intrusion into a relatively shallow level (< 14 km) of the former accretionary complex (Fig. 11a). A direct evidence for contemporaneous high-*T* regional metamorphism and partial melting at depth is given by the analysis of zircon rims in a leucosome sample from the Grt−Crd zone; the inner rims of zircon containing sillimanite and the outer rims of zircon yield weighted average U−Pb ages of 97.0 ± 4.4 Ma and 88.5 ± 2.5 Ma, respectively (sample GY03D; Figs. 6, 9a−d). An indirect evidence is the presence of sillimanite-bearing, low Th/U metamorphic mantles in zircon grains from the Busetsu granite (domain B; Fig. 5b−g). Considering that zircon in high-*T* metamorphic rocks mostly grows in the presence of anatectic melt (e.g. Roberts and Finger, 1997; Kawakami et al., 2013), the metamorphic mantles (Fig. 5b−g) point to sillimanite-stable, suprasolidus conditions in the source zone or intrusion pathway of the Busetsu granite at ca. 95−84 Ma.

The Grt−Crd zone was still at sillimanite-grade hypersolidus conditions at ca. 90 Ma as indicated by the age of zircon rims in the pegmatite sample (GY47A; 90.1 ± 1.2 Ma). The dynamic crystallization microtextures developed at grain boundaries of K-feldspar and quartz (Fig. 3l) suggests ductile deformation of the Grt–Crd zone rocks after the solidification of the pegmatite at ca. 90 Ma. The youngest zircon age in domain B of zircon from the Busetsu granite (ca. 84 Ma) can be taken as the onset of final cooling towards subsolidus conditions in the Sil–Kfs or Grt–Crd zones. These observations imply that heat flow from the lower crust could no longer sustain hypersolidus, regional high-*T* conditions at the end of this stage.

The second stage corresponds to another magmatic pulse from ca. 81 to 75 Ma (Fig. 11c). The 81–75 Ma pulse granitoids intruded in a relatively deep crustal level (> 18 km); Al-in-hornblende geobarometry results for tonalitic rocks (0.50–0.64 GPa) are almost equivalent to peak pressure estimates for the Grt–Crd zone (0.43–0.57 GPa; Miyazaki, 2010), indicating that no significant exhumation had occurred before ca. 81 Ma. The 81–75 Ma gneissose granitoids commonly preserve a magmatic foliation which is parallel to that of the host metamorphic rocks; this points to a syn-tectonic emplacement at relatively high-*T* conditions, but based on age differences, Takatsuka et al. (2018) interpreted that these granitoids were not the direct cause of the high-*T* regional metamorphism. Some 81–75 Ma gneissose granitoids also exhibit solid-state foliations (Takatsuka et al., 2018) indicating that they were deformed in a ductile manner even after magma solidification. This observation is used to infer that syn-tectonic cooling and exhumation of the Grt−Crd zone started just after the youngest deep intrusion, i.e., after ca. 75 Ma (Fig. 11d).

The final stage corresponds to the intrusion of the 75−69 Ma pulse granitoids (Fig. 11e). For granitoids emplaced at that time, U−Pb zircon ages range from ca. 75 to 69 Ma while K−Ar ages on biotite are only slightly younger and cluster at ca. 71−68 Ma (Table 1). Such a fast cooling history implies that the host metamorphic rocks into which the 75−69 Ma pulse granitoids intruded were relatively cold, possibly at a temperature below the closure temperature of the K−Ar system in biotite (340−360 °C; Hodges, 2005). In addition, all the 75−69 Ma pulse granitoids were emplaced at ~ 9−13 km depth (Figs. 10, 11e) and discordantly cut the regional metamorphic zones (e.g., Ryoke Research Group, 1972; Fig. 1). The cold and shallow environment inferred for the intrusion of the 75−69 Ma pulse granitoids requires that the metamorphic section, especially the Grt-Crd zone, had already been exhumed by ca. 70 Ma; it is best explained by a northward tilting of both the metamorphic rocks and gneissose granitoids (Fig. 11d). The average exhumation rate of the Grt−Crd zone metamorphic rocks between ca. 75 and 70 Ma is estimated at 0.80−2.4 km/Myr (0.80−2.4 mm/yr), which is slightly faster than the present-day erosion speed across the Japanese Islands excepting high-elevation areas (<0.75 mm/yr; Fujiwara et al., 1999).

8. Insights into the tectono-thermal response of the crust during a flare-up event

8.1. Succession of granitoid emplacement depths

One of the important features of the flare-up history revealed in this study is the sequence of granitoid emplacement depths. Pre-tectonic chiastolite found around the Kamihara tonalite (Fig. 3i–j) is used to propose a shallow intrusion level for the 99–95 Ma pulse granitoids. If this is accepted, the plutono-metamorphic evolutions in the western (Yanai area; Skrzypek et al., 2016) and the eastern (Mikawa area; this study) parts of the Ryoke belt reveal a common feature. In the Mikawa area, plutonic activity started with shallow intrusions (< 14 km), and was followed by deeper (18–24 km) and finally shallow ones (9–13 km; Figs. 11, 12). A similar cycle is recognized in the Yanai area where the oldest and shallow intrusions (< 14 km at ca. 105–100 Ma) are followed by deeper (~ 22 km at ca. 100 Ma) and again shallow (< 14 km at ca. 95 Ma) plutons (Skrzypek et al., 2016; Fig. 12).

The final emplacement level of magmatic intrusions in upper crustal regions is thought to depend on the interaction of rheology and rigidity contrasts within the crust, the crustal stress field, and the crustal and lithospheric density structure (Burov et al., 2003; Schubert et al., 2013). It can also be controlled by the preexisting geological structures that facilitate or prevent its ascent (Brown, 2013; Petri et al., 2017; Vigneresse and Clemens, 2000). Importance of the tectonic control on the intrusions of granitoids during the flare-up is inferred from the syn-tectonic nature of the 81–75 Ma pulse granitoids. However, the shallow granitoids of the first pulses are considered pre-tectonic both in the Yanai and Mikawa areas. The temporal coincidence between the hypersolidus stage of regional metamorphism and the 99-95 Ma pulse in the Mikawa area (Fig. 12) suggests that the prograde stage of regional metamorphism should have already started before the intrusion of the 99−95 Ma pulse. In addition, the intrusion of the deep 81−75 Ma pulse granitoids occurred after the highest-grade regional metamorphic zone (Grt−Crd zone) cooled below the solidus temperature at 88.5 ± 2.5 Ma. These coincidences between granite emplacement depths and changes in the thermal structure suggest that emplacement levels of the plutons may, to some extent, be controlled by the thermal structure of the crust at their intrusion timings. The yield strength of the crust may have been lowered through heating, and this may have enabled granitoid magmas to be emplaced in relatively shallow crustal levels (e.g., Schubert et al., 2013). In the case of diapiric ascent of magmatic bodies, however, numerical models suggest that the effect of background thermal structure on the emplacement depth of plutons are in the order of several km (Burov et al., 2003). Therefore, the change in emplacement level of plutons (~ 10 km depth difference) should also be controlled by other factors such as tectonics during the granitoid intrusion. Whether similar link between high background thermal structure and granitoid emplacement in shallow levels of the crust exists for the 75-69 Ma pulse or not is unknown, because the metamorphic zones were already inclined at the timing of the 75-69 Ma pulse intrusion and thus the middle crust of that time is presently not exposed (Fig. 11e). The vertical movement of the granitoid magmas of the 75-69 Ma pulse could have potentially been facilitated by existing geologic structures in the crust, such as inclined foliation planes (e.g., Brown, 2013), since the foliation planes of the host metamorphic rocks had already been tilted by this stage (Fig. 11d−e).

8.2. Transient thermal anomaly in the mantle and formation of low-P/T type regional metamorphic zones

In the Mikawa area, the absence of syn-metamorphic (ca. 97−89 Ma) granitoids in the highest-grade Grt−Crd zone and the relatively long duration of regional hypersolidus conditions (> 8.5 ± 5.1 Myr) point to prolonged heating of the middle crust. The upper-middle continental crust is made up of an accretionary complex in which the amount of radiogenic heat producing elements is equivalent to the average continental crust values (Togashi et al., 2000). Even relatively deep granitoid intrusions hardly generate hypersolidus conditions longer than ca. 1 Ma (e.g. Okudaira et al., 1996), so that thermal conduction from the lower crust, heated up by the transient thermal input from the mantle, can only satisfactorily explain such a prolonged low-P/T type regional metamorphism. Numerical modelling shows that transient thermal anomalies in the mantle can significantly raise the temperature of mid-crustal rocks (Bodorkos et al., 2002) and points to the importance of thermal conduction. We do not deny the importance of thermal input by advection of granitoids, but emphasize the relative importance of thermal conduction from the lower crust compared to the supplementary thermal input by advection of magmatic bodies in the case of the prolonged low-*P*/*T* type regional metamorphism.

Our dataset suggest that start of the Cretaceous flare-up event was controlled by the increase in thermal input from the mantle. Numerical models suggest that about 10 Myr is required for the middle crust to reach the highest-*T* condition after 5 Myr of duration of 1300 ^{o}C in the mantle lithosphere nearly at the bottom of the crust (Bodorkos et al., 2002). Accordingly, the mantle anomaly must have predated the first granitoid pulse. Whether the pattern of granitoid pulses directly reflects a succession of thermal pulses in the mantle or a pulsatile crustal response to a single mantle anomaly (de Silva et al., 2015) remains an important problem to be solved.

Estimating the amount of magma addition to the arc crust is a delicate issue. In the Mikawa area, the 75−69 Ma granitoids are contemporaneous with the Nohi rhyolite, a voluminous volcanic complex consisting of caldera-related felsic rocks (ignimbrites, lavas, volcanoclastic rocks, intrusives etc.) erupted at ca. 70 Ma (U−Pb zircon dating, Hoshi et al., 2016). However, the relative importance of the 75−69 Ma pulse with respect to the older ones is not necessarily higher (Fig. 12). Erosion can be responsible for the loss of a volcanic sequences corresponding to the 99−95 Ma pulse, and the fact that the presently exposed crustal level is subparallel to the intrusion level of the 75−69 Ma pulse plutons might overemphasize the volume of magma added during the last pulse (Figs. 10, 11e). Taken together the magmatic pulses occurring from ca. 99

Ma to ca.69 Ma in the eastern part of the Ryoke belt may reflect transient thermal inputs from the mantle and resulting partial melting of the lower crust to produce the granitoids, and point to a significant addition of continental material into the metasedimentary upper-middle crust of the Eurasian continental margin during the Cretaceous flare-up event.

9. Conclusions

The Cretaceous flare-up event which can be deciphered in the eastern part of the Ryoke belt (SW Japan) reveals the following features and implications for crustal evolution:

(1) Three plutonic pulses occurred at ca. 99−95, ca. 81−75 and ca. 75−69 Ma, with the first granitoid pulse being contemporaneous with the hypersolidus stage of the low-P/T type regional metamorphism (97.0 ± 4.4 Ma to 88.5 ± 2.5 Ma).

(2) In spite of the temporal association, the absence of spatial association between the highest-grade regional metamorphic zone and pre- to syn-metamorphic granitoids supports the presence of a transient thermal anomaly in the mantle and thermal conduction as the main process responsible for the formation of the low-P/T type regional metamorphic zones.

(3) The plutons were successively emplaced in a shallow (< 14 km), deeper (~18−24 km) and shallow (~9−13 km) levels of the crust, with emplacement depths probably controlled by the combination of thermal structural change of the crust and tectonics during granitoid intrusions.

(4) Estimates of the respective volume of magma added during each pulse are biased by the present-day exposures; yet the 75−69 Ma pulse event clearly documents a voluminous addition of granitic material to the arc crust through both plutonic and volcanic activities.

Acknowledgements

We are grateful to T. Okudaira and S. Endo for reviews and M. Scamberulli for editorial efforts. K. Tani, T. Nakajima and K. Suzuki are thanked for discussions on the granitoids of the Ryoke belt. Thanks are also due to K. Horie, M. Takehara, T. Kogiso and Y. Monta for assisting sample preparation and to F. Higashino for assistance in U−Pb zircon dating. This study was financially supported by JSPS KAKENHI Grant No. 26400513 and NIPR general collaboration project No. 28-25 to Kawakami, and by a JSPS postdoctoral fellowship to Skrzypek (Grant No. 25-03715 to T. Hirajima).

References

Adachi, Y., Wallis, S. 2008. Ductile deformation and development of andalusite microstructures in the Hongusan area: constraints on the metamorphism and tectonics of the Ryoke Belt. Island Arc, 17, 41–56.

Akasaki, E., Owada, M., Kamei, A. 2015. Crustal differentiation due to partial melting of granitic

rocks in an active continental margin, the Ryoke Belt, Southwest Japan. Lithos, 230, 82–91.
Asami, M., Hoshino, M., Miyakawa, K., Suwa, K. 1982. Metamorphic conditions of staurolite schists of the Ryoke metamorphic belt in the Hazu-Hongusan area, central Japan. Journal of the Geological Society of Japan, 88, 437–450 (in Japanese with English abstract).
Bodorkos, S., Sandiford, M., Oliver, N.H.S., Cawood, P.A., 2002. High-*T*, low-*P* metamorphism in the Palaeoproterozoic Halls Creek Orogen, northern Australia: the middle crustal response to a mantle-related transient thermal pulse. Journal of Metamorphic Geology, 20, 217–237.
Bosse, V., Boulvais, P., Gautier, P., Tiepolo, M., Ruffet, G., Devidal, J.L., Cherneva, Z., Gerdjikov, I., Paquette, J.L. 2009. Fluid-induced disturbance of the monazite Th-Pb chronometer: In situ dating and element mapping in pegmatites from the Rhodope (Greece, Bulgaria). Chemical Geology, 261, 286–302.
Brown, M. 1998. Unpairing metamorphic belts: P-T paths and a tectonic model for the Ryoke Belt, southwest Japan. Journal of Metamorphic Geology, 16, 3–22.
Brown, M. 2013. Granite: from genesis to emplacement. GSA Bulletin, 125, 1079–1113.
Burov, E., Jaupart, C., Guillou-Frottier, L. 2003. Ascent and emplacement of buoyant magma bodies in brittle-ductile upper crust. Journal of Geophysical Research, 108, 2177, doi:10.1029/2002JB001904.
de Saint Blanquat, M., Horsman, E., Habert, G., Morgan, S., Vanderhaeghe, O., Law, R., Tikoff,

B. 2011. Multiscale magmatic cyclicity, duration of pluton construction, and the paradoxical relationship between tectonism and plutonism in continental arcs. Tectonophysics, 500, 20–33.

De Silva, S.L., Riggs, N.R., Barth, A.P. 2015. Quickening the pulse: Fractal tempos in continental arc magmatism. Elements, 11, 113–118.

Ducea, M., 2001. The California arc: Thick granitic batholiths, eclogitic residues, lithospheric-scale thrusting, and magmatic flare-ups. GSA Today, 11, 4–10.

Ducea, M.N., Paterson, S.R., DeCelles, P.G., 2015, High-volume magmatic events in subduction systems. Elements, 11, 99–104.

Endo, S., Yamasaki, T. 2013. Geology of the Ryoke Plutono-Metamorphic Complex in the Tsukude area, central Japan. Bulletin of the Geological Survey of Japan, 64, 59-84 (in Japanese with English abstract).

Fujiwara, O., Sanga, T., Ohmori, H. 1999. Regional distribution of erosion rates over the Japanese Islands. Japan Nuclear Cycle Technical Review, 5, 85–93 (in Japanese with English abstract).

Geological Survey of Japan, 2015. Seamless digital geological map of Japan 1: 200,000. May 29, 2015 version. Geological Survey of Japan, National Institute of Advanced Industrial Science and Technology (Ed.).

Harayama, S., Koido, Y., Ishizawa, K., Nakai, Y., Kutsukake, T. 1985. Cretaceous to Paleogene

Magmatism in the Chubu District, Japan. Earth Science (Chikyu Kagaku), 39, 345–357 (in Japanese with English abstract).

Hodges, K.V. 2005. Geochronology and thermochronology in orogenic systems. Treatise on Geochemistry, Vol. 3, The Crust, 263–292.

Hoshi, H., Iwano, H., Danhara, T., Sako, K. 2016. U−Pb evidence for rapid formation of the Nohi Rhyolite at about 70 Ma. Abstracts, The 123rd Annual Meeting of the Geological Society of Japan. 81.

Ikeda, T. 1998a. Phase equilibria and the pressure-temperature path of the highest-grade Ryoke metamorphic rocks in the Yanai district, SW Japan. Contributions to Mineralogy and Petrology, 132, 321–335.

Ikeda, T. 1998b. Progressive sequence of reactions of the Ryoke metamorphism in the Yanai district, southwest Japan: the formation of cordierite. Journal of Metamorphic Geology, 16, 39–52.

Ishihara, S., Chappell, B.W. 2007. Chemical compositions of the late Cretaceous Ryoke granitoids of the Chubu District, central Japan-Revisited. Bulletin of the Geological Survey of Japan, 58, 323–350.

Ishihara, S., Terashima, S. 1977. Chemical variation of the Cretaceous granitoids across southwestern Japan -Shirakawa-Toki-Okazaki transection-. Journal of the Geological Society of Japan, 83, 1−18.

Jackson, S.E., Pearson, W.L., Griffin, W.L., Belousova, E.A. 2004. The application of laser ablation-inductively coupled plasma-mass spectrometry to in situ U–Pb zircon geochronology. Chemical Geology, 211, 47–69.

Jaffey, A.H., Flynn, K.F., Glendenin, L.E., Bentleyt, W.C., Essling, A.M. 1971. Precision measurement of half-lives and specific activities of ^{235}U and ^{238}U. Physical Review C, 4, 1889–1906.

Jochum K.P., Brueckner, S.M. 2008. Reference materials in geoanalytical and environmental research - Review for 2006 and 2007. Geostandards and Geoanalytical Research, 32, 405–452.

Kasapoğlu, B., Ersoy, Y.E., Uysal, İ., Palmer, M. R., Zack, T., Koralay, E.O., Karlsson, A. 2016. The petrology of Paleogene volcanism in the Central Sakarya, Nallıhan Region: Implications for the initiation and evolution of post-collisional, slab break-off-related magmatic activity. Lithos, 246-247, 81–98.

Kawakami, T. 2001. Tourmaline breakdown in the migmatite zone of the Ryoke metamorphic belt, SW Japan. Journal of Metamorphic Geology, 19, 61–75.

Kawakami, T., Suzuki, K. 2011. CHIME monazite dating as a tool to detect polymetamorphism in high-temperature metamorphic terrane: Example from the Aoyama area, Ryoke metamorphic belt, Southwest Japan. Island Arc, 20, 439–453.

Kawakami, T., Yamaguchi, I., Miyake, A., Shibata, T., Maki, K., Yokoyama, T.D., Hirata, T. 2013. Behavior of zircon in the upper-amphibolite to granulite facies schist/migmatite transition, Ryoke metamorphic belt, SW Japan: constraints from the melt inclusions in zircon. Contributions to Mineralogy and Petrology, 165, 575–591.

Kawakami, T., Nakano, N., Higashino, F., Hokada, T., Osanai, Y., Yuhara, M., Charusiri, P., Kamikubo, H., Yonemura, K., Hirata, T. 2014. U–Pb zircon and CHIME monazite dating of granitoids and high-grade metamorphic rocks from the Eastern and Peninsular Thailand – A new report of Early Paleozoic granite. Lithos, 200–201, 64–79.

Kawano, Y., Ueda, Y., 1967. Periods of the igneous activities of the granitic rocks in Japan by K-A dating method. Tectonophysics, 4, 523–530.

Kinoshita, O., 1995. Migration of igneous activities related to ridge subduction in Southwest Japan and the East Asian continental margin from the Mesozoic to the Paleogene. Tectonophysics, 245, 25–35.

Kretz, R. 1983. Symbols for rock-forming minerals. American mineralogist 68, 277-9.

Kutsukake, T. (1993). An initial continental margin plutonism -Cretaceous Older Ryoke granitoids, southwest Japan. Geological Magazine, 130, 15–28.

Ludwig, K. 2012. User's manual for Isoplot version 3.75–4.15: a geochronological toolkit for Microsoft Excel. Berkley Geochronological Center Special Publication 5.

Lukács, R., Harangi, S., Bachmann, O., Guillong, M., Danišík, M., Buret, Y., von Quadt, A., Dunkl, I., Fodor, L., Sliwinski, J., Soós, I., Szepesi, J. 2015. Zircon geochronology and geochemistry to constrain the youngest eruption events and magma evolution of the Mid-Miocene ignimbrite flare-up in the Pannonian Basin, eastern central Europe. Contributions to Mineralogy and Petrology, 170, 52. doi 10.1007/s00410-015-1206-8

Makimoto, H., Yamada, N., Mizuno, K., Takada, A., Komazawa, M., Sudo, S. 2004. Geological map of Japan 1: 200,000, Toyohashi and Irago Misaki. Geological Survey of Japan (in Japanese with English abstract).

Masumoto, Y., Enami, M., Tsuboi, M., Hong, M. 2014. Magmatic zoisite and epidote in tonalite of the Ryoke belt, central Japan. European Journal of Mineralogy, 26, 279–291.

Miyake, A., Hirukawa, T., Sato, M., Taguchi, T., Suzuki, K., Nakai, Y. 2016. Large thermal aureole around the Inagawa Granodiorite in the southeastern area of Asuke, Aichi Prefecture. Journal of the Geological Society of Japan, 122, 173–191 (in Japanese with English abstract).

Miyake, A., Igarashi, Y., Inaishi, T., Taguchi, T. 2017, Finding of staurolite-bearing pelitic schists in the Ryoke metamorphic belt of the Dando-san area, Aichi Prefecture and its significance. Journal of the Geological Society of Japan, 123, 59–72 (in Japanese with English abstract).

Miyake, A., Murata, E., Morishita, O. 1992. Growth stages of andalusite in the Ryoke metamorphic rocks from the Nukata area, Aichi Prefecture. Journal of Mineralogy, Petrology and Economic Geology, 87, 475–480 (in Japanese with English abstract).

Miyake, A., Yokoe, K., Suzuki, B., Igarashi, Y. 2014. The thermal structures in the Ryoke metamorphic belt of the Dando-san area, Aichi Prefecture. Journal of Geological Society of Japan, 120, 299–312 (in Japanese with English abstract).

Miyashiro, A. 1961. Evolution of metamorphic belts. Journal of Petrology, 2, 277–311.

Miyazaki, K. 2010. Development of migmatites and the role of viscous segregation in high-T metamorphic complexes: Example from the Ryoke Metamorphic Complex, Mikawa Plateau, Central Japan. Lithos, 116, 287–299.

Miyazaki, K., Nishioka, Y., Nakashima, R., Ozaki, M. 2008. Geology of the Goyu district. Quadrangle Series, 1:50,000. Geological Survey of Japan (in Japanese with English abstract).

Morishita, T., Suzuki, K. 1993. XRF analyses of the Mitsuhashi Granite in the Shitara area, Aichi Prefecture. Bulletin of the Nagoya University Furukawa Museum, 9, 77−90 (in Japanese with English abstract).

Morishita, T., Suzuki, K. 1995. CHIME ages of monazite from the Shinshiro Tonalite of the Ryoke belt in the Mikawa area, Aichi Prefecture. The Journal of earth and planetary sciences, Nagoya University, 42, 45–53.

Morishita, T., Suzuki, K., Nasu, T. 1996. CHIME ages of monazite from granitoids in the Mikawa-Tono area, central Japan. Geological Society of Japan The 103rd Annual Meeting, Abstract

Volume. p. 282 (in Japanese).

Murakami, M., Kosler, J., Takagi, H., Tagami, T. 2006. Dating pseudotachylyte of the Asuke Shear Zone using zircon fission-track and U–Pb methods. Tectonophysics, 424, 99–107.

Nakai, Y. 1976. Petrographical and petrochemical studies of the Ryoke granites in the Mikawa-Tono district, central Japan. Bulletin of Aichi University of Education (Natural Science), 25, 97−112.

Nakai, Y. 1982. The Busetsu granite in the Ryoke belt, Central Japan. Geological Society of Japan The 89th Annual Meeting, Abstract Volume. p. 404 (in Japanese).

Nakai, Y., Suzuki, K. 1996. CHIME monazite ages of the Kamihara Tonalite and the Tenryukyo Granodiorite in the eastern Ryoke belt of central Japan. Journal of the Geological Society of Japan, 102, 431–439.

Nakai, Y., Suzuki, K. 2003. Post-tectonic two-mica granite in the Okazaki area, central Japan: a field guide for the 2003 Hutton Symposium. Hutton Symposium, V, Field Guidebook, Geological Survey of Japan, Interim-Report,28, 115–124.

Nakajima, T. 1994. The Ryoke plutonometamorphic belt: crustal section of the Cretaceous Eurasian continental margin. Lithos, 33, 51–66.

Nakajima, T. 1996. Cretaceous granitoids in SW Japan and their bearing on the crust-forming process in the eastern Eurasian margin. Transactions of the Royal Society of Edinburgh: Earth

Science, 87, 183–191.

Nakajima, T., Horie, K., Adachi, T., Miyazaki, K., Dunkley, D.J., Hokada, T. 2013. SHRIMP U–Pb ages of zircons from Ryoke metamorphic rocks. Geological Society of Japan The 120th Annual Meeting, Abstract Volume. p. 51 (in Japanese).

Nakajima, T., Kamiyama, H., Williams, I.S., Tani, K. 2004. Mafic rocks from the Ryoke Belt, southwest Japan: implications for Cretaceous Ryoke/San-yo granitic magma genesis. Geological Society of America Special Papers, 389, 249–263.

Nakashima, R., Hori, N., Miyazaki, K., Nishioka, Y. 2008. Geology of the Toyohashi and Tahara districts. Quadrangle Series, 1:50,000. Geological Survey of Japan (in Japanese with English abstract).

Nozawa, T., 1975. Radiometric age map of Japan: Granite. Geological Map of Japan 1:2,000,000, Map Series.

Ohtomo, Y. 1985. Zonal structure of the Shinshiro Tonalite pluton. MAGMA 73, 69–73 (in Japanese).

Okudaira, T., Hara, I., Sakurai, Y., Hayasaka, Y. 1993. Tectono-metamorphic processes of the Ryoke belt in the Iwakuni-Yanai district, southwest Japan. Memoirs of the Geological Society of Japan, 42, 91–120.

Okudaira, T. 1996. Thermal evolution of the Ryoke metamorphic belt, southwest Japan: Tectonic and numerical modeling. Island Arc, 5, 373–385.

Otamendi, J.E., Ducea, M.N., Bergantz, G.W. 2012. Geological, petrological and geochemical evidence for progressive construction of an arc crustal section, Sierra de Valle Fertil, Famatinian Arc, Argentina. Journal of Petrology, 53, 761–800.

Ozima, M., Ueno, N., Shimizu, N., Kuno, H. 1967. Rb–Sr and K–Ar isotopic investigations of Sidara granodiorites and the associated Ryoke metamorphic belt, central Japan. Japanese Journal of Geology and Geography, 38, 159–162.

Paterson, S.R., Ducea, M.N., 2015, Arc magmatic tempos: Gathering the evidence. Elements, 11, 91–97.

Pearce, N.J., Perkins, W.T., Westgate, J.A., Gorton, M.P., Jackson, S.E., Neal, C.R., Chenery, S.P. 1997. A compilation of new and published major and trace element data for NIST SRM 610 and NIST SRM 612 glass reference materials. Geostandards newsletter, 21, 115–144.

Petri, B., Skrzypek, E., Mohn, G., Mateeva, T., Robion, P., Schulmann, K., Manatschal, G., Müntener, O. 2017. Mechanical anisotropies and mechanisms of mafic magma ascent in the middle continental crust: The Sondalo magmatic system (N Italy). GSA Bulletin. in press.

Roberts, M.P., Finger, F., 1997. Do U-Pb zircon ages from granulites reflect peak metamorphic conditions? Geology, 25, 319–322.

Rubatto, D. 2002. Zircon trace element geochemistry: partitioning with garnet and the link between U–Pb ages and metamorphism. Chemical geology, 184, 123–138.

Ryoke Research Group. 1972. The mutual relations of the granitic rocks of the Ryoke metamorphic belt in central Japan. Earth Science (Chikyu Kagaku), 26, 205-216 (in Japanese with English abstract).

Sakata, S., Hattori, K., Iwano, H., Yokoyama, T.D., Danhara, T., Hirata, T. 2014. Determination of U–Pb Ages for Young Zircons using Laser Ablation-ICP-Mass Spectrometry Coupled with an Ion Detection Attenuator Device. Geostandards and Geoanalytical Research, 38, 409–420.

Sato, D., Matsuura, H., Yamamoto, T. 2016. Timing of the Late Cretaceous ignimbrite flare-up at the eastern margin of the Eurasian Plate: New zircon U–Pb ages from the Aioi–Arima–Koto region of SW Japan. Journal of Volcanology and Geothermal Research, 310, 89–97.

Schmidt, M.W. 1992. Amphibole composition in tonalite as a function of pressure: an experimental calibration of the Al-in-hornblende barometer. Contributions to mineralogy and petrology, 110, 304–310.

Schubert, M., Driesner, T., Gerya, T.V., Ulmer, P. 2013. Mafic injection as a trigger for felsic magmatism: A numerical study, Goechemistry, Geophysics, Geosystematics, 14, 1910–1928, doi:10.1002/ggge.20124.

Seydoux-Guillaume, A.M., Paquette, J.L., Wiedenbeck, M., Montel, J.M., Heinrich, W. 2002. Experimental resetting of the U–Th–Pb systems in monazite. Chemical Geology, 191, 165–

181.

Shibata, K., Ishihara, S. 1979a. Initial $^{87}Sr/^{86}Sr$ ratios of plutonic rocks from Japan. Contributions to Mineralogy and Petrology, 70, 381–390.

Shibata, K., Ishihara, S. 1979b. Rb-Sr whole-rock and K-Ar mineral ages of granitic rocks in Japan. Geochemical Journal, 13, 113–119.

Skrzypek, E., Kato, T., Kawakami, T., Sakata, S., Hattori, K., Hirata, T., Ikeda, T. 2018. Monazite behavior and time-scale of metamorphic processes along a low-pressure/high-temperature field gradient (Ryoke belt, SW Japan). Journal of Petrology, in press.

Skrzypek, E., Kawakami, T., Hirajima, T., Sakata, S., Hirata, T., Ikeda, T. 2016. Revisiting the high temperature metamorphic field gradient of the Ryoke Belt (SW Japan): New constraints from the Iwakuni-Yanai area. Lithos, 260, 9–27.

Sláma, J., Košler, J., Condon, D.J., Crowley, J.L., Gerdes, A., Hanchar, J.M., Horstwood, M.S.A., Morris, G.A., Nasdala, L., Norberg, N., Schaltegger, U., Schoene, B., Tubrett, M.N., Whitehouse, M.J. 2008. Plešovice zircon - A new natural reference material for U–Pb and Hf isotopic microanalysis. Chemical Geology, 249, 1–35.

Suzuki, K., Adachi, M., 1998. Denudation history of the high T/P Ryoke metamorphic belt, southwest Japan: constraints from CHIME monazite ages of gneisses and granitoids. Journal of Metamorphic Geology, 16, 23–37.

Suzuki, K., Adachi, M., Kajizuka, I., 1994a. Electron microprobe observations of Pb diffusion in metamorphosed detrital monazites. Earth and Planetary Science Letters, 128, 391–405.

Suzuki, K., Morishita, T., Kajizuka, I., Nakai, Y., Adachi, M., Shibata, K., 1994b. CHIME ages of monazites from the Ryoke metamorphic rocks and some granitoids in the Mikawa-Tono area, central Japan. Bulletin of the Nagoya University Furukawa Museum, 10, 7–38 (in Japanese with English abstract).

Tani, K., Horie, K., Dunkley, D., Ishihara, S., 2014. Pulsed granitic crust formation revealed by comprehensive SHRIMP zircon dating of the SW Japan granitoids. Abstract of Japan Geoscience Union Meeting. Yokohama, 2014.

Takatsuka, K., Kawakami, T., Skrzypek, E., Sakata, S., Obayashi, H., Hirata, T., 2018, Age gap between the intrusion of gneissose granitoids and regional high-temperature metamorphism in the Ryoke belt (Mikawa area, central Japan). Island Arc, 27, e12224. DOI: 10.1111/iar.12224.

Tibaldi, A.M., Otamendi, J.E., Cristofolini, E.A., Baliani, I., Walker, B.A., Bergantz, G.W., 2013. Reconstruction of the Early Ordovician Famatinian arc through thermobarometry in lower and middle crustal exposures, Sierra de Valle Fértil, Argentina. Tectonophysics, 589, 151–166.

Togashi, S., Imai, N., Okuyama-Kusunose, Y., Tanaka, T., Okai, T., Koma, T., Murata, Y., 2000. Young upper crustal chemical composition of the orogenic Japan Arc. Geochemistry Geophysics Geosystems, 1, 2000GC000083.

Tsuboi, M., Asahara, Y., 2009. Initial $^{87}Sr/^{86}Sr$ ratio heterogeneity in Kamihara Tonalite, Ryoke belt, southwest Japan: Evidence from strontium isotopic analysis of apatite. Journal of Mineralogical and Petrological Sciences, 104, 226−233.

Tunheng, A., Hirata, T., 2004. Development of signal smoothing device for precise elemental analysis using laser ablation-ICP-mass spectrometry. Journal of Analytical Atomic Spectrometry, 19, 932–934.

Uchiumi, S., Uto, K., Shibata, K., 1990. K–Ar age results — 3 — New data from the Geological Survey of Japan. Bulletin of the Geological Survey of Japan, 41, 567–575 (in Japanese with English abstract).

Ueno, N., Ozima, M., Ono, A., 1969. Geochronology of the Ryoke metamorphism—Rb–Sr, K–Ar isotopic investigations of the metamorphic rocks in the Ryoke metamorphic belt—. Geochemical Journal, 3, 35–44.

Vigneresse, J.-L., Clemens, J.D., 2000. Granitic magma ascent and emplacement: neither diapirism nor neutral buoyancy. In: Vendeville, B., Mart, Y. & Vingeresse, J.-L. (eds) Salt, Shale and Igneous Diapirs in and around Europe. Geological Society, London, Special Publications, 174, 1–19.

Wakita, K., 1987. The occurrence of Latest Jurassic-Earliest Cretaceous radiolarians at the Hida-Kanayama area in the Mino terrane, central Japan. Journal of the Geological Society of Japan, 93, 441–443 (in Japanese).

Waters, D.J., Lovegrove, D.P., 2002. Assessing the extent of disequilibrium and overstepping of prograde metamorphic reactions in metapelites from the Bushveld Complex aureole, South Africa. Journal of Metamorphic Geology, 20, 135–149.

Wiedenbeck, M., Alle, P., Corfu, F., Griffin, W.L., Meier, M., et al., 1995. Three natural zircon standards for U–Th–Pb, Lu–Hf, trace element and REE analyses. Geostandards Newsletter, 19, 1–23.

Wiedenbeck, M., Hanchar, J.M., Peck, W.H., Sylvester, P., Valley, J., et al., 2004. Further characterisation of the 91500 zircon crystal. Geostandards and Geoanalytical Research, 28, 9–39.

Yamasaki, T., 2013. K–Ar ages of the Ryoke plutonic rocks in the Asuke area, Aichi prefecture, central Japan. Journal of the Geological Society of Japan, 119, 421–431 (in Japanese with English abstract).

Yamasaki, T., Ozaki, M., 2012. Geology of the Asuke district. Quadrangle Series, 1:50,000. Geological Survey of Japan (in Japanese with English abstract).

Figure captions

Fig. 1. (a) Simplified geological map showing the location of the Ryoke belt across Japan. (b)

Geological map of the Ryoke belt in central Japan with metamorphic zones. Sample localities of granitoids and a metamorphic rock (GY92A) are indicated. The geological map is compiled and modified after Makimoto et al. (2004), Miyazaki et al. (2008), Nakashima et al. (2008), Miyazaki (2010), Yamasaki and Ozaki (2012), Endo and Yamasaki (2013), the Geological Survey of Japan (2015), Miyake et al. (2016) and Takatsuka et al. (2018). MTL; Median Tectonic Line. ISTL; Itoigawa-Shizuoka Tectonic Line. Mineral abbreviations are after Kretz (1983).

Fig. 2. Field occurrence and slab photographs of granitoid samples used for U−Pb zircon dating. (a) Outcrop of the Shinshiro tonalite (GY50A) showing ellipsoidal mafic enclaves (dark color) elongated parallel to the gneissose structure. Surface is partly green because of moss. (b) Slab photograph of the Shinshiro tonalite (sample GY100A) showing a gneissose structure defined by the arrangement of Hbl + Bt. (c) Slab photograph of the Mitsuhashi granodiorite (sample GY99A) showing a gneissose structure defined by the arrangement of Hbl + Bt. (d, e) Slab photographs of the Inagawa granite: sample GY86A from the gneissose porphyritic facies and sample GY93A from the massive facies. (f, g) Field occurrence of the Busetsu granite: (f) Xenolith of pelitic schist in garnet-bearing, fine-grained granite. (g) Intrusion boundary of fine-grained granite and meta-sandstone. Foliation of the meta-sandstone is oblique to the boundary. (h) Slab photograph of the Busetsu granite (sample

GY89A) showing a gneissose structure and K-feldspar megacrysts. (i) Field occurrence of ~20 cm thick leucosome (GY03D) subparallel to the migmatitic banding of the psammitic metatexite. (j) Field occurrence of pegmatite sample GY47A (white). Mafic lens is present above the pegmatite.

Fig. 3. Photomicrographs of granitoid and pelitic gneiss samples. (a, b) Samples GY50A and GY100A from the Shinshiro tonalite showing the mode of occurrence of zircon and allanite (plane polarized light, PPL). (c) Sample GY99A from the Mitsuhashi granodiorite showing the mode of occurrence of zircon (PPL). (d, e) Samples GY86A and GY93A from the Inagawa granite showing the mode of occurrence of zircon and allanite (PPL) (f, g) Samples GY51A and MK02M from the Busetsu granite (PPL) showing the mode of occurrence of zircon. These samples are characterized by the presence of garnet and muscovite. (h) Sample GY89A from the Busetsu granite (crossed polarized light, CPL) showing a gneissose structure defined by the arrangement of Bt + Ms, and dynamic recrystallization of quartz in elongated layers. (i) Pelitic gneiss (sample GY92A1) from a km-wide band of metasedimentary rocks in between the Kamihara and Busetsu plutons. Andalusite with a chiastolite texture (partly transformed to sillimanite) is replaced by pinitized cordierite at the rim. The main foliation defined by the arrangement of biotite and fibrolite is deflected around the andalusite porphyroblast. See text for details. PPL. (j) CPL of (i). (k) Thin section photo

of leucosome sample GY03D. CPL. (l) Thin section photo of pegmatite sample GY47A. Fine-grained myrmekite is abundant along grain boundaries of K-feldspar, where sillimanite and secondary muscovite is also common. CPL.

Fig. 4. Cathodoluminescence images of representative zircon grains showing analyzed spots and results of U–Pb dating. Concordant and discordant data are shown in yellow and white characters, respectively. Results are labeled with spot number, $^{206}Pb/^{238}U$ age ± 2σ error (Ma), and concordance in parenthesis (%). Scale bars represent 20 μm. (a–f) Shinshiro tonalite samples (GY50A and GY100A), (g, h) Mitsuhashi granodiorite sample (GY99A), (i–l) Inagawa granite samples (GY86A and GY93A).

Fig. 5. Cathodoluminescence and BSE images of representative zircon grains from the Busetsu granite (samples GY51A, MK02M and GY89A) with analyzed spots and results of U–Pb dating. Concordant and discordant data are shown in yellow and white characters, respectively. Results are labeled with spot number, $^{206}Pb/^{238}U$ age ± 2σ error (Ma), Th/U ratio, and concordance in parenthesis (%). Alphabets representing the domain name (B, C or D) are also added to (b–i). Scale bars represent 20 μm. (a) Zircon with domain A alone (b–d) Zircons with inherited core, domain B and domain D. Red arrows indicate sillimanite inclusions. (e–g) Zircons with domains B and C. (h, i) Zircons with domains C and D. (j–m) Zircons with domain D alone. See text for detailed explanation of the domains. A histogram

and relative probability diagram for ^{206}Pb/^{238}U ages obtained with all Busetsu granite samples (GY51A, MK02M and GY89A, concordant data only) is also shown.

Fig. 6. Cathodoluminescence and BSE images of representative zircon grains from a migmatite leucosome sample GY03D. Scale bars represent 20 μm.

Fig. 7. Cathodoluminescence and BSE images of representative zircon grains from a pegmatite sample GY47A. Scale bars represent 20 μm.

Fig. 8. Concordia diagrams for U–Pb zircon dating results for (a, b) Shinshiro tonalite (samples GY50A and GY100A), (c) Mitsuhashi granodiorite (sample GY99A), (d, e) Inagawa granite (samples GY86A and GY93A), and (f–h) Busetsu granite (samples GY51A, MK02M and GY89A). Concordant and discordant data are plotted together for each sample. Rejected data (See Table S2 and text for details) are not shown.

Fig. 9. Relative probability diagrams, concordia diagrams and U-concentration vs age plot for U–Pb zircon dating of migmatites and a pegmatite. (a) Relative probability diagram for sample GY03D. (b) Concordia diagram for sample GY03D. (c) U-concentration (ppm) vs ^{206}Pb/^{238}U age ± 2σ error (Ma) plot for sample GY03D. (d) Th/U ratio vs ^{206}Pb/^{238}U age ± 2σ error (Ma) plot for sample GY03D. (e) Concordia diagram for sample GY47A. (f) Relative probability diagram for sample GY47A.

Fig. 10. Summary of U–Pb zircon ages and spatial distribution of plutonic rocks in the Mikawa

area (This study; Takatsuka et al., 2018; Tani et al., 2014; Nakajima et al., 2004; Murakami et al., 2006). U−Pb zircon ages are shown as $^{206}Pb/^{238}U$ ages with 2σ uncertainties. Also shown are pressure estimates of granitoid crystallization by Al-in-hornblende barometry (This study; Masumoto et al., 2014) and $P-T$ estimates for contact metamorphism around the 75−69 Ma granitoids (Shinshiro tonalite, Mitsuhashi granodiorite, Inagawa granite and Busetsu granite) (This study; Adachi and Wallis, 2007; Endo and Yamasaki, 2013; Miyake et al., 1992; 2016).

Fig. 11. Schematic drawings summarizing the plutono-metamorphic evolution of the Ryoke belt in the Mikawa area. Note that different colors of zircon illustrations in different phases of granitoids finally appears altogether in the Busetsu granite. (a) ca. 99−95Ma: Emplacement of granitoids in a shallow part of the accretionary complex. Zircon in the 99−95 Ma granitoids is shown in blue. (b) ca. 95−85 Ma: High-*T* regional metamorphism and partial melting at depth. Leucosomes and metamorphic zircon (shown in gray) form in the migmatitic Grt−Crd zone. (c) ca. 81 Ma: Emplacement of the gneissose granitoids in the middle crust. Zircon in 81−75 Ma granitoids is shown in orange. (d) ca. 75 Ma: Late-magmatic (and probably syn-tectonic) exhumation of the high-grade metamorphic zones; the regional metamorphic zonation is tilted toward the north. (e) ca. 75−69 Ma: emplacement of the 75−69 Ma granitoids at shallow crustal level. Inset shows the complex zircon record in

the Busetsu granite. Zircon crystal shown by pink is a direct crystallization product from the Busetsu granite, and zircons sourced from other plutons and metamorphic rocks has pink rims representing the overgrowth during the crystallization of the Busetsu granite.

Fig. 12. Relative probability diagram of surface exposure of granitoids plotted against U−Pb zircon ages for the Mikawa and Yanai areas (this study; Skrzypek et al., 2016; in press; Takatsuka et al., 2018). Note the scale difference between two areas. Time periods shaded in gray (*HT*) represent the duration of high-*T* metamorphism in each area, estimated based on the age range of metamorphic zircons (this study; Skrzypek et al., 2016). Although not shown in the figure, the central part of the Hiroshima Granite around Hiroshima and Kabe regions (~40 km east of the Yanai area) are reported to give zircon U-Pb ages of 87.3 ± 0.9 to 85.6 ± 1.0 Ma (Tani et al., 2014). See Table S5 for data and a detailed method used to construct this figure.

Table 1. Summary of published geochronological data for granitoids in the Mikawa area.

Table 2. Summary of U−Pb zircon dating results for granitoids, migmatite and pegmatite in the Mikawa area obtained in this study.

Table S1. Instrumentation and operational settings for LA−ICP−MS analyses.

Table S2. Results of LA−ICP−MS U−Pb zircon dating.

Table S3. Representative amphibole analyses from sample GY33A.

Table S4. Representative amphibole analyses from sample GY81B.

Table S5. Dataset used for constructing Fig. 8 and explanatory text of its construction method.

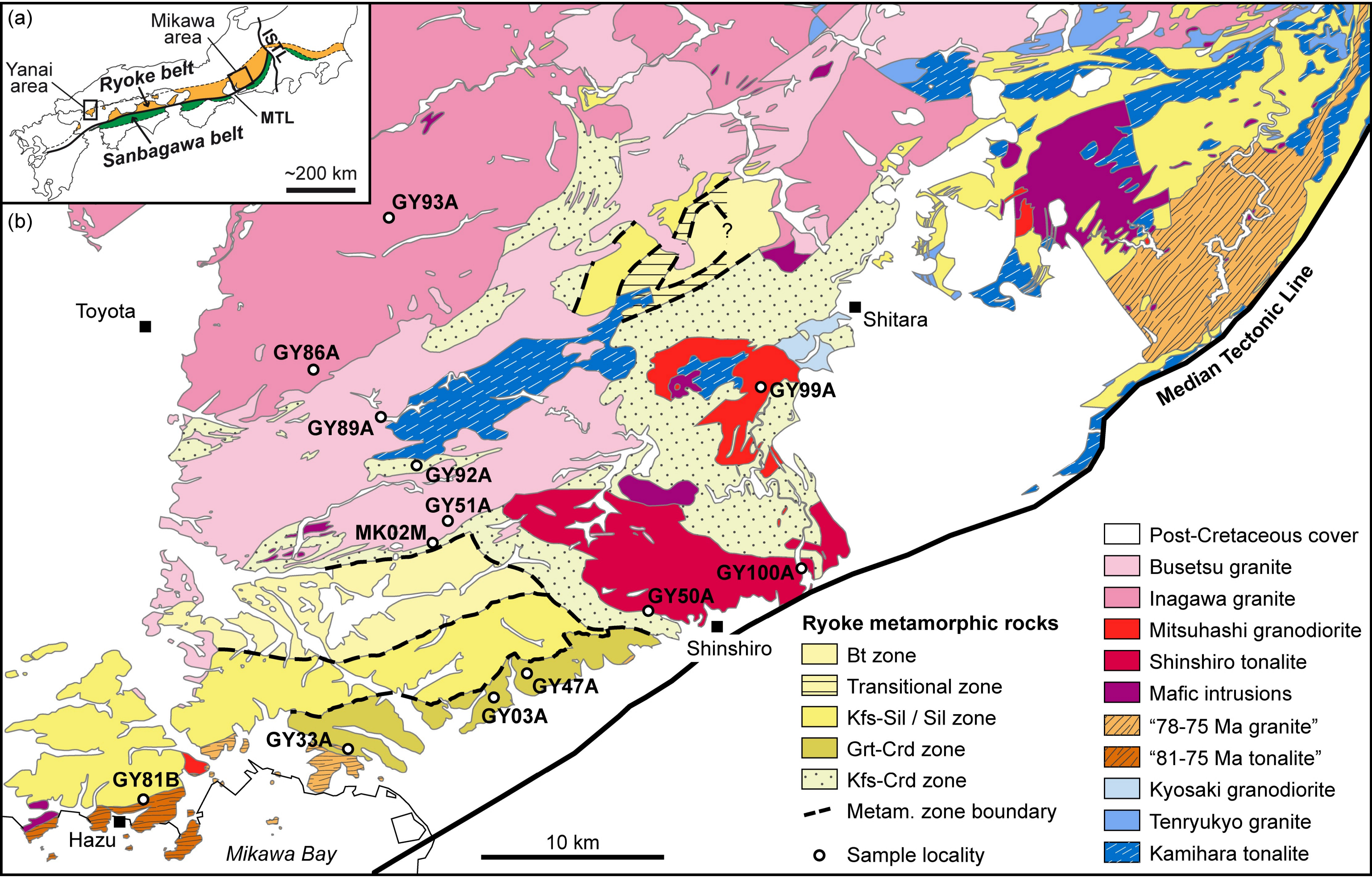
(a)
Mikawa area
Yanai area
Ryoke belt
ISTL
MTL
Sanbagawa belt
~200 km
(b)
GY93A
Toyota
GY86A
GY89A
GY92A
GY51A
MK02M
GY99A
Shitara
Median Tectonic Line
GY100A
GY50A
Shinshiro
GY47A
GY03A
GY33A
GY81B
Hazu
Mikawa Bay
10 km
Ryoke metamorphic rocks
Bt zone
Transitional zone
Kfs-Sil / Sil zone
Grt-Crd zone
Kfs-Crd zone
Metam. zone boundary
Sample locality
Post-Cretaceous cover
Busetsu granite
Inagawa granite
Mitsuhashi granodiorite
Shinshiro tonalite
Mafic intrusions
"78-75 Ma granite"
"81-75 Ma tonalite"
Kyosaki granodiorite
Tenryukyo granite
Kamihara tonalite

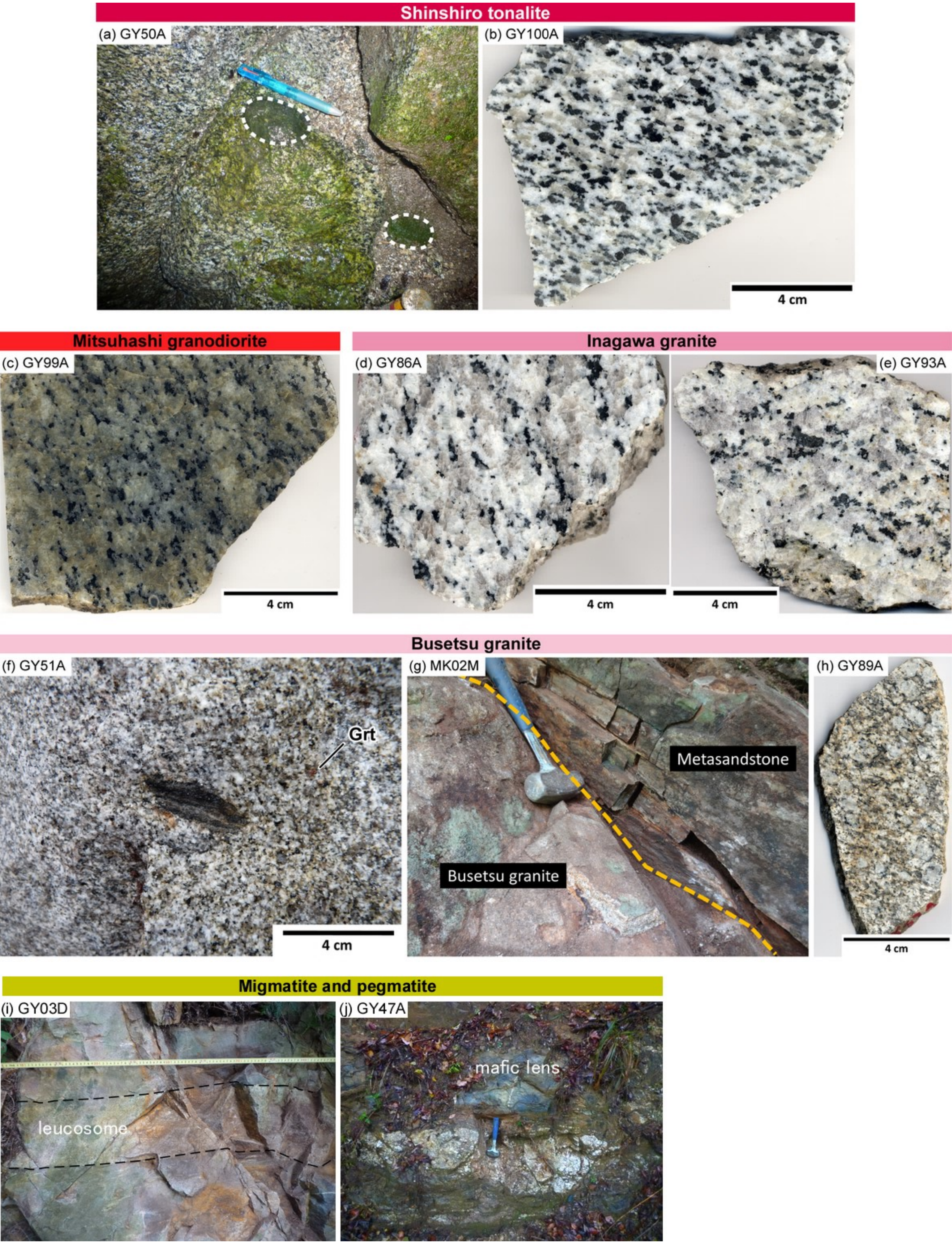
Shinshiro tonalite
(a) GY50A
(b) GY100A
4 cm
Mitsuhashi granodiorite
(c) GY99A
4 cm
Inagawa granite
(d) GY86A
(e) GY93A
4 cm
4 cm
Busetsu granite
(f) GY51A
Grt
4 cm
(g) MK02M
Metasandstone
Busetsu granite
(h) GY89A
4 cm
Migmatite and pegmatite
(i) GY03D
leucosome
(j) GY47A
mafic lens

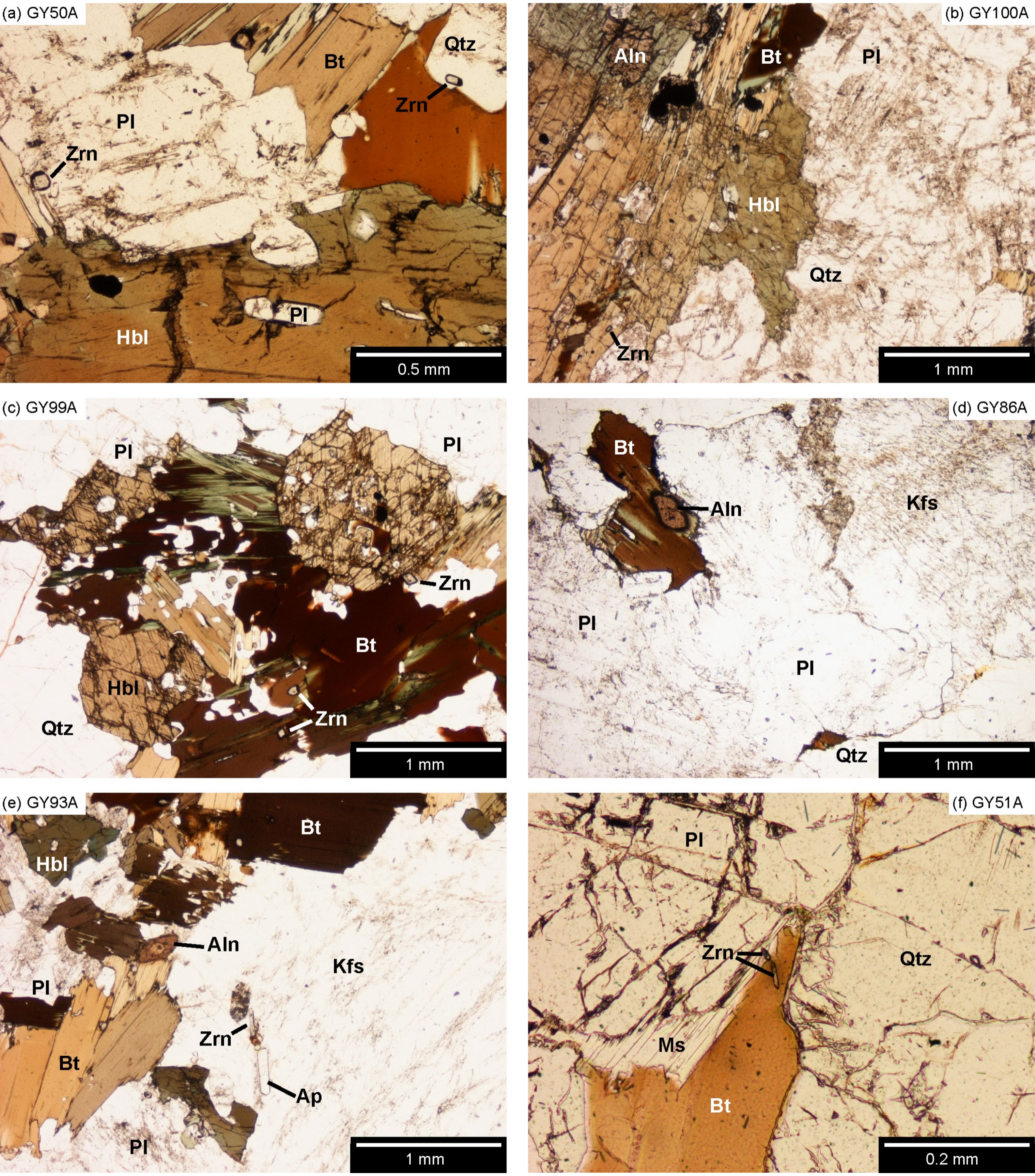
(a) GY50A
Qtz
Bt
Zrn
Pl
Zrn
Pl
Hbl
0.5 mm
(b) GY100A
Aln
Bt
Pl
Hbl
Qtz
Zrn
1 mm
(c) GY99A
Pl
Pl
Zrn
Bt
Hbl
Zrn
Qtz
1 mm
(d) GY86A
Bt
Aln
Kfs
Pl
Pl
Qtz
1 mm
(e) GY93A
Bt
Hbl
Aln
Kfs
Pl
Zrn
Bt
Ap
Pl
1 mm
(f) GY51A
Pl
Zrn
Qtz
Ms
Bt
0.2 mm

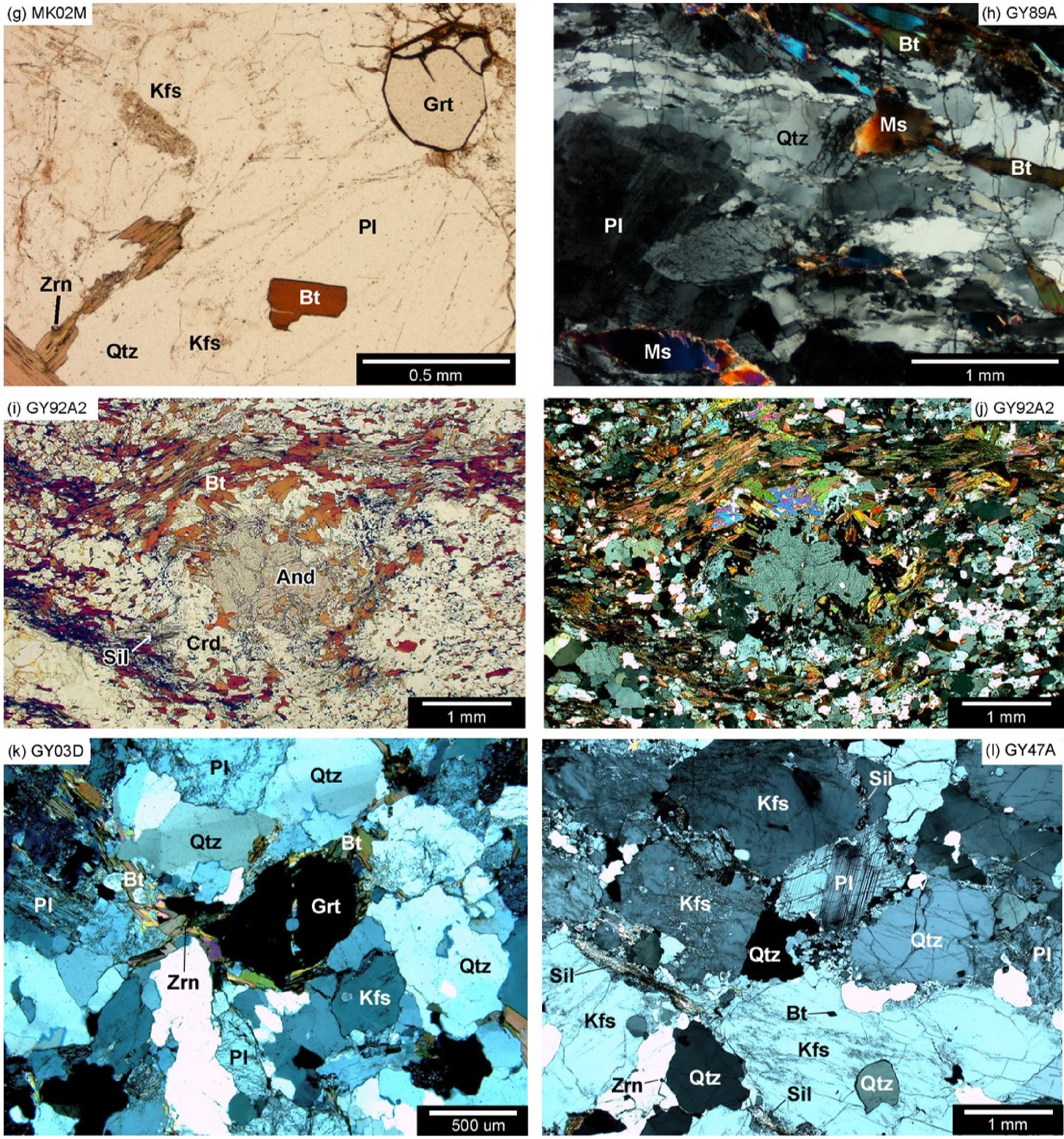
(g) MK02M
Kfs
Grt
Pl
Zrn
Bt
Qtz
Kfs
0.5 mm
(h) GY89A
Bt
Ms
Qtz
Bt
Pl
Ms
1 mm
(i) GY92A2
Bt
And
Sil
Crd
1 mm
(j) GY92A2
1 mm
(k) GY03D
Pl
Qtz
Qtz
Bt
Bt
Pl
Grt
Zrn
Qtz
Kfs
Pl
500 um
(l) GY47A
Sil
Kfs
Pl
Kfs
Qtz
Qtz
Sil
Pl
Bt
Kfs
Kfs
Zrn
Qtz
Sil
Qtz
1 mm

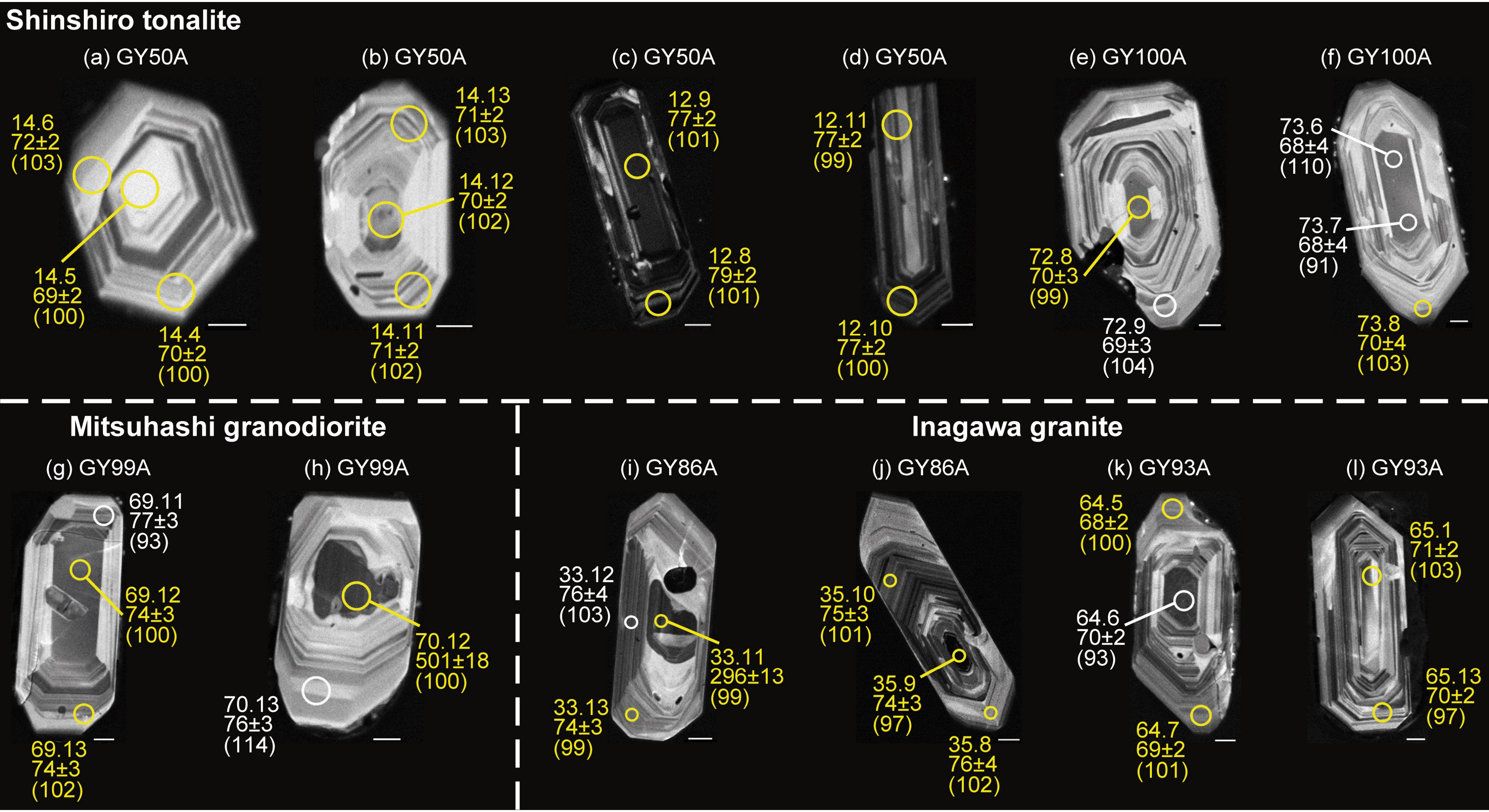

Shinshiro tonalite
(a) GY50A
14.6
72±2
(103)
14.5
69±2
(100)
14.4
70±2
(100)
(b) GY50A
14.13
71±2
(103)
14.12
70±2
(102)
14.11
71±2
(102)
(c) GY50A
12.9
77±2
(101)
12.8
79±2
(101)
(d) GY50A
12.11
77±2
(99)
12.10
77±2
(100)
(e) GY100A
72.8
70±3
(99)
72.9
69±3
(104)
(f) GY100A
73.6
68±4
(110)
73.7
68±4
(91)
73.8
70±4
(103)
Mitsuhashi granodiorite
(g) GY99A
69.11
77±3
(93)
69.12
74±3
(100)
69.13
74±3
(102)
(h) GY99A
70.12
501±18
(100)
70.13
76±3
(114)
Inagawa granite
(i) GY86A
33.12
76±4
(103)
33.11
296±13
(99)
33.13
74±3
(99)
(j) GY86A
35.10
75±3
(101)
35.9
74±3
(97)
35.8
76±4
(102)
(k) GY93A
64.5
68±2
(100)
64.6
70±2
(93)
64.7
69±2
(101)
(l) GY93A
65.1
71±2
(103)
65.13
70±2
(97)

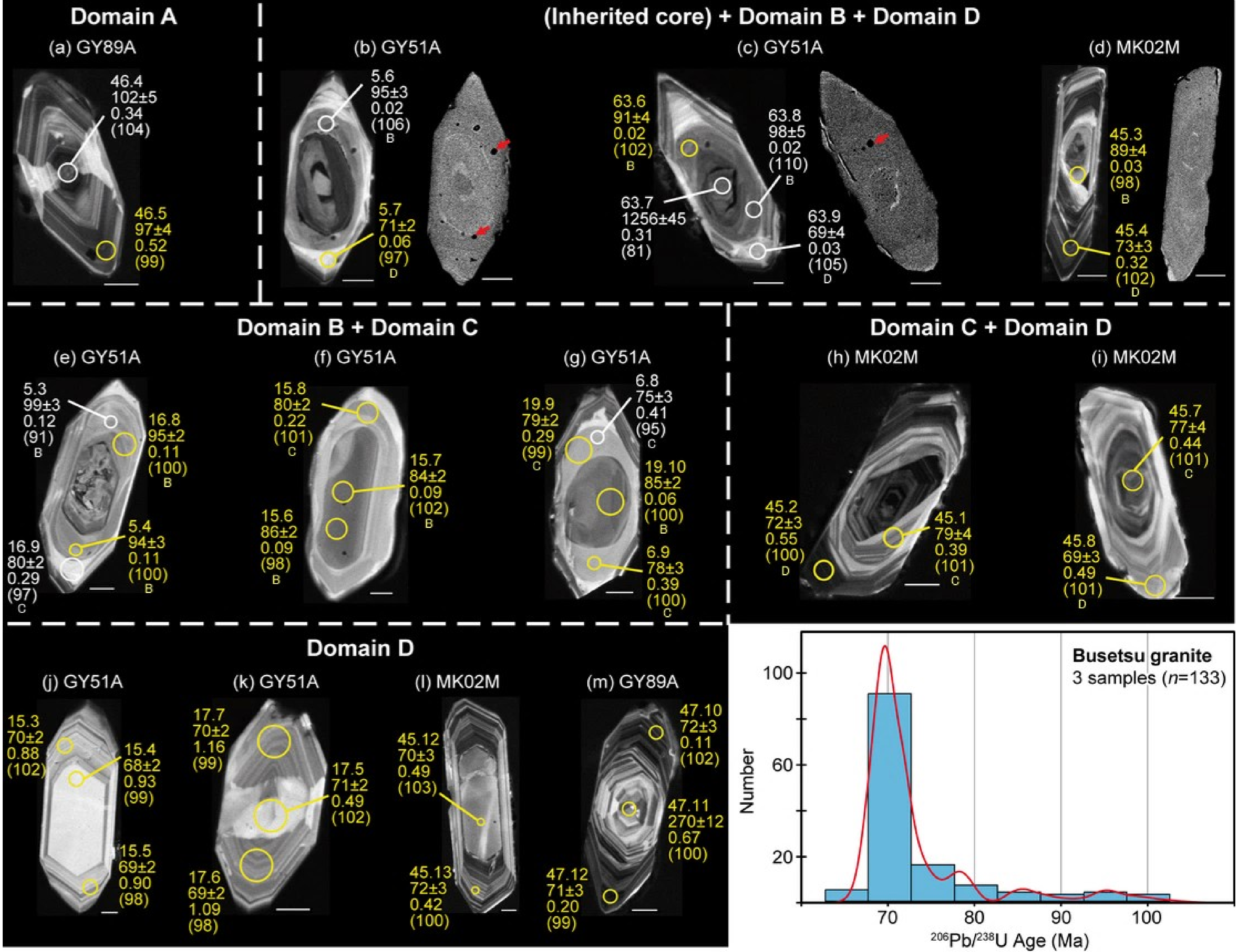
Domain A
(a) GY89A
46.4
102±5
0.34
(104)
46.5
97±4
0.52
(99)
(Inherited core) + Domain B + Domain D
(b) GY51A
5.6
95±3
0.02
(106)
B
5.7
71±2
0.06
(97)
D
(c) GY51A
63.6
91±4
0.02
(102)
B
63.8
98±5
0.02
(110)
B
63.7
1256±45
0.31
(81)
63.9
69±4
0.03
(105)
D
(d) MK02M
45.3
89±4
0.03
(98)
B
45.4
73±3
0.32
(102)
D
Domain B + Domain C
(e) GY51A
5.3
99±3
0.12
(91)
B
16.8
95±2
0.11
(100)
B
5.4
94±3
0.11
(100)
B
16.9
80±2
0.29
(97)
C
(f) GY51A
15.8
80±2
0.22
(101)
C
15.7
84±2
0.09
(102)
B
15.6
86±2
0.09
(98)
B
(g) GY51A
6.8
75±3
0.41
(95)
C
19.9
79±2
0.29
(99)
C
19.10
85±2
0.06
(100)
B
6.9
78±3
0.39
(100)
C
Domain C + Domain D
(h) MK02M
45.2
72±3
0.55
(100)
D
45.1
79±4
0.39
(101)
C
(i) MK02M
45.7
77±4
0.44
(101)
C
45.8
69±3
0.49
(101)
D
Domain D
(j) GY51A
15.3
70±2
0.88
(102)
15.4
68±2
0.93
(99)
15.5
69±2
0.90
(98)
(k) GY51A
17.7
70±2
1.16
(99)
17.5
71±2
0.49
(102)
17.6
69±2
1.09
(98)
(l) MK02M
45.12
70±3
0.49
(103)
45.13
72±3
0.42
(100)
(m) GY89A
47.10
72±3
0.11
(102)
47.11
270±12
0.67
(100)
47.12
71±3
0.20
(99)
Busetsu granite
3 samples (n=133)
Number
100
60
20
70
80
90
100
206Pb/238U Age (Ma)

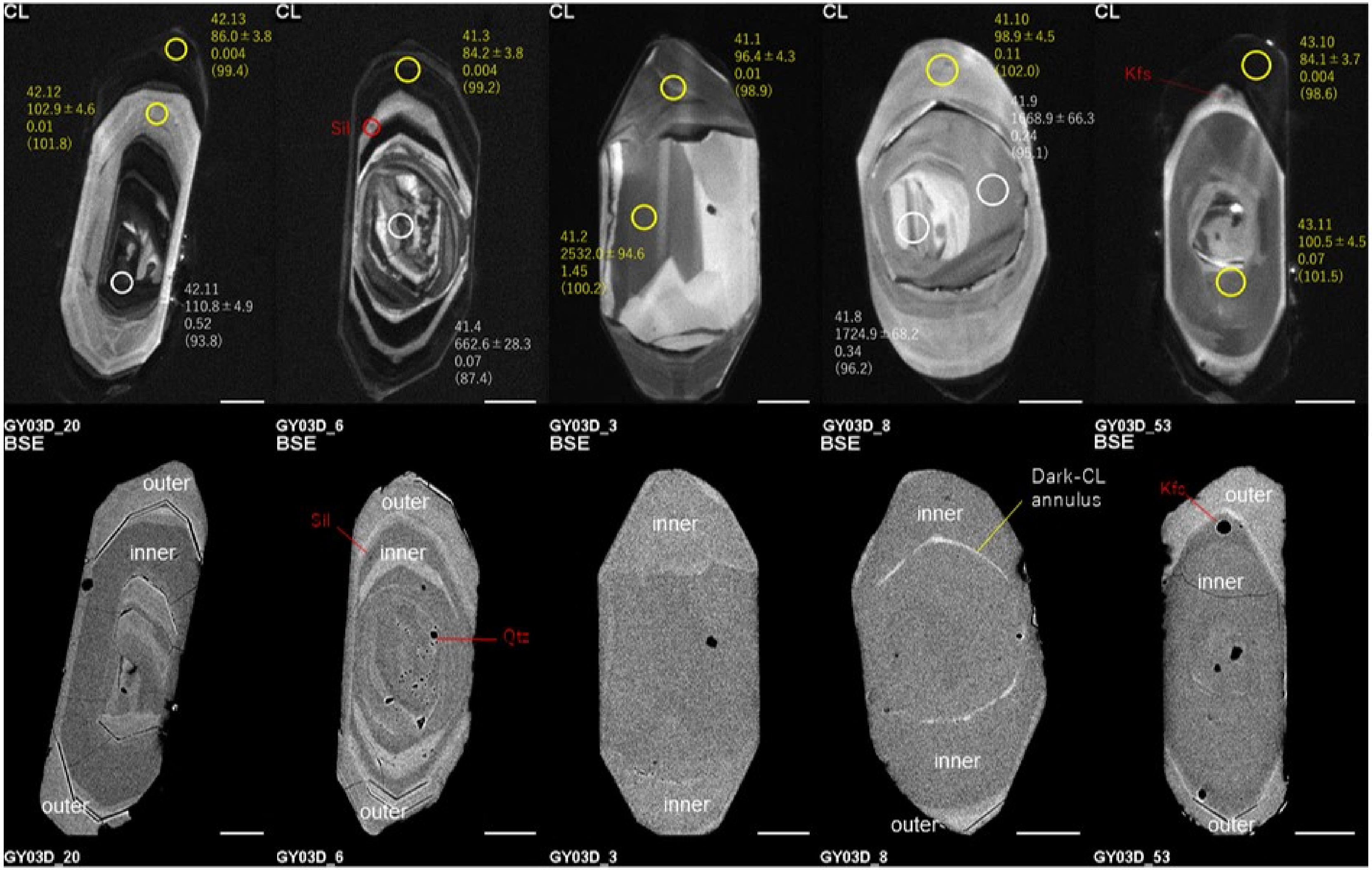
CL
42.13
86.0 ± 3.8
0.004
(99.4)
42.12
102.9 ± 4.6
0.01
(101.8)
42.11
110.8 ± 4.9
0.52
(93.8)
GY03D_20
CL
41.3
84.2 ± 3.8
0.004
(99.2)
Sil
41.4
662.6 ± 28.3
0.07
(87.4)
GY03D_6
CL
41.1
96.4 ± 4.3
0.01
(98.9)
41.2
2532.0 ± 94.6
1.45
(100.2)
GY03D_3
CL
41.10
98.9 ± 4.5
0.11
(102.0)
41.9
1668.9 ± 66.3
0.24
(95.1)
41.8
1724.9 ± 68.2
0.34
(96.2)
GY03D_8
CL
Kfs
43.10
84.1 ± 3.7
0.004
(98.6)
43.11
100.5 ± 4.5
0.07
(101.5)
GY03D_53
BSE
outer
inner
outer
GY03D_20
BSE
Sil
outer
inner
Qtz
outer
GY03D_6
BSE
inner
inner
GY03D_3
BSE
Dark-CL
annulus
inner
inner
outer
GY03D_8
BSE
Kfs
outer
inner
outer
GY03D_53

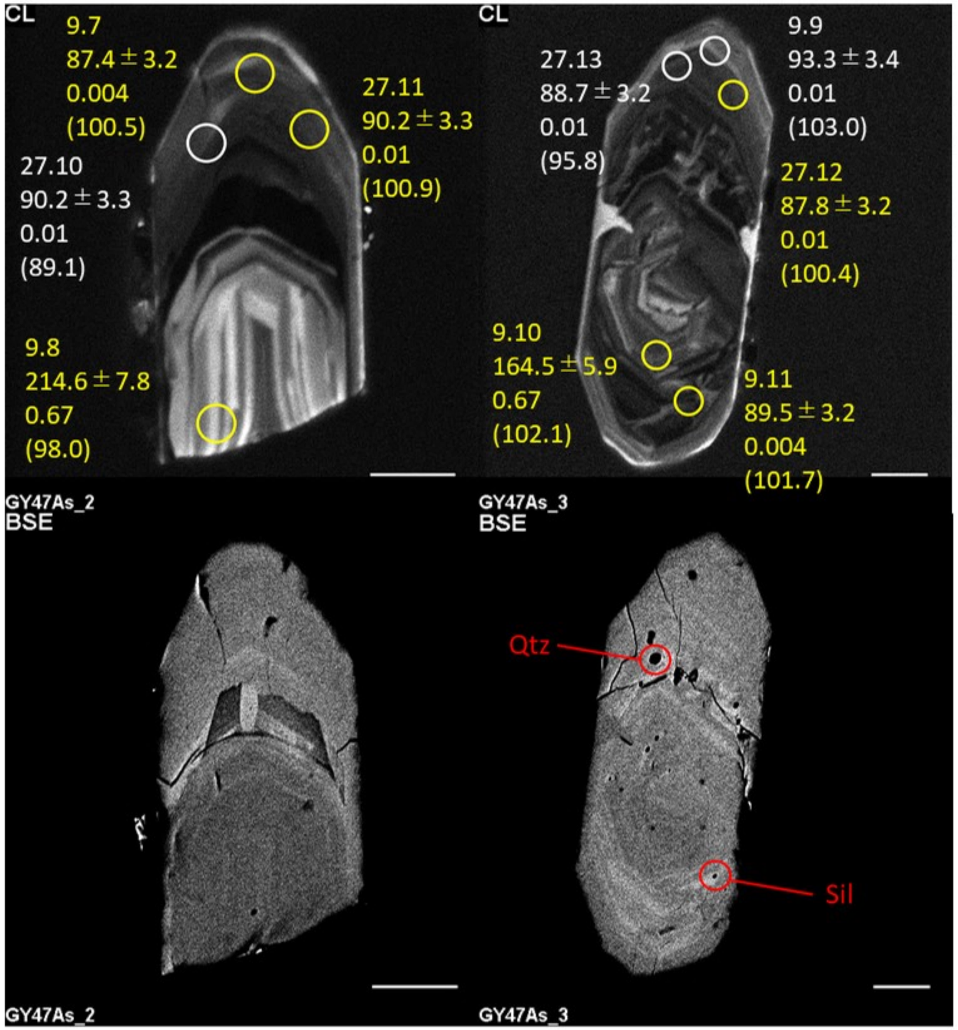
CL
9.7
87.4 ± 3.2
0.004
(100.5)
27.11
90.2 ± 3.3
0.01
(100.9)
27.10
90.2 ± 3.3
0.01
(89.1)
9.8
214.6 ± 7.8
0.67
(98.0)
GY47As_2
CL
27.13
88.7 ± 3.2
0.01
(95.8)
9.9
93.3 ± 3.4
0.01
(103.0)
27.12
87.8 ± 3.2
0.01
(100.4)
9.10
164.5 ± 5.9
0.67
(102.1)
9.11
89.5 ± 3.2
0.004
(101.7)
GY47As_3
BSE
GY47As_2
BSE
Qtz
Sil
GY47As_3

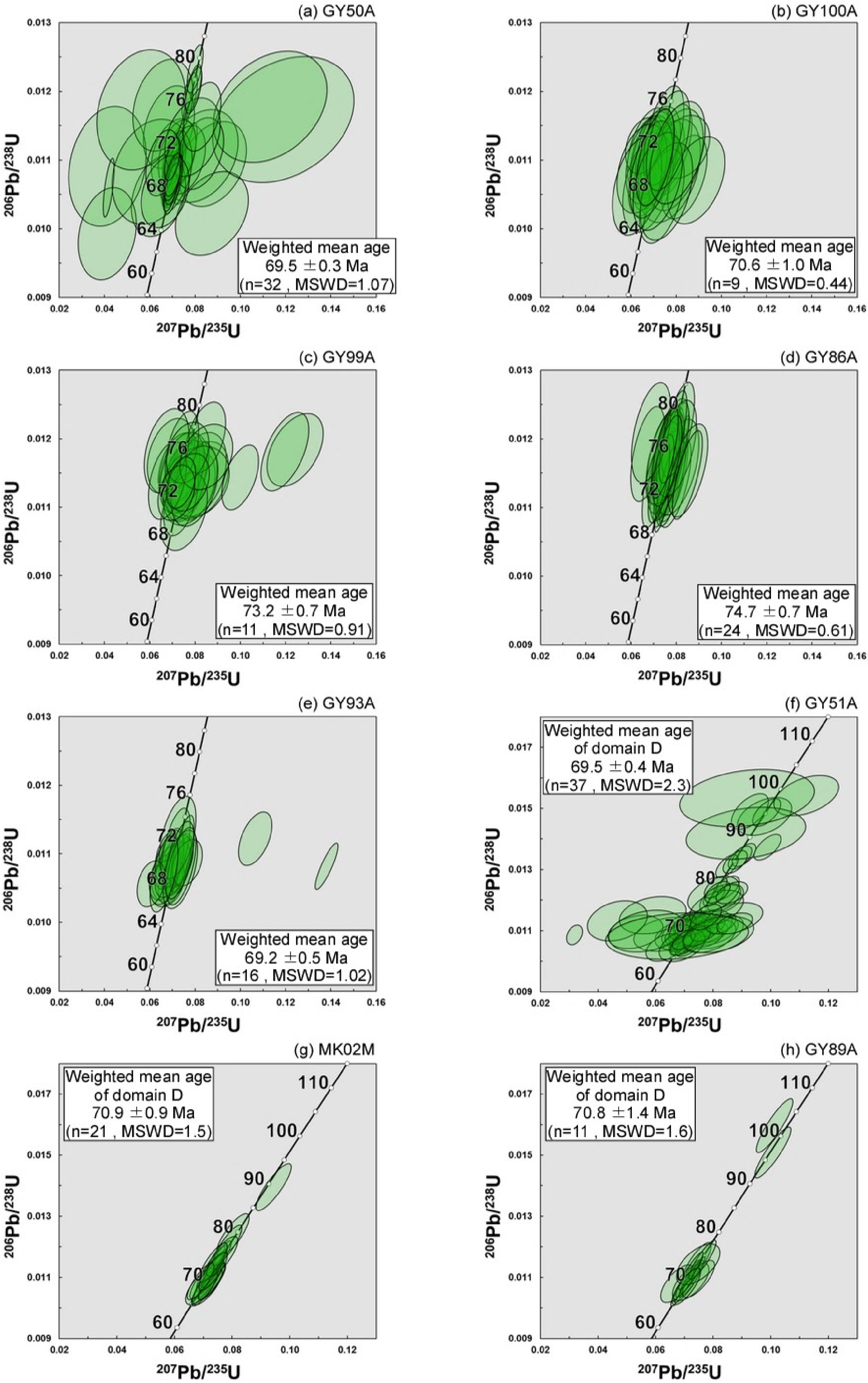
(a) GY50A
Weighted mean age
69.5 ±0.3 Ma
(n=32 , MSWD=1.07)
(b) GY100A
Weighted mean age
70.6 ±1.0 Ma
(n=9 , MSWD=0.44)
(c) GY99A
Weighted mean age
73.2 ±0.7 Ma
(n=11 , MSWD=0.91)
(d) GY86A
Weighted mean age
74.7 ±0.7 Ma
(n=24 , MSWD=0.61)
(e) GY93A
Weighted mean age
69.2 ±0.5 Ma
(n=16 , MSWD=1.02)
(f) GY51A
Weighted mean age
of domain D
69.5 ±0.4 Ma
(n=37 , MSWD=2.3)
(g) MK02M
Weighted mean age
of domain D
70.9 ±0.9 Ma
(n=21 , MSWD=1.5)
(h) GY89A
Weighted mean age
of domain D
70.8 ±1.4 Ma
(n=11 , MSWD=1.6)
206Pb/238U
207Pb/235U

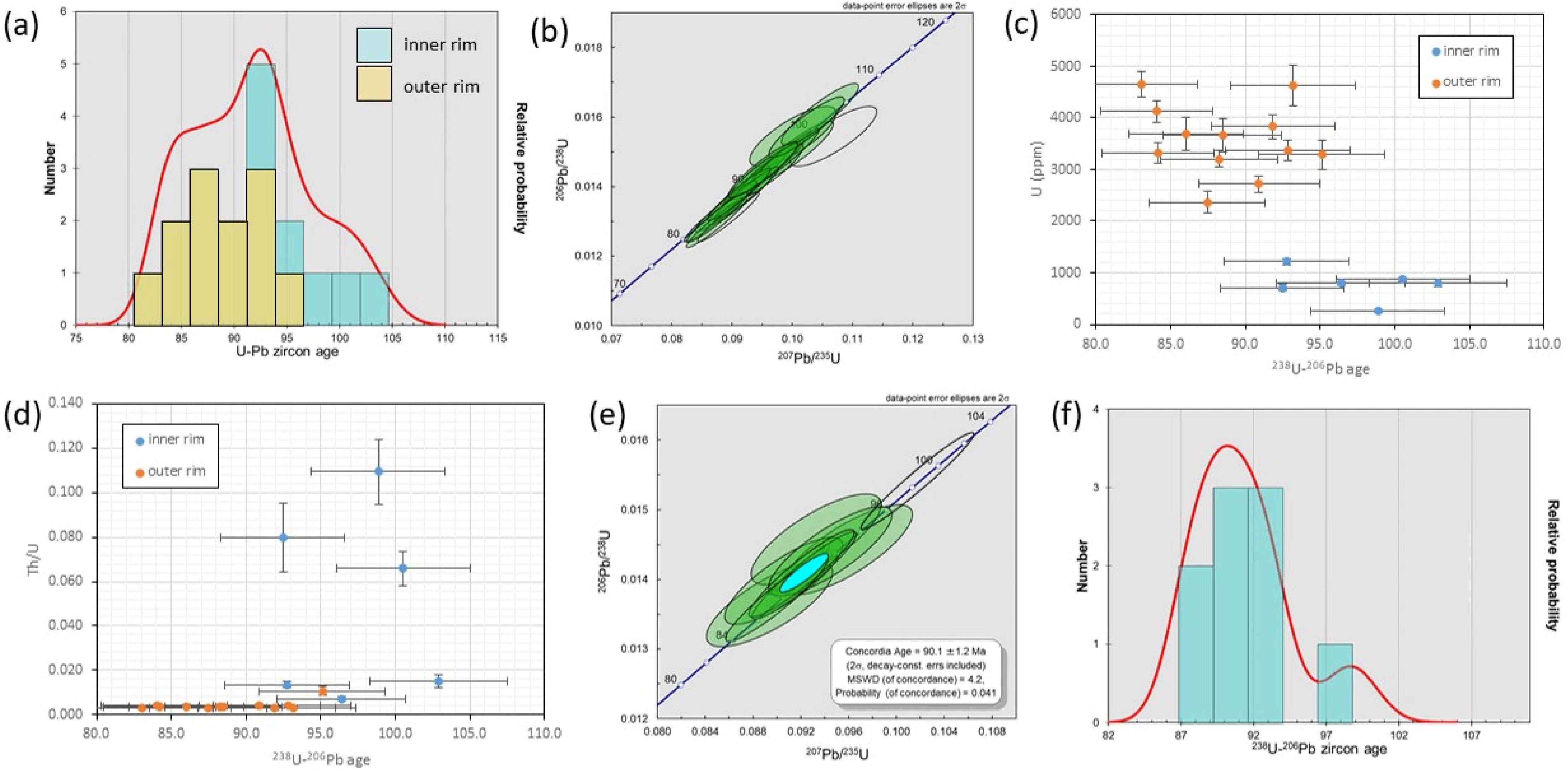

(a)
inner rim
outer rim
Number
Relative probability
U-Pb zircon age
(b)
data-point error ellipses are 2σ
$^{206}Pb/^{238}U$
$^{207}Pb/^{235}U$
(c)
inner rim
outer rim
U (ppm)
^{238}U-^{206}Pb age
(d)
inner rim
outer rim
Th/U
^{238}U-^{206}Pb age
(e)
data-point error ellipses are 2σ
Concordia Age = 90.1 ±1.2 Ma
(2σ, decay-const. errs included)
MSWD (of concordance) = 4.2,
Probability (of concordance) = 0.041
$^{206}Pb/^{238}U$
$^{207}Pb/^{235}U$
(f)
Number
Relative probability
^{238}U-^{206}Pb zircon age

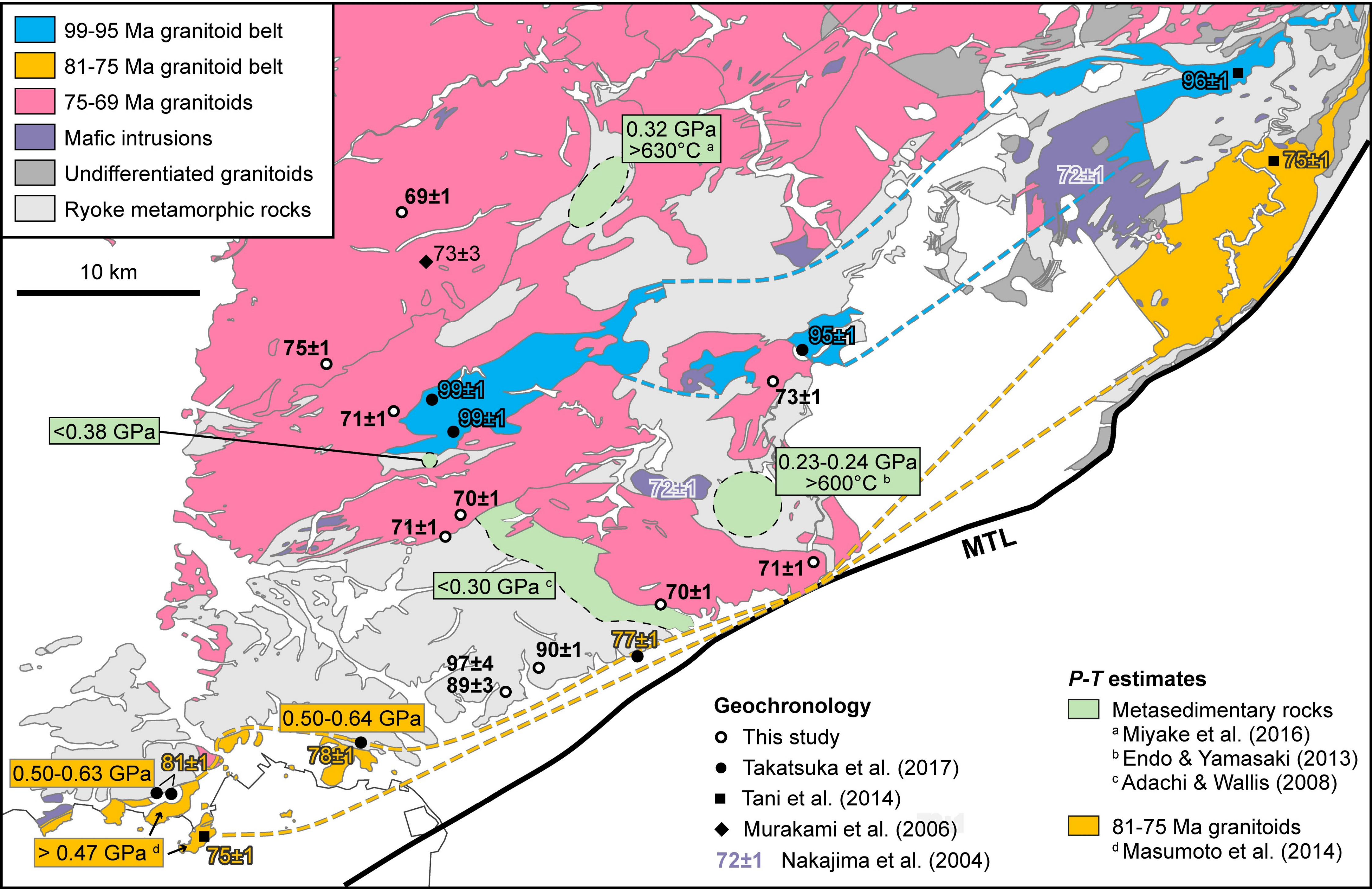

99-95 Ma granitoid belt
81-75 Ma granitoid belt
75-69 Ma granitoids
Mafic intrusions
Undifferentiated granitoids
Ryoke metamorphic rocks
10 km
0.32 GPa >630°C a
69±1
73±3
75±1
99±1
99±1
71±1
<0.38 GPa
96±1
75±1
72±1
95±1
73±1
0.23-0.24 GPa >600°C b
72±1
70±1
71±1
71±1
<0.30 GPa c
70±1
MTL
77±1
90±1
97±4
89±3
0.50-0.64 GPa
78±1
0.50-0.63 GPa
81±1
> 0.47 GPa d
75±1
Geochronology
This study
Takatsuka et al. (2017)
Tani et al. (2014)
Murakami et al. (2006)
72±1 Nakajima et al. (2004)
P-T estimates
Metasedimentary rocks
a Miyake et al. (2016)
b Endo & Yamasaki (2013)
c Adachi & Wallis (2008)
81-75 Ma granitoids
d Masumoto et al. (2014)

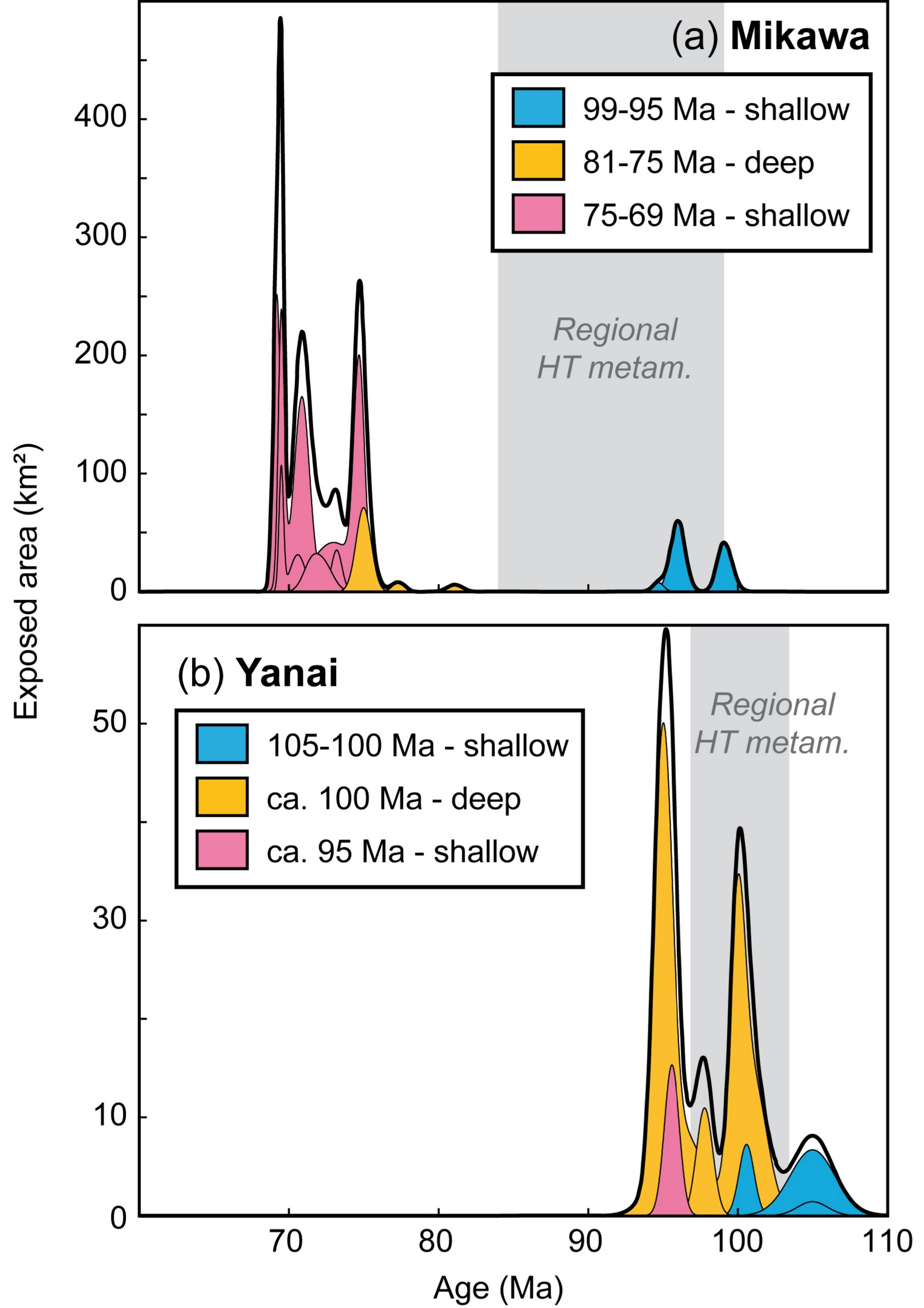
(a) Mikawa
99-95 Ma - shallow
81-75 Ma - deep
75-69 Ma - shallow
Regional HT metam.
(b) Yanai
105-100 Ma - shallow
ca. 100 Ma - deep
ca. 95 Ma - shallow
Regional HT metam.
Exposed area (km²)
Age (Ma)
0
100
200
300
400
10
30
50
70
80
90
100
110

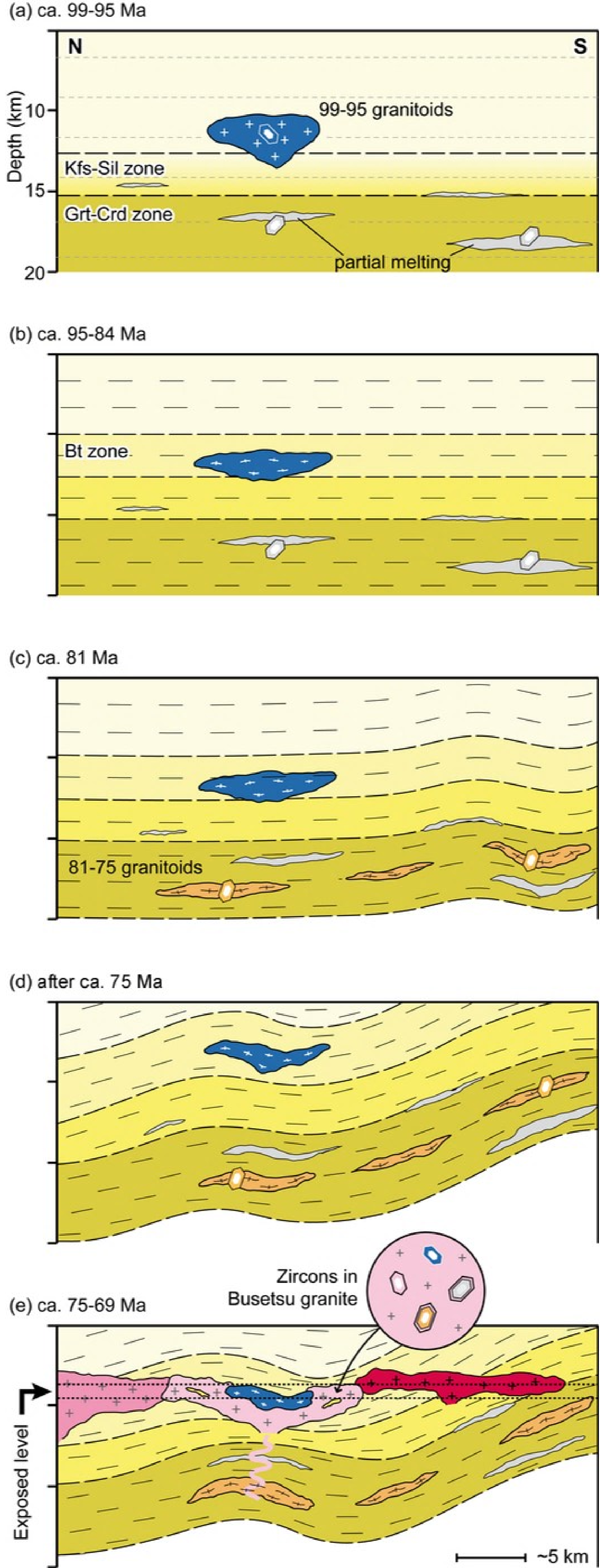
(a) ca. 99-95 Ma
N
S
Depth (km)
10
15
20
99-95 granitoids
Kfs-Sil zone
Grt-Crd zone
partial melting
(b) ca. 95-84 Ma
Bt zone
(c) ca. 81 Ma
81-75 granitoids
(d) after ca. 75 Ma
(e) ca. 75-69 Ma
Zircons in
Busetsu granite
Exposed level
~5 km

Table 1

Summary of published geochronological data for granitoids in the Mikawa area.

Name	Age (Ma)	Method	Mineral	Reference
"Older Ryoke granitoids"				
Kamihara tonalite	94.9±4.9	CHIME	Mnz	Nakai & Suzuki (1996)
Kamihara tonalite	94.5±3.1	CHIME	Mnz	Nakai & Suzuki (1996)
Kamihara tonalite	93.9±2.0	CHIME	Mnz	Morishita et al. (1996)
Kamihara tonalite	97.1±3.7	CHIME	Mnz	Morishita et al. (1996)
Kamihara tonalite	70.7±3.6	K-Ar	Bt	Yamasaki (2013)
Tenryukyo granite[a]	89.7±7.7	CHIME	Mnz	Nakai & Suzuki (1996)
Tenryukyo granite[a]	91.2±3.5	CHIME	Mnz	Nakai & Suzuki (1996)
Tenryukyo granite[b]	92.6±6.0	CHIME	Mnz	Morishita et al. (1996)
Tenryukyo granite[b]	92.2±6.0	CHIME	Mnz	Suzuki & Adachi (1998)
Kiyosaki granodiorite	86.6±3.2	CHIME	Mnz	Morishita et al. (1996)
Kiyosaki granodiorite	87.0±2.6	CHIME	Mnz	Morishita et al. (1996)
Kiyosaki granodiorite	70.0	K-Ar	Bt	Ozima et al. (1967)
Kiyosaki granodiorite	69.5	K-Ar	Bt	Ozima et al. (1967)
"Younger Ryoke granitoids"				
Shinshiro tonalite	86.0±4.7	CHIME	Mnz	Morishita & Suzuki (1995)
Shinshiro tonalite	85.2±3.3	CHIME	Mnz	Morishita & Suzuki (1995)
Shinshiro tonalite	85.5±5.5	CHIME	Mnz	Morishita & Suzuki (1995)
Shinshiro tonalite	73.3±2.9	K-Ar	Hbl	Uchiumi et al. (1990)
Shinshiro tonalite	68.0±2.1	K-Ar	Bt	Uchiumi et al. (1990)
Mitsuhashi granodiorite	84.1±3.1	CHIME	Mnz	Suzuki et al. (1994a)
Mitsuhashi granodiorite	83.8±1.3	CHIME	Mnz	Suzuki et al. (1994b)
Mitsuhashi granodiorite	71.0±3.6	K-Ar	Bt	Yamasaki (2013)
Inagawa granite	81.9±1.4	CHIME	Mnz	Suzuki & Adachi (1998)
Inagawa granite	82.6±1.8	CHIME	Mnz	Suzuki & Adachi (1998)
Inagawa granite	83.5±1.5	CHIME	Mnz	Miyake et al. (2016)
Inagawa granite	82.3±3.6	CHIME	Mnz	Miyake et al. (2016)
Inagawa granite	70.1±3.6	K-Ar	Bt	Yamasaki (2013)
Inagawa granite	66.7±3.4	K-Ar	Bt	Yamasaki (2013)
Busetsu granite	76.3±2.4	CHIME	Mnz	Suzuki et al. (1994b)
Busetsu granite	77.6±3.7	CHIME	Mnz	Suzuki et al. (1994b)
Busetsu granite	78.1±2.0	CHIME	Mnz	Suzuki et al. (1994b)
Busetsu granite	78.5±2.6	CHIME	Mnz	Suzuki et al. (1994b)
Busetsu granite	75.0±5.1	CHIME	Mnz	Suzuki et al. (1994b)
Busetsu granite	78.9±5.3	CHIME	Mnz	Suzuki et al. (1994b)
Busetsu granite	77.2±4.1	CHIME	Mnz	Nakai & Suzuki (2003)
Busetsu granite	75.9±6.1	CHIME	Mnz	Nakai & Suzuki (2003)
Busetsu granite	75.3±4.9	CHIME	Mnz	Nakai & Suzuki (2003)
Busetsu granite	66.0±3.3	K-Ar	Bt	Nakai (1982)
Busetsu granite	71.1±3.6	K-Ar	Bt	Yamasaki (2013)

[a] mapped as "78-75 Ma granite" in Fig. 1.

[b] mapped as "81-75 Ma tonalite" in Fig. 1.

Table 2

Granitoid name & lithology	Sample	Weighted average $^{206}Pb/^{238}U$ age (Ma)	Spot number & MSWD of weighted average	Older zircon domains (Ma)
Shinshiro tonalite				
Hbl-Bt tonalite	GY50A	69.5±0.3	n=32, MSWD=1.07	1880
Hbl-Bt tonalite	GY100A	70.6±1.0	n=9, MSWD=0.44	
Mitsuhashi granodiorite				
Hbl-Bt granodiorite	GY99A	73.2±0.7	n=11, MSWD=0.91	501
Inagawa granite				
Gneissose granite	GY86A	74.7±0.7	n=24, MSWD=0.61	296
Massive granite	GY93A	69.2±0.5	n=16, MSWD=1.02	
Busetsu granite				
Medium-grained granite	GY51A	69.5±0.4	n=37, MSWD=2.3	77-80 / 84-86 / 91-95 / 253 / 1896 / 2272
Fine-grained granite	MK02M	70.9±0.9	n=21, MSWD=1.5	77-79 / 89 / 1960
Mylonitized granite	GY89A	70.8±1.4	n=11, MSWD=1.6	96 / 191 / 270 / 1879-1905
Migmatite and Pegmatite				
Leucosome in a psammitic metatexite migmatite	GY03D	97.0±4.4 (inner rim) 88.5±2.5 (outer rim)	n=6, MSWD=3.8 n=12, MSWD=4.1	133 / 167-170 / 191-195 / 236 / 251 / 281 / 2352
Pegmatite	GY47A	90.1±1.2	n=8, MSWD=4.2	165 / 215 / 1876 / 2190

Table S1. Instrumentation and operational settings for LA-ICP-MS analyses

Kyoto University

Analyzed sample	GY03D, GY47A, GY50A, GY51A, GY86A, GY89A, MK02M
Laser ablation system	
Instrument	NWR193 Excimer ArF (ESI, Portland, USA)
Cell type	Two volume cell
Laser wave length	193 nm
Pulse duration	5 ns
Fluence	2.8 - 5.4 J/cm^2
Repetition rate	4, 5 Hz
Ablation pit size	10 μm
Sampling mode	Single hole drilling
Pre-cleaning	1 shot with 15 μm
Carrier gas	He gas and Ar make-up gas combined outside ablation cell
He gas flow rate	0.60 l/min
Ar make-up gas flow rate	0.86 l/min
Ablation duration	20, 25 seconds
Signal smoothing device	Baffle type (Tunheng and Hirata, 2004)
ICP Mass Spectrometer	
Instrument	Nu PlasmaII HR-MC-ICP-MS (Nu Instruments, Wrexham, U.K.)
RF power	1300 W
Data reduction	Integration of total ion counts per single ablation. Signals obtaind from first few seconds were not used for data reduction, and next signals obtained from 10 seconds were integrated for further calculations. Signal intensity of ^{238}U was not monitored and $^{206}Pb/^{238}U$ is calculated assuming $^{238}U/^{235}U$ = 137.88 (Jaffey et al., 1971).
Detection mode	Multiple collector mode using six ion counters (IC and D) and a faraday collector (H)
Monitored isotopes	^{202}Hg, $^{204}(Hg + Pb)$, ^{206}Pb, ^{207}Pb, ^{208}Pb, ^{232}Th, ^{235}U
Detector	IC4 for ^{202}Hg, IC3 for $^{204}(Hg + Pb)$, D2 for ^{206}Pb, D1 or IC1 for ^{207}Pb, IC0 for ^{208}Pb, IC5 for ^{235}U, and H9 for ^{232}Th
Integration time per peak	10 secconds for ^{202}Hg, $^{204}(Hg + Pb)$, ^{206}Pb, ^{207}Pb, ^{208}Pb, ^{232}Th, ^{235}U
Total integration time per reading	0.4 seconds
Formation rate of Th oxide ($^{232}Th^{16}O^+/^{232}Th^+$)	<0.3%
Data processing	
Gas blank	Gas blank counts (20 seconds) acquired before each single measurement and linearly subtracted with a step forward method
Calibration strategy	91500 zircon was used in correction for Pb/U and Th/U fractionation in all measurements. NIST SRM610 was used for correction of Pb/Pb fractionation. All correction factor for elemental and isotopic fractionation are determined by linear interpolation. GJ-1 (600.39 ± 0.65 Ma, Jackson et al., 2004), Plešovice (337.13 ± 0.37 Ma, Sláma et al., 2008) and OD-3 (32.853±0.016 Ma, Lukács et al., 2015) were used as secondary reference material for validation of accuracy
Normalization values	$^{206}Pb/^{238}U$ = 0.1792, $^{208}Pb/^{232}Th$ = 0.05374, U concentration = 81.2 μg/g, Th concentration = 28.6 μg/g, Pb concentration = 14.8 μg/g (91500, Wiedenbeck et al., 1995), $^{207}Pb/^{206}Pb$ = 0.9096, $^{206}Pb/^{204}Pb$ = 17.045, $^{207}Pb/^{204}Pb$ = 15.504, $^{208}Pb/^{204}Pb$ = 36.964 (NIST SRM 610, Jochum and Brueckner, 2008).
Common-Pb correction	Not made
Uncertainties	Uncertainties for ages and isotope ratios are quoted at 2 SD absolute, propagation is by quadratic addition. Reproducibility of primary reference material, counting statistics of measured isotope and background signal intensity are propagated (Sakata et al., 2014).
Quality control/validation	GJ-1 : Weighted ave. $^{206}Pb/^{238}U$ age = 603.8 ± 5.4 Ma (2 SD, MSWD = 1.03, n = 17, in 17 sessions), $^{207}Pb/^{235}U$ age = 603.1 ± 4.9 Ma (2 SD, MSWD = 0.68, n = 17, in 17 sessions) Plešovice : Weighted ave. $^{206}Pb/^{238}U$ age = 341.7 ± 4.1 Ma (2 SD, MSWD = 0.86, n = 7, in 7 sessions), $^{207}Pb/^{235}U$ age = 342.4 ± 4.4 Ma (2 SD, MSWD = 0.80, n = 7, in 7 sessions) OD-3 : Weighted ave. $^{206}Pb/^{238}U$ age = 32.2 ± 0.5 Ma (2 SD, MSWD = 0.69, n = 10, in 10 sessions), $^{207}Pb/^{235}U$ age = 33.8 ± 1.1 Ma (2 SD, MSWD = 1.7, n = 10, in 10 sessions)

Kyoto University

Analyzed sample	GY50A, GY51A
Laser ablation system	
Instrument	NWR193 Excimer ArF (ESI, Portland, USA)
Cell type	Two volume cell
Laser wave length	193 nm
Pulse duration	5 ns
Fluence	5.3 - 5.5 J/cm^2
Repetition rate	3 Hz
Ablation pit size	20 μm
Sampling mode	Single hole drilling
Pre-cleaning	1 shot with 25 μm
Carrier gas	He gas and Ar make-up gas combined outside ablation cell
He gas flow rate	0.60 l/min
Ar make-up gas flow rate	0.86 l/min
Ablation duration	33 seconds
Signal smoothing device	Baffle type (Tunheng and Hirata, 2004)
ICP Mass Spectrometer	
Instrument	Nu PlasmaII HR-MC-ICP-MS (Nu Instruments, Wrexham, U.K.)
RF power	1300 W
Data reduction	Integration of total ion counts per single ablation. Signals obtaind from first few seconds were not used for data reduction, and next signals obtained from 22 seconds were integrated for further calculations. Signal intensity of ^{238}U was not monitored and $^{206}Pb/^{238}U$ is calculated assuming $^{238}U/^{235}U$ = 137.88 (Jaffey et al., 1971).
Detection mode	Multiple collector mode using six ion counters (IC and D) and a faraday collector (H)
Monitored isotopes	^{202}Hg, $^{204}(Hg + Pb)$, ^{206}Pb, ^{207}Pb, ^{208}Pb, ^{232}Th, ^{235}U
Detector	IC4 for ^{202}Hg, IC3 for $^{204}(Hg + Pb)$, D2 for ^{206}Pb, IC1 for ^{207}Pb, IC0 for ^{208}Pb, IC5 for ^{235}U, and H9 for ^{232}Th
Integration time per peak	22 secconds for ^{202}Hg, $^{204}(Hg + Pb)$, ^{206}Pb, ^{207}Pb, ^{208}Pb, ^{232}Th, ^{235}U
Total integration time per reading	0.4 seconds
Formation rate of Th oxide ($^{232}Th^{16}O^+/^{232}Th^+$)	<0.3%
Data processing	
Gas blank	Gas blank counts (20 seconds) acquired before each single measurement and linearly subtracted with a step forward method
Calibration strategy	91500 zircon was used in correction for Pb/U and Th/U fractionation in all measurements. NIST SRM610 was used for correction of Pb/Pb fractionation. All correction factor for elemental and isotopic fractionation are determined by linear interpolation. GJ-1 (600.39 ± 0.65 Ma, Jackson et al., 2004) and Plešovice (337.13 ± 0.37 Ma, Sláma et al., 2008) were used as secondary reference material for validation of accuracy
Normalization values	$^{206}Pb/^{238}U$ = 0.1792, $^{208}Pb/^{232}Th$ = 0.05374, U concentration = 81.2 μg/g, Th concentration = 28.6 μg/g, Pb concentration = 14.8 μg/g (91500, Wiedenbeck et al., 1995), $^{207}Pb/^{206}Pb$ = 0.9096, $^{206}Pb/^{204}Pb$ = 17.045, $^{207}Pb/^{204}Pb$ = 15.504, $^{208}Pb/^{204}Pb$ = 36.964 (NIST SRM 610, Jochum and Brueckner, 2008).
Common-Pb correction	Not made
Uncertainties	Uncertainties for ages and isotope ratios are quoted at 2 SD absolute, propagation is by quadratic addition. Reproducibility of primary reference material, counting statistics of measured isotope and background signal intensity are propagated (Sakata et al., 2014).
Quality control/validation	GJ-1 : Weighted ave. $^{206}Pb/^{238}U$ age = 598.6 ± 8.5 Ma (2 SD, MSWD = 2.5, n = 9, in 9 sessions), $^{207}Pb/^{235}U$ age = 599.8 ± 5.5 Ma (2 SD, MSWD = 1.11, n = 9, in 9 sessions) Plešovice : Weighted ave. $^{206}Pb/^{238}U$ age = 342.3 ± 2.7 Ma (2 SD, MSWD = 0.87, n = 9, in 9 sessions), $^{207}Pb/^{235}U$ age = 341.0 ± 3.5 Ma (2 SD, MSWD = 0.37, n = 9, in 9 sessions)

Gakushuin University

Analyzed sample	GY51A, GY93A, GY99A, GY100A
Laser ablation system	
Instrument	NWR213 Nd:YAG laser (ESI, Portland, U.S.A.)
Cell type	Two volume cell
Laser wave length	213 nm
Pulse duration	<5 ns
Fluence	3.5—4.5 J/cm^2
Repetition rate	5 Hz
Ablation pit size	10 or 20 μm
Sampling mode	Single hole drilling
Pre-cleaning	1 shot with 15 or 35 μm
Carrier gas	He gas and Ar make-up gas combined outside ablation cell
He gas flow rate	0.60—0.85 l/min
Ar make-up gas flow rate	1.4—1.5 l/min
Ablation duration	10 s
Signal smoothing device	Baffle type (volume: 120 ml)
ICP Mass Spectrometer	
Instrument	Agilent8800 (Agileent Technology, Santa Clara, California, U.S.A.)
RF power	1310 W
Data reduction	Integration of total ion counts per single ablation. Signals obtaind from first few seconds were not used for data reduction, and next signals obtained from 15 s were integrated for further calculations. Signal intensity of ^{235}U was not monitored and $^{207}Pb/^{235}U$ is calculated assuming $^{238}U/^{235}U$ = 137.88 (Jaffey et al., 1971). Oxide ions of Th and U (ThO^+ and UO^+) were monitored and used for further calculation instead of Th^+ and U^+
Detection mode	Pulse counting mode by an ion counter
Mass scan mode	MS/MS mode
Collision/reaction gas and flow rate	NH_3 (1.9 ml/min) and He (9 ml/min) for reduction of isobaric interference from mercury (Kasapoğlu et al., 2016)
Octapole bias	-1.9 V
Octapole RF	189 V
Energy discrimination	-12.5 V
Monitored mass peak (amu) and permeable mass value for first quadrupole (Q1) and second quadrupole (Q2)	202 (Hg; Q1 = 202; Q2 = 202), 204 (Hg + Pb; Q1 = 204; Q2 = 204), 206 (Pb; Q1 = 206; Q2 = 206), 207 (Pb; Q1 = 207; Q2 = 207), 248 (ThO; Q1 = 248; Q2 = 248), 254 (UO; Q1 = 254; Q2 = 254)
Integration time per mass peak	202 (5 ms), 204 (10 ms), 206 (50 ms), 207 (50 ms), 248 (20 ms), 254 (50 ms)
Total integration time per reading	0.2047 s
Integration time per single ablation	15 s
$^{232}Th^{16}O^+/^{232}Th^+$	46.8
Data processing	
Gas blank	Gas blank counts were obtained for 15 s before each ablation pit and linearly subtracted with a step forward method.
Calibration strategy	91500 zircon was used in correction for Pb/U and Th/U fractionation in all measurements. NIST SRM610 was used for correction of Pb/Pb fractionation. All correction factor for elemental and isotopic fractionation are determined by linear interpolation. GJ-1 (600.39 ± 0.65 Ma, Jackson et al., 2004) and Plešovice (337.13 ± 0.37 Ma, Sláma et al., 2008) were used as secondary reference material for validation of accuracy
Normalization values	$^{206}Pb/^{238}U$ = 0.1792, U concentration = 81.2 μg/g, Th concentration = 28.6 μg/g, Pb concentration = 14.8 μg/g (91500, Wiedenbeck et al., 1995), $^{207}Pb/^{206}Pb$ = 0.9096, $^{206}Pb/^{204}Pb$ = 17.045, and $^{207}Pb/^{204}Pb$ = 15.504 for NIST SRM610 (Jochum and Brueckner, 2008).
Common-Pb correction	Not made
Uncertainties	Uncertainties for ages and isotope ratios are quoted at 2 SD absolute, propagation is by quadratic addition. Reproducibility of primary reference material, counting statistics of measured isotope and background signal intensity are propagated (Sakata et al., 2014).
Quality control/validation	GJ-1 : Weighted ave. $^{206}Pb/^{238}U$ age = 602.1 ± 5.8 Ma (2 SD, MSWD = 0.71, n = 9, in 9 sessions), $^{207}Pb/^{235}U$ age = 605.7 ± 5.9 Ma (2 SD, MSWD = 0.28, n = 9, in 9 sessions) Plešovice : Weighted ave. $^{206}Pb/^{238}U$ age = 338.1 ± 3.3 Ma (2 SD, MSWD = 0.50, n = 9, in 9 sessions), $^{207}Pb/^{235}U$ age = 337.9 ± 3.6 Ma (2 SD, MSWD = 0.40, n = 9, in 9 sessions)

References

Jackson, S. E., Pearson, W. L., Griffin, W. L., Belousova, E. A., 2004. The application of laser ablation-inductively coupled plasma-mass spectrometry to in situ U-Pb zircon geochronology. Chemical Geology 211, 47-69.

Jaffey A. H., Flynn K. F., Glendenin L. E., Bentleyt W. C., Essling A. M., 1971. Precision measurement of half-lives and specific activities of ^{235}U and ^{238}U. Physical Review C 4, 1889-1906.

Jochum, K. P., Brueckner, S. M., 2008. Reference materials in geoanalytical and environmental research - Review for 2006 and 2007. Geostandards and Geoanalytical Research 32, 405-452.

Kasapoğlu, B., Ersoy, Y. E., Uysal, İ., Palmer, M. R., Zack, T., Koralay, E. O., Karlsson, A., 2016. The petrology of Paleogene volcanism in the Central Sakarya, Nallıhan Region: Implications for the initiation and evolution of post-collisional, slab break-off-related magmatic activity. Lithos 246-247, 81-98.

Lukács, R., Harangi, S., Bachmann, O., Guillong, M., Danišík, M., Buret, Y., von Quadt, A., Dunkl, I., Fodor, L., Sliwinski, J., Soós, I., Szepesi, J., 2015. Zircon geochronology and geochemistry to constrain the youngest eruption events and magma evolution of the Mid-Miocene ignimbrite flare-up in the Pannonian Basin, eastern central Europe. Contributions to Mineralogy and Petrology 170.

Pearce, N.J.G., Perkins, W.T., Westgate, J.A., Gorton, M.P., Jackson, S.E., Neal, C.R., Chenery, S.P., 1997. A Compilation of New and Published Major and Trace Element Data for NIST SRM 610 and NIST SRM 612 Glass Reference Materials. Geostandards and Geoanalytical Research 21, 115-144.

Sakata, S., Hattori, K., Iwano, H., Yokoyama, T.D., Danhara, T., Hirata, T., 2014. Determination of U-Pb Ages for Young Zircons using Laser Ablation-ICP-Mass Spectrometry Coupled with an Ion Detection Attenuator Device. Geostandards and Geoanalytical Research 38, 409-420.

Sláma, J., Košler, J., Condon, D. J., Crowley, J. L., Gerdes, A., Hanchar, J. M., Horstwood, M. S. A., Morris, G. A., Nasdala, L., Norberg, N., Schaltegger, U., Schoene, B., Tubrett, M. N., Whitehouse, M. J., 2008. Plešovice zircon - A new natural reference material for U-Pb and Hf isotopic microanalysis. Chemical Geology 249, 1-35.

Tunheng, A., Hirata, T., 2004. Development of signal smoothing device for precise elemental analysis using laser ablation-ICP-mass spectrometry. Journal of Analytical Atomic Spectrometry 19, 932-934.

Wiedenbeck, M., Alle, P., Corfu, F., Griffin, W. L., Meier, M., Oberli, F., van Quadt, A., Roddick, J. C., Spiegel, W., 1995. Three natural zircon standards for U-Th-Pb, Lu-Hf, trace element and REE analyses. Geostandards Newsletter 19, 1-23.

Table S2. Results of LA-ICP-MS U-Pb zircon dating

GY50A (Shinshiro tonalite)
Sequences: 1, 2, 12, 13, 14

Spot no.	Grain no.	Position	U (ppm)	±	Th (ppm)	±	Th/U	±	Isotope ratios $^{207}Pb/^{235}U$	±	$^{206}Pb/^{238}U$	±	ρ	$^{207}Pb/^{206}Pb$	±	Age (Ma) $^{206}Pb/^{238}U$	±	$^{207}Pb/^{235}U$	±	% Conc.	Remarks
1.1	4	rim	50	9	23	9	0.46	0.20	0.0639	0.0099	0.0105	0.0005	0.30	0.0442	0.0065	67.2	3.1	62.9	9.5	106.8	
1.2	44	rim	15	3	5	2	0.37	0.16	0.0413	0.0140	0.0109	0.0007	0.19	0.0275	0.0091	70.0	4.6	41.1	13.8	170.2	
1.3	45	core	26	5	20	8	0.75	0.32	0.0412	0.0105	0.0099	0.0005	0.22	0.0301	0.0075	63.7	3.5	41.0	10.3	155.3	
1.4	12	rim	21	4	17	6	0.81	0.34	0.0611	0.0145	0.0108	0.0006	0.24	0.0409	0.0094	69.5	4.0	60.2	14.0	115.4	
1.5	12	rim	42	8	28	10	0.66	0.28	0.0658	0.0108	0.0118	0.0005	0.28	0.0404	0.0064	75.6	3.5	64.7	10.3	116.9	
1.6	57	core	46	9	38	14	0.83	0.35	0.0877	0.0123	0.0109	0.0005	0.33	0.0581	0.0077	70.2	3.2	85.4	11.6	82.2	
1.7	57	rim	34	6	16	6	0.47	0.20	0.0824	0.0136	0.0111	0.0006	0.30	0.0540	0.0085	70.9	3.5	80.4	12.9	88.2	
1.8	59	rim	40	7	19	7	0.47	0.20	0.0875	0.0132	0.0102	0.0005	0.32	0.0620	0.0088	65.6	3.2	85.1	12.4	77.0	
1.9	19	rim	14	3	6	2	0.45	0.19	0.1190	0.0255	0.0116	0.0008	0.30	0.0745	0.0152	74.3	4.8	114.2	23.4	65.1	
1.10	19	rim	21	4	6	2	0.30	0.13	0.1132	0.0205	0.0118	0.0007	0.31	0.0698	0.0120	75.5	4.2	108.9	18.8	69.3	
1.11	65	rim	63	12	28	11	0.45	0.19	0.0684	0.0092	0.0115	0.0005	0.32	0.0432	0.0055	73.6	3.1	67.2	8.8	109.5	
2.2	67	core	484	17	34	2	0.07	0.01	5.1980	0.1938	0.3279	0.0102	0.84	0.1150	0.0023	1828.0	49.9	1852.3	32.3	98.7	
2.3	25	rim	14	1	3	0	0.21	0.02	0.0562	0.0160	0.0117	0.0007	0.21	0.0347	0.0097	75.2	4.6	55.5	15.5	135.4	
2.4	25	rim	79	3	32	2	0.41	0.03	0.0705	0.0081	0.0111	0.0004	0.34	0.0462	0.0050	71.0	2.7	69.2	7.7	102.6	
2.5	70	core	83	3	43	3	0.52	0.04	0.0821	0.0087	0.0111	0.0004	0.36	0.0536	0.0053	71.1	2.7	80.1	8.2	88.8	
2.6	70	core	121	4	88	6	0.72	0.06	0.0721	0.0068	0.0111	0.0004	0.38	0.0471	0.0041	71.1	2.6	70.7	6.5	100.6	
2.7	28	core	57	2	29	2	0.52	0.04	0.0789	0.0101	0.0113	0.0005	0.32	0.0505	0.0061	72.7	3.0	77.1	9.5	94.3	
2.8	31	core	148	5	97	7	0.65	0.05	0.0831	0.0068	0.0116	0.0004	0.43	0.0518	0.0039	74.6	2.6	81.0	6.4	92.0	
2.9	31	rim	104	4	37	3	0.35	0.03	0.0755	0.0075	0.0110	0.0004	0.37	0.0497	0.0046	70.6	2.6	73.9	7.1	95.5	
2.10	34	core	64	2	29	2	0.46	0.04	0.0669	0.0087	0.0105	0.0004	0.31	0.0460	0.0057	67.6	2.7	65.7	8.3	102.9	
2.11	34	rim	140	5	71	5	0.51	0.04	0.0657	0.0061	0.0110	0.0004	0.39	0.0434	0.0037	70.3	2.5	64.6	5.8	108.8	
12.1	4	rim	88	7	33	5	0.37	0.06	0.0725	0.0031	0.0110	0.0003	0.54	0.0477	0.0017	70.7	1.6	71.1	3.0	99.5	
12.2	4	rim	187	14	115	18	0.62	0.11	0.0720	0.0028	0.0110	0.0003	0.59	0.0473	0.0015	70.8	1.6	70.6	2.7	100.2	
12.3	12	rim	144	11	68	11	0.47	0.08	0.0692	0.0028	0.0107	0.0002	0.57	0.0470	0.0016	68.4	1.6	67.9	2.7	100.7	
12.4	12	core	106	8	69	11	0.65	0.11	0.0742	0.0031	0.0107	0.0002	0.56	0.0505	0.0018	68.4	1.6	72.7	3.0	94.1	
12.5	12	rim	134	10	52	8	0.39	0.07	0.0702	0.0029	0.0107	0.0002	0.57	0.0475	0.0016	68.7	1.6	68.9	2.7	99.7	
12.6	57	rim	192	15	92	14	0.48	0.08	0.0712	0.0028	0.0109	0.0003	0.59	0.0475	0.0015	69.6	1.6	69.8	2.7	99.7	
12.7	57	core	108	8	40	6	0.37	0.06	0.0702	0.0030	0.0109	0.0003	0.55	0.0466	0.0016	70.0	1.6	68.9	2.8	101.6	
12.8	16	rim	1218	94	354	55	0.29	0.05	0.0801	0.0029	0.0123	0.0003	0.64	0.0471	0.0013	79.0	1.8	78.2	2.7	101.0	
12.9	16	core	613	47	527	81	0.86	0.15	0.0777	0.0028	0.0119	0.0003	0.63	0.0472	0.0013	76.5	1.7	76.0	2.7	100.7	
12.10	62	rim	1154	89	474	73	0.41	0.07	0.0795	0.0029	0.0121	0.0003	0.64	0.0478	0.0013	77.3	1.8	77.6	2.7	99.5	
12.11	62	core	381	29	212	33	0.56	0.10	0.0794	0.0030	0.0120	0.0003	0.62	0.0479	0.0014	77.0	1.8	77.6	2.8	99.2	
12.12	65	rim	98	8	33	5	0.33	0.06	0.0707	0.0030	0.0110	0.0003	0.55	0.0468	0.0017	70.3	1.6	69.4	2.9	101.3	
13.1	67	core	348	24	20	3	0.06	0.01	4.9788	0.2123	0.3107	0.0102	0.77	0.1162	0.0032	1744.2	50.5	1815.7	36.7	96.1	
13.2	67	core	557	39	49	7	0.09	0.01	4.7862	0.2041	0.2958	0.0097	0.77	0.1173	0.0032	1670.6	48.6	1782.5	36.5	93.7	
13.3	24	rim	219	15	132	18	0.60	0.09	0.0703	0.0032	0.0107	0.0004	0.73	0.0477	0.0015	68.5	2.3	69.0	3.0	99.4	
13.4	24	rim	152	11	63	9	0.41	0.06	0.0706	0.0033	0.0106	0.0004	0.71	0.0481	0.0016	68.3	2.2	69.2	3.1	98.6	
13.5	24	rim	110	8	43	6	0.39	0.06	0.0719	0.0035	0.0109	0.0004	0.69	0.0477	0.0017	70.0	2.3	70.5	3.3	99.4	
13.6	25	rim	138	10	57	8	0.41	0.06	0.0697	0.0033	0.0108	0.0004	0.70	0.0468	0.0016	69.2	2.3	68.4	3.1	101.1	
13.7	25	rim	113	8	46	6	0.40	0.06	0.0703	0.0034	0.0107	0.0004	0.69	0.0475	0.0017	68.8	2.3	69.0	3.2	99.8	
13.8	25	rim	135	9	53	7	0.39	0.06	0.0712	0.0034	0.0109	0.0004	0.70	0.0474	0.0016	69.9	2.3	69.8	3.2	100.1	
13.9	70	core	178	12	100	14	0.56	0.09	0.0699	0.0032	0.0107	0.0004	0.72	0.0475	0.0015	68.5	2.3	68.6	3.1	99.8	
13.10	70	core	161	11	82	11	0.51	0.08	0.0419	0.0020	0.0106	0.0004	0.68	0.0286	0.0010	68.0	2.2	41.6	2.0	163.2	
13.11	70	core	214	15	154	21	0.72	0.11	0.0767	0.0035	0.0111	0.0004	0.73	0.0501	0.0016	71.2	2.3	75.1	3.3	94.8	
13.12	71	rim	156	11	74	10	0.48	0.07	0.0693	0.0032	0.0108	0.0004	0.71	0.0467	0.0015	69.0	2.3	68.0	3.1	101.4	
13.13	71	core	123	9	77	11	0.63	0.10	0.0717	0.0034	0.0108	0.0004	0.70	0.0482	0.0016	69.2	2.3	70.3	3.2	98.5	
14.1	72	rim	155	15	64	12	0.41	0.09	0.0723	0.0029	0.0109	0.0003	0.58	0.0479	0.0016	70.1	1.6	70.9	2.7	98.9	
14.2	72	core	243	23	170	32	0.70	0.15	0.0701	0.0027	0.0107	0.0002	0.60	0.0477	0.0015	68.3	1.6	68.8	2.6	99.3	
14.3	72	rim	150	14	56	11	0.38	0.08	0.0712	0.0029	0.0107	0.0002	0.58	0.0484	0.0016	68.4	1.6	69.8	2.7	98.0	
14.4	73	rim	210	20	80	15	0.38	0.08	0.0710	0.0028	0.0109	0.0003	0.59	0.0472	0.0015	69.9	1.6	69.7	2.6	100.4	
14.5	73	core	86	8	46	9	0.53	0.11	0.0704	0.0031	0.0108	0.0003	0.54	0.0475	0.0017	68.9	1.6	69.1	2.9	99.7	
14.6	73	rim	77	7	23	4	0.30	0.06	0.0695	0.0031	0.0109	0.0003	0.53	0.0460	0.0017	70.2	1.6	68.2	2.9	102.9	
14.7	29	rim	103	10	39	7	0.38	0.08	0.0682	0.0029	0.0107	0.0003	0.55	0.0462	0.0016	68.8	1.6	67.0	2.8	102.6	
14.8	29	rim	92	9	36	7	0.39	0.08	0.0699	0.0030	0.0107	0.0003	0.54	0.0472	0.0017	68.8	1.6	68.6	2.9	100.3	
14.9	30	core	92	9	61	12	0.67	0.14	0.0698	0.0030	0.0108	0.0003	0.54	0.0469	0.0017	69.1	1.6	68.5	2.9	100.9	
14.10	30	rim	107	10	45	9	0.43	0.09	0.0703	0.0030	0.0108	0.0003	0.55	0.0472	0.0017	69.1	1.6	68.9	2.8	100.3	
14.11	75	rim	154	15	64	12	0.42	0.09	0.0713	0.0029	0.0111	0.0003	0.58	0.0466	0.0015	71.3	1.6	70.0	2.7	101.8	
14.12	75	core	171	16	100	19	0.59	0.12	0.0710	0.0028	0.0109	0.0003	0.58	0.0471	0.0015	70.2	1.6	69.7	2.7	100.7	
14.13	75	rim	115	11	48	9	0.42	0.09	0.0700	0.0029	0.0110	0.0003	0.56	0.0461	0.0016	70.6	1.6	68.7	2.8	102.8	
Rejected spots																					**Remarks**
2.1	67	rim	450	16	128	9	0.28	0.02	0.0996	0.0053	0.0127	0.0004	0.61	0.0567	0.0024	81.7	2.6	96.4	4.9	84.7	irregular signal
12.13	67	rim	492	38	68	11	0.14	0.02	1.6178	0.0575	0.1065	0.0024	0.64	0.1102	0.0030	652.5	14.2	977.1	22.6	66.8	irregular signal

GY100A (Shinshiro tonalite)
Sequences: 71, 72, 73

Spot no.	Grain no.	Position	U (ppm)	±	Th (ppm)	±	Th/U	±	Isotope ratios $^{207}Pb/^{235}U$	±	$^{206}Pb/^{238}U$	±	ρ	$^{207}Pb/^{206}Pb$	±	Age (Ma) $^{206}Pb/^{238}U$	±	$^{207}Pb/^{235}U$	±	% Conc.	Remarks
71.7	78	core	220	23	169	35	0.77	0.18	0.0734	0.0061	0.0110	0.0003	0.34	0.0482	0.0038	70.8	2.0	71.9	5.8	98.4	
71.9	35	core	333	35	285	59	0.86	0.20	0.0694	0.0049	0.0111	0.0003	0.38	0.0454	0.0030	71.0	1.9	68.1	4.6	104.3	
71.10	35	rim	174	18	45	9	0.26	0.06	0.0658	0.0067	0.0112	0.0003	0.29	0.0426	0.0041	71.9	2.1	64.7	6.4	111.0	
71.11	33	core	287	30	141	29	0.49	0.11	0.0762	0.0055	0.0108	0.0003	0.38	0.0510	0.0034	69.5	1.9	74.6	5.2	93.2	
71.12	33	core	340	35	148	31	0.44	0.10	0.0774	0.0051	0.0112	0.0003	0.40	0.0501	0.0030	71.9	1.9	75.7	4.8	95.0	
71.13	33	rim	112	12	44	9	0.40	0.09	0.0833	0.0094	0.0112	0.0004	0.30	0.0540	0.0058	71.8	2.4	81.3	8.8	88.3	
72.1	74	rim	162	11	76	11	0.47	0.07	0.0837	0.0082	0.0108	0.0005	0.47	0.0564	0.0049	69.0	3.2	81.6	7.7	84.5	
72.2	74	rim	133	9	57	8	0.42	0.07	0.0684	0.0082	0.0111	0.0005	0.39	0.0446	0.0049	71.3	3.3	67.2	7.8	106.2	
72.3	73	rim	254	18	63	9	0.25	0.04	0.0684	0.0060	0.0109	0.0005	0.50	0.0457	0.0035	69.6	3.1	67.2	5.7	103.6	
72.4	73	core	157	11	66	9	0.42	0.07	0.0713	0.0077	0.0110	0.0005	0.43	0.0472	0.0046	70.2	3.2	70.0	7.3	100.4	
72.5	73	core	110	8	57	8	0.51	0.08	0.0889	0.0104	0.0107	0.0005	0.42	0.0603	0.0064	68.7	3.3	86.5	9.7	79.3	
72.6	71	rim	150	10	89	12	0.59	0.09	0.0693	0.0078	0.0111	0.0005	0.42	0.0454	0.0046	71.0	3.3	68.0	7.4	104.4	
72.7	71	core	125	9	50	7	0.40	0.06	0.0679	0.0083	0.0110	0.0005	0.39	0.0447	0.0051	70.6	3.3	66.7	7.9	105.8	
72.8	31	core	209	14	149	21	0.71	0.11	0.0718	0.0068	0.0109	0.0005	0.48	0.0478	0.0039	69.8	3.1	70.4	6.4	99.2	
72.9	31	rim	181	13	75	10	0.42	0.06	0.0675	0.0070	0.0108	0.0005	0.44	0.0454	0.0042	69.2	3.2	66.3	6.7	104.3	
72.10	29	rim	247	17	108	15	0.44	0.07	0.0673	0.0061	0.0110	0.0005	0.49	0.0442	0.0035	70.8	3.1	66.1	5.8	107.0	
72.11	29	core	260	18	155	21	0.60	0.09	0.0789	0.0066	0.0112	0.0005	0.53	0.0510	0.0036	71.9	3.2	77.1	6.2	93.2	
72.12	29	rim	108	8	26	4	0.24	0.04	0.0650	0.0090	0.0109	0.0005	0.35	0.0433	0.0056	69.7	3.4	63.9	8.6	109.1	
72.13	68	rim	146	10	88	12	0.60	0.09	0.0721	0.0081	0.0111	0.0005	0.42	0.0469	0.0048	71.4	3.3	70.7	7.7	101.1	
73.1	28	rim	156	8	49	5	0.31	0.03	0.0737	0.0081	0.0105	0.0006	0.49	0.0510	0.0049	67.2	3.6	72.2	7.6	93.0	
73.2	28	core	88	4	41	4	0.46	0.05	0.0773	0.0111	0.0108	0.0006	0.40	0.0517	0.0068	69.5	3.9	75.6	10.4	92.0	
73.3	27	core	114	6	72	7	0.63	0.07	0.0675	0.0091	0.0107	0.0006	0.41	0.0459	0.0057	68.4	3.7	66.4	8.7	103.1	
73.4	27	core	110	6	56	6	0.50	0.06	0.0798	0.0100	0.0110	0.0006	0.44	0.0526	0.0059	70.6	3.9	78.0	9.4	90.5	
73.5	27	rim	206	10	97	10	0.47	0.05	0.0745	0.0072	0.0114	0.0006	0.54	0.0476	0.0039	72.8	3.8	73.0	6.8	99.8	
73.6	24	core	110	6	70	7	0.63	0.07	0.0628	0.0089	0.0106	0.0006	0.39	0.0428	0.0056	68.1	3.7	61.8	8.5	110.3	
73.7	24	core	115	6	71	7	0.62	0.07	0.0757	0.0095	0.0105	0.0006	0.44	0.0521	0.0058	67.6	3.7	74.1	8.9	91.3	
73.8	24	rim	154	8	54	5	0.35	0.04	0.0691	0.0077	0.0109	0.0006	0.48	0.0461	0.0045	69.7	3.7	67.8	7.3	102.7	
73.9	64	rim	125	6	36	4	0.29	0.03	0.0718	0.0089	0.0107	0.0006	0.44	0.0487	0.0054	68.5	3.7	70.4	8.4	97.4	
73.10	64	core	173	9	79	8	0.46	0.05	0.0765	0.0079	0.0113	0.0006	0.51	0.0491	0.0044	72.3	3.8	74.8	7.5	96.7	
73.11	64	rim	110	6	33	3	0.30	0.03	0.0806	0.0100	0.0111	0.0006	0.44	0.0526	0.0058	71.2	3.9	78.7	9.4	90.5	
73.12	62	rim	248	12	62	6	0.25	0.03	0.0710	0.0065	0.0111	0.0006	0.57	0.0466	0.0035	70.9	3.6	69.6	6.1	101.8	
73.13	62	core	222	11	171	17	0.77	0.09	0.0709	0.0068	0.0110	0.0006	0.54	0.0466	0.0038	70.8	3.7	69.5	6.5	101.8	
Rejected spots																					**Remarks**
71.8	78	core	115	12	62	13	0.54	0.13	0.1585	0.0131	0.0130	0.0004	0.39	0.0887	0.0067	83.0	2.6	149.4	11.5	55.6	irregular signal

GY99A (Mitsuhashi granodiorite)
Sequences: 69, 70, 71

Spot no.	Grain no.	Position	U (ppm)	±	Th (ppm)	±	Th/U	±	Isotope ratios $^{207}Pb/^{235}U$	±	$^{206}Pb/^{238}U$	±	ρ	$^{207}Pb/^{206}Pb$	±	Age (Ma) $^{206}Pb/^{238}U$	±	$^{207}Pb/^{235}U$	±	% Conc.	Remarks
69.1	41	core	202	27	155	41	0.77	0.23	0.0807	0.0068	0.0113	0.0004	0.42	0.0518	0.0040	72.4	2.5	78.8	6.4	92.0	
69.2	41	rim	114	15	64	17	0.56	0.17	0.0694	0.0086	0.0117	0.0005	0.31	0.0429	0.0050	75.3	2.9	68.1	8.2	110.5	
69.3	38	rim	147	20	83	22	0.57	0.17	0.1243	0.0102	0.0118	0.0004	0.45	0.0761	0.0056	75.9	2.8	119.0	9.2	63.8	
69.4	38	core	291	39	197	53	0.68	0.20	0.0999	0.0067	0.0114	0.0004	0.51	0.0634	0.0036	73.3	2.5	96.7	6.2	75.8	
69.5	37	core	186	25	87	23	0.47	0.14	0.0741	0.0068	0.0114	0.0004	0.39	0.0469	0.0039	73.3	2.6	72.6	6.4	101.1	
69.6	37	rim	150	20	59	16	0.39	0.12	0.0730	0.0075	0.0116	0.0004	0.36	0.0458	0.0044	74.2	2.7	71.5	7.1	103.7	
69.7	72	core	112	15	34	9	0.31	0.09	0.0750	0.0087	0.0116	0.0004	0.33	0.0471	0.0052	74.0	2.8	73.5	8.3	100.8	
69.9	32	rim	101	14	47	13	0.47	0.14	0.0829	0.0098	0.0114	0.0005	0.33	0.0527	0.0059	73.1	2.9	80.9	9.2	90.4	
69.10	32	core	189	25	79	21	0.42	0.13	0.0761	0.0068	0.0113	0.0004	0.40	0.0489	0.0040	72.3	2.6	74.4	6.5	97.2	
69.11	29	rim	192	26	101	27	0.53	0.16	0.0847	0.0072	0.0120	0.0004	0.42	0.0511	0.0039	77.0	2.7	82.6	6.7	93.3	
69.12	29	core	221	30	183	49	0.83	0.25	0.0756	0.0064	0.0115	0.0004	0.41	0.0477	0.0037	73.7	2.6	74.0	6.0	99.5	
69.13	29	rim	242	32	123	33	0.51	0.15	0.0736	0.0060	0.0115	0.0004	0.42	0.0466	0.0034	73.5	2.5	72.1	5.7	101.8	
70.1	70	rim	143	4	85	5	0.59	0.04	0.0754	0.0080	0.0114	0.0005	0.40	0.0480	0.0047	73.1	3.1	73.8	7.5	99.0	
70.2	70	core	961	27	474	27	0.49	0.03	0.0811	0.0042	0.0114	0.0004	0.72	0.0514	0.0018	73.4	2.7	79.2	3.9	92.6	
70.3	70	rim	106	3	58	4	0.55	0.04	0.0819	0.0097	0.0115	0.0005	0.37	0.0517	0.0057	73.6	3.2	79.9	9.2	92.1	
70.4	69	core	257	7	305	18	1.19	0.08	0.0742	0.0061	0.0118	0.0005	0.48	0.0455	0.0033	75.9	3.0	72.7	5.8	104.4	
70.5	69	rim	102	3	42	3	0.41	0.03	0.0778	0.0098	0.0114	0.0005	0.35	0.0497	0.0058	72.8	3.2	76.1	9.2	95.7	
70.6	68	rim	240	7	147	9	0.61	0.04	0.0738	0.0063	0.0111	0.0004	0.47	0.0481	0.0036	71.4	2.8	72.3	5.9	98.7	
70.7	68	rim	134	4	47	3	0.35	0.02	0.0751	0.0084	0.0109	0.0005	0.38	0.0498	0.0052	70.1	3.0	73.5	7.9	95.4	
70.8	67	rim	137	4	44	3	0.32	0.02	0.0798	0.0085	0.0113	0.0005	0.40	0.0512	0.0050	72.5	3.1	78.0	8.0	93.0	
70.9	67	core	234	7	140	8	0.60	0.04	0.1197	0.0086	0.0118	0.0005	0.55	0.0735	0.0044	75.7	3.0	114.8	7.8	66.0	
70.10	65	rim	140	4	55	3	0.39	0.03	0.0742	0.0081	0.0115	0.0005	0.39	0.0468	0.0047	73.7	3.1	72.7	7.6	101.4	
70.11	65	core	183	5	99	6	0.54	0.04	0.0678	0.0068	0.0114	0.0005	0.41	0.0432	0.0040	73.0	3.0	66.6	6.5	109.6	
70.12	64	core	376	11	259	15	0.69	0.04	0.6410	0.0278	0.0809	0.0030	0.85	0.0575	0.0013	501.3	17.8	502.9	17.2	99.7	
70.13	64	rim	128	4	62	4	0.48	0.03	0.0675	0.0081	0.0118	0.0005	0.35	0.0414	0.0046	75.8	3.2	66.3	7.7	114.3	
71.1	63	rim	72	8	26	5	0.36	0.08	0.0803	0.0121	0.0114	0.0004	0.25	0.0513	0.0075	72.8	2.8	78.4	11.4	92.9	
71.2	63	core	150	16	129	27	0.86	0.20	0.0767	0.0077	0.0118	0.0004	0.30	0.0472	0.0045	75.6	2.3	75.1	7.3	100.7	
71.3	23	core	161	17	125	26	0.78	0.18	0.0772	0.0075	0.0114	0.0003	0.31	0.0492	0.0045	72.9	2.2	75.5	7.0	96.5	
71.4	23	rim	107	11	50	10	0.47	0.11	0.0850	0.0096	0.0117	0.0004	0.30	0.0525	0.0056	75.2	2.5	82.8	9.0	90.8	
71.5	62	core	186	19	105	22	0.56	0.13	0.0718	0.0067	0.0112	0.0003	0.32	0.0465	0.0041	71.9	2.1	70.4	6.3	102.1	
71.6	62	rim	298	31	241	50	0.81	0.19	0.0738	0.0053	0.0114	0.0003	0.37	0.0471	0.0032	72.8	1.9	72.3	5.0	100.8	
Rejected spots																					**Remarks**
69.8	72	rim	92	12	56	15	0.61	0.18	0.2579	0.0199	0.0132	0.0005	0.51	0.1415	0.0094	84.7	3.3	233.0	16.1	36.3	irregular signal

GY86A (Inagawa granite)
Sequences: 33, 34, 35

									Isotope ratios						Age (Ma)				
Spot no.	Grain no.	Position	U (ppm)	±	Th (ppm)	±	Th/U	±	$^{207}Pb/^{235}U$	±	$^{206}Pb/^{238}U$	±	ρ	$^{207}Pb/^{206}Pb$	±	$^{206}Pb/^{238}U$	±	$^{207}Pb/^{235}U$	±	% Conc.
33.1	2	core	448	38	215	37	0.48	0.09	0.0766	0.0043	0.0117	0.0005	0.80	0.0476	0.0016	74.9	3.4	75.0	4.1	99.9
33.2	2	rim	339	29	153	26	0.45	0.09	0.0754	0.0045	0.0114	0.0005	0.77	0.0481	0.0018	72.8	3.3	73.8	4.3	98.6
33.3	2	rim	156	13	97	16	0.62	0.12	0.0767	0.0055	0.0115	0.0005	0.65	0.0484	0.0026	73.7	3.4	75.1	5.2	98.1
33.4	5	rim	188	16	99	17	0.53	0.10	0.0787	0.0053	0.0114	0.0005	0.69	0.0499	0.0024	73.3	3.4	76.9	5.0	95.4
33.5	5	core	195	17	169	29	0.87	0.16	0.0776	0.0052	0.0114	0.0005	0.69	0.0495	0.0024	72.9	3.4	75.9	4.9	96.0
33.6	53	core	868	74	527	89	0.61	0.12	0.0753	0.0039	0.0113	0.0005	0.86	0.0485	0.0013	72.2	3.2	73.7	3.7	97.9
33.7	53	core	63	5	34	6	0.55	0.10	0.0807	0.0077	0.0116	0.0006	0.52	0.0505	0.0041	74.3	3.6	78.8	7.3	94.3
33.8	53	rim	243	21	107	18	0.44	0.08	0.0788	0.0050	0.0115	0.0005	0.73	0.0496	0.0022	73.8	3.4	77.0	4.7	95.9
33.9	54	rim	141	12	104	18	0.74	0.14	0.0753	0.0056	0.0115	0.0005	0.63	0.0476	0.0027	73.5	3.4	73.7	5.3	99.7
33.10	54	rim	81	7	46	8	0.57	0.11	0.0675	0.0062	0.0118	0.0006	0.52	0.0415	0.0032	75.5	3.6	66.3	5.9	113.9
33.11	55	core	556	47	386	65	0.69	0.13	0.3419	0.0167	0.0470	0.0021	0.92	0.0528	0.0010	295.8	13.0	298.6	12.7	99.1
33.12	55	rim	233	20	173	29	0.74	0.14	0.0751	0.0048	0.0118	0.0005	0.71	0.0460	0.0021	75.9	3.5	73.6	4.6	103.1
33.13	55	rim	234	20	123	21	0.52	0.10	0.0763	0.0049	0.0115	0.0005	0.72	0.0482	0.0022	73.7	3.4	74.7	4.6	98.7
34.1	8	rim	128	7	74	8	0.58	0.07	0.0809	0.0059	0.0121	0.0006	0.64	0.0483	0.0027	77.8	3.6	79.0	5.6	98.5
34.2	8	core	1402	77	630	69	0.45	0.06	0.0811	0.0040	0.0117	0.0005	0.92	0.0502	0.0010	75.0	3.4	79.2	3.7	94.8
34.3	8	rim	116	6	69	8	0.60	0.07	0.0783	0.0060	0.0119	0.0006	0.62	0.0477	0.0029	76.3	3.6	76.5	5.7	99.7
34.4	12	rim	517	28	258	28	0.50	0.06	0.0774	0.0042	0.0117	0.0005	0.83	0.0479	0.0014	75.2	3.4	75.7	4.0	99.2
34.5	14	rim	70	4	37	4	0.54	0.07	0.0801	0.0072	0.0119	0.0006	0.54	0.0490	0.0037	76.0	3.7	78.3	6.8	97.1
34.6	14	core	82	4	57	6	0.70	0.09	0.0853	0.0072	0.0115	0.0006	0.57	0.0536	0.0037	74.0	3.5	83.1	6.7	89.0
34.7	14	rim	162	9	119	13	0.74	0.09	0.0768	0.0053	0.0116	0.0005	0.67	0.0481	0.0025	74.2	3.4	75.1	5.0	98.7
34.8	20	rim	169	9	14	2	0.09	0.01	0.0711	0.0050	0.0114	0.0005	0.66	0.0454	0.0024	72.8	3.4	69.7	4.7	104.5
34.9	20	core	118	6	95	10	0.81	0.10	0.0744	0.0057	0.0116	0.0005	0.61	0.0466	0.0028	74.2	3.5	72.9	5.4	101.9
34.10	20	rim	232	13	131	14	0.56	0.07	0.0733	0.0047	0.0114	0.0005	0.72	0.0465	0.0021	73.2	3.4	71.8	4.4	101.9
34.11	21	rim	205	11	18	2	0.09	0.01	0.0849	0.0054	0.0115	0.0005	0.72	0.0537	0.0024	73.6	3.4	82.8	5.1	88.9
34.12	21	core	268	15	229	25	0.86	0.11	0.0771	0.0047	0.0115	0.0005	0.75	0.0485	0.0020	73.9	3.4	75.4	4.5	98.0
34.13	23	rim	177	10	104	11	0.59	0.07	0.0792	0.0053	0.0119	0.0005	0.69	0.0484	0.0024	76.0	3.5	77.4	5.0	98.2
35.1	74b	rim	58	4	30	5	0.53	0.09	0.0690	0.0071	0.0121	0.0006	0.48	0.0414	0.0038	77.5	3.8	67.7	6.8	114.4
35.2	74b	core	201	16	183	28	0.91	0.16	0.0762	0.0050	0.0116	0.0005	0.70	0.0475	0.0022	74.6	3.4	74.6	4.8	100.0
35.3	75	rim	122	9	65	10	0.53	0.09	0.0764	0.0058	0.0118	0.0006	0.62	0.0470	0.0028	75.7	3.5	74.8	5.5	101.2
35.4	75	core	143	11	76	12	0.53	0.09	0.0756	0.0055	0.0117	0.0005	0.64	0.0467	0.0026	75.2	3.5	74.0	5.2	101.7
35.5	75	rim	102	8	54	8	0.53	0.09	0.0740	0.0061	0.0117	0.0006	0.58	0.0458	0.0030	75.2	3.5	72.5	5.7	103.7
35.6	78	rim	236	18	125	19	0.53	0.09	0.0786	0.0050	0.0120	0.0006	0.73	0.0474	0.0020	77.1	3.5	76.8	4.7	100.4
35.7	78	core	137	11	60	9	0.44	0.08	0.0794	0.0058	0.0114	0.0005	0.64	0.0507	0.0028	72.8	3.4	77.6	5.5	93.9
35.8	79	rim	204	16	75	12	0.37	0.06	0.0759	0.0050	0.0118	0.0005	0.70	0.0466	0.0022	75.7	3.5	74.3	4.7	101.9
35.9	79	core	5334	414	1414	220	0.27	0.05	0.0775	0.0036	0.0115	0.0005	0.96	0.0488	0.0007	73.8	3.3	75.8	3.4	97.4
35.10	79	core	455	35	211	33	0.46	0.08	0.0764	0.0043	0.0117	0.0005	0.81	0.0472	0.0015	75.3	3.4	74.7	4.0	100.7
35.11	31	core	77	6	58	9	0.76	0.13	0.0752	0.0068	0.0117	0.0006	0.54	0.0465	0.0035	75.2	3.6	73.6	6.4	102.2
35.12	32	rim	176	14	68	11	0.39	0.07	0.0762	0.0052	0.0117	0.0005	0.68	0.0473	0.0024	74.9	3.5	74.6	4.9	100.4
35.13	32	core	226	18	169	26	0.75	0.13	0.0749	0.0048	0.0118	0.0005	0.71	0.0461	0.0021	75.6	3.5	73.4	4.6	103.1

GY93A (Inagawa granite)
Sequences: 64, 65, 66

									Isotope ratios						Age (Ma)				
Spot no.	Grain no.	Position	U (ppm)	±	Th (ppm)	±	Th/U	±	$^{207}Pb/^{235}U$	±	$^{206}Pb/^{238}U$	±	ρ	$^{207}Pb/^{206}Pb$	±	$^{206}Pb/^{238}U$	±	$^{207}Pb/^{235}U$	±	% Conc.
64.1	35	rim	347	19	136	15	0.39	0.05	0.0707	0.0045	0.0107	0.0003	0.38	0.0478	0.0028	68.7	1.7	69.4	4.3	99.1
64.2	35	core	235	13	154	17	0.65	0.08	0.0606	0.0051	0.0106	0.0003	0.31	0.0416	0.0033	67.7	1.7	59.7	4.9	113.4
64.3	71	core	169	9	118	13	0.70	0.09	0.0687	0.0064	0.0107	0.0003	0.30	0.0467	0.0041	68.4	1.9	67.4	6.0	101.4
64.4	71	core	178	10	119	13	0.67	0.08	0.0677	0.0062	0.0106	0.0003	0.30	0.0464	0.0040	67.9	1.9	66.5	5.9	102.0
64.5	69	rim	363	20	123	14	0.34	0.04	0.0691	0.0044	0.0106	0.0003	0.38	0.0473	0.0028	67.9	1.6	67.8	4.2	100.1
64.6	69	core	256	14	189	21	0.74	0.09	0.0767	0.0055	0.0109	0.0003	0.36	0.0511	0.0034	69.7	1.8	75.0	5.2	93.0
64.7	69	rim	513	28	271	30	0.53	0.07	0.0700	0.0038	0.0108	0.0002	0.42	0.0471	0.0023	69.0	1.6	68.7	3.6	100.5
64.8	68	core	590	33	322	36	0.55	0.07	0.0747	0.0037	0.0109	0.0002	0.46	0.0497	0.0022	70.0	1.6	73.2	3.5	95.6
64.9	68	rim	404	22	186	21	0.46	0.06	0.0731	0.0043	0.0109	0.0003	0.40	0.0488	0.0026	69.6	1.6	71.6	4.1	97.1
64.10	30	rim	260	14	84	9	0.32	0.04	0.0659	0.0050	0.0107	0.0003	0.34	0.0448	0.0032	68.4	1.7	64.8	4.8	105.5
64.11	30	core	620	34	325	36	0.52	0.06	0.0734	0.0036	0.0109	0.0002	0.46	0.0489	0.0021	69.7	1.6	71.9	3.4	97.0
64.12	66	rim	296	16	192	21	0.65	0.08	0.0660	0.0047	0.0106	0.0003	0.35	0.0452	0.0030	67.9	1.7	64.9	4.5	104.6
64.13	66	core	428	24	212	24	0.50	0.06	0.0701	0.0041	0.0107	0.0003	0.40	0.0475	0.0025	68.6	1.6	68.7	3.9	99.8
65.1	64	rim	319	30	100	19	0.31	0.07	0.0680	0.0047	0.0107	0.0003	0.42	0.0459	0.0029	68.9	2.0	66.8	4.4	103.2
65.2	64	core	688	64	1113	207	1.62	0.34	0.0682	0.0034	0.0109	0.0003	0.54	0.0452	0.0019	70.2	1.9	67.0	3.2	104.7
65.3	61	core	5920	552	3457	644	0.58	0.12	0.1382	0.0041	0.0108	0.0003	0.87	0.0926	0.0014	69.4	1.8	131.4	3.6	52.8
65.4	61	rim	301	28	70	13	0.23	0.05	0.0729	0.0050	0.0109	0.0003	0.42	0.0486	0.0030	69.8	2.0	71.5	4.7	97.7
65.5	24	rim	324	30	121	23	0.37	0.08	0.1066	0.0061	0.0112	0.0003	0.50	0.0689	0.0034	72.0	2.0	102.8	5.6	70.0
65.6	24	core	338	31	115	22	0.34	0.07	0.0679	0.0046	0.0109	0.0003	0.42	0.0453	0.0028	69.6	2.0	66.7	4.3	104.5
65.7	24	rim	423	39	149	28	0.35	0.07	0.0698	0.0042	0.0109	0.0003	0.46	0.0466	0.0025	69.6	1.9	68.5	4.0	101.7
65.8	22	rim	309	29	242	45	0.78	0.16	0.0726	0.0049	0.0109	0.0003	0.43	0.0483	0.0029	69.8	2.0	71.2	4.6	98.2
65.9	22	core	244	23	180	34	0.74	0.15	0.0687	0.0053	0.0110	0.0003	0.38	0.0455	0.0033	70.2	2.1	67.5	5.1	104.1
65.10	21	core	731	68	781	146	1.07	0.22	0.0742	0.0035	0.0109	0.0003	0.56	0.0494	0.0019	69.8	1.9	72.6	3.3	96.1
65.11	21	rim	246	23	141	26	0.57	0.12	0.0714	0.0054	0.0108	0.0003	0.39	0.0480	0.0033	69.1	2.0	70.0	5.1	98.7
65.12	59	core	432	40	262	49	0.61	0.13	0.0699	0.0041	0.0110	0.0003	0.47	0.0461	0.0024	70.5	1.9	68.6	3.9	102.9
65.13	59	rim	356	33	177	33	0.50	0.10	0.0736	0.0046	0.0109	0.0003	0.45	0.0489	0.0028	70.0	2.0	72.1	4.4	97.2
66.1	58	rim	334	13	184	14	0.55	0.05	0.0716	0.0052	0.0111	0.0005	0.58	0.0468	0.0028	71.1	3.0	70.2	5.0	101.4
66.2	58	core	743	28	205	15	0.28	0.02	0.0744	0.0042	0.0110	0.0005	0.73	0.0490	0.0019	70.6	2.9	72.8	4.0	96.9
66.3	58	rim	200	8	80	6	0.40	0.03	0.0724	0.0066	0.0112	0.0005	0.48	0.0467	0.0037	72.1	3.1	71.0	6.2	101.6
66.4	57	rim	221	8	117	9	0.53	0.04	0.0734	0.0063	0.0108	0.0005	0.51	0.0494	0.0037	69.1	3.0	72.0	6.0	96.0
66.5	57	core	341	13	260	20	0.76	0.06	0.0738	0.0053	0.0108	0.0005	0.59	0.0495	0.0029	69.4	2.9	72.3	5.1	95.9
66.6	20	core	356	13	182	14	0.51	0.04	0.0731	0.0052	0.0109	0.0005	0.59	0.0486	0.0028	70.0	3.0	71.6	5.0	97.7
66.7	20	rim	323	12	135	10	0.42	0.04	0.0663	0.0051	0.0107	0.0005	0.56	0.0449	0.0029	68.7	2.9	65.2	4.8	105.3

GY51A (Busetsu granite)
Sequences: 4, 5, 6, 15, 16, 17, 18, 19, 20, 63

Spot no.	Grain no.	Position	U (ppm)	±	Th (ppm)	±	Th/U	±	Isotope ratios $^{207}Pb/^{235}U$	±	$^{206}Pb/^{238}U$	±	ρ	$^{207}Pb/^{206}Pb$	±	Age (Ma) $^{206}Pb/^{238}U$	±	$^{207}Pb/^{235}U$	±	% Conc.	Remarks
4.11	53s	rim	168	9	124	14	0.74	0.09	0.0633	0.0055	0.0105	0.0004	0.40	0.0439	0.0035	67.0	2.3	62.4	5.2	107.5	
4.12	54s	rim	90	5	142	15	1.57	0.19	0.0689	0.0075	0.0109	0.0004	0.35	0.0460	0.0047	69.7	2.6	67.7	7.2	103.0	
4.13	56s	rim	127	7	113	12	0.89	0.11	0.0800	0.0071	0.0110	0.0004	0.40	0.0528	0.0043	70.5	2.5	78.2	6.7	90.2	
5.3	6s	mantle	107	10	13	2	0.12	0.03	0.1124	0.0092	0.0154	0.0005	0.42	0.0528	0.0039	98.7	3.4	108.2	8.5	91.3	
5.4	6s	mantle	135	12	15	3	0.11	0.02	0.0979	0.0077	0.0147	0.0005	0.43	0.0481	0.0034	94.4	3.2	94.8	7.2	99.5	
5.5	7s	rim	59	5	49	9	0.82	0.17	0.0530	0.0078	0.0110	0.0004	0.28	0.0351	0.0049	70.3	2.8	52.4	7.5	134.1	
5.6	61s	mantle	359	33	5	1	0.02	0.00	0.0928	0.0053	0.0149	0.0005	0.56	0.0452	0.0021	95.4	3.0	90.1	4.9	105.8	
5.7	61s	rim	186	17	10	2	0.06	0.01	0.0745	0.0058	0.0111	0.0004	0.44	0.0487	0.0034	71.1	2.4	73.0	5.5	97.4	
5.8	63s	rim	97	9	199	36	2.05	0.42	0.0871	0.0083	0.0114	0.0004	0.39	0.0554	0.0049	73.1	2.7	84.8	7.8	86.2	
5.9	65s	rim	44	4	46	8	1.06	0.22	0.0590	0.0095	0.0115	0.0005	0.27	0.0372	0.0058	73.8	3.2	58.2	9.2	126.7	
5.10	65s	rim	54	5	59	11	1.09	0.22	0.0635	0.0090	0.0109	0.0005	0.29	0.0423	0.0057	69.8	2.9	62.5	8.6	111.6	
5.11	70s	rim	141	13	45	8	0.32	0.06	0.0722	0.0063	0.0109	0.0004	0.40	0.0479	0.0038	70.1	2.5	70.8	6.0	99.1	
5.12	70s	core	580	53	32	6	0.06	0.01	3.5663	0.1317	0.2101	0.0065	0.83	0.1231	0.0025	1229.4	34.5	1542.1	29.7	79.7	
5.13	17s	mantle	181	16	91	17	0.50	0.10	0.0830	0.0062	0.0120	0.0004	0.45	0.0500	0.0033	77.1	2.6	80.9	5.9	95.3	
6.1	17s	rim	42	3	56	7	1.35	0.19	0.0468	0.0085	0.0113	0.0005	0.26	0.0300	0.0053	72.6	3.4	46.4	8.3	156.4	
6.2	75s	core	514	31	76	9	0.15	0.02	8.1313	0.3373	0.4105	0.0149	0.87	0.1437	0.0029	2217.1	68.4	2245.7	38.2	98.7	
6.3	34s	core	308	19	108	13	0.35	0.05	5.2917	0.2212	0.3307	0.0120	0.87	0.1160	0.0024	1841.9	58.5	1867.5	36.3	98.6	
6.4	34s	rim	357	22	16	2	0.04	0.01	0.0677	0.0044	0.0110	0.0004	0.57	0.0445	0.0024	70.7	2.7	66.5	4.2	106.4	
6.5	38s	rim	118	7	170	21	1.43	0.20	0.0731	0.0070	0.0111	0.0005	0.43	0.0479	0.0041	71.0	2.9	71.6	6.6	99.1	
6.6	38s	rim	128	8	180	22	1.40	0.19	0.0693	0.0065	0.0105	0.0004	0.43	0.0478	0.0041	67.4	2.7	68.0	6.2	99.1	
6.7	40s	rim	33	2	17	2	0.52	0.07	0.0568	0.0107	0.0110	0.0006	0.27	0.0375	0.0068	70.5	3.6	56.1	10.3	125.6	
6.8	41s	mantle	110	7	45	6	0.41	0.06	0.0812	0.0077	0.0117	0.0005	0.43	0.0501	0.0043	75.3	3.1	79.3	7.2	94.9	
6.9	41s	mantle	120	7	47	6	0.39	0.05	0.0801	0.0073	0.0122	0.0005	0.44	0.0476	0.0039	78.1	3.1	78.2	6.9	99.9	
6.10	44s	rim	91	6	96	12	1.06	0.14	0.0805	0.0082	0.0110	0.0005	0.41	0.0533	0.0050	70.3	2.9	78.6	7.8	89.4	
6.11	44s	rim	112	7	121	15	1.09	0.15	0.0787	0.0075	0.0108	0.0004	0.43	0.0528	0.0045	69.4	2.8	76.9	7.1	90.2	
6.12	47	rim	87	5	138	17	1.59	0.22	0.0766	0.0082	0.0111	0.0005	0.40	0.0500	0.0049	71.2	3.0	75.0	7.7	95.0	
6.13	50s	rim	58	4	105	13	1.81	0.25	0.0818	0.0101	0.0109	0.0005	0.36	0.0546	0.0063	69.7	3.1	79.8	9.5	87.3	
15.1	2	core	65	5	42	7	0.66	0.11	0.0708	0.0032	0.0105	0.0002	0.52	0.0491	0.0019	67.0	1.6	69.5	3.1	96.5	
15.2	2	core	69	5	30	5	0.44	0.08	0.0723	0.0032	0.0112	0.0003	0.52	0.0467	0.0018	72.0	1.7	70.9	3.1	101.5	
15.3	7	rim	60	5	52	8	0.88	0.15	0.0700	0.0032	0.0109	0.0003	0.51	0.0467	0.0019	69.8	1.6	68.7	3.1	101.6	
15.4	7	core	30	2	28	4	0.93	0.16	0.0703	0.0039	0.0107	0.0003	0.44	0.0477	0.0023	68.4	1.7	69.0	3.7	99.3	
15.5	7	rim	52	4	47	7	0.90	0.16	0.0722	0.0034	0.0108	0.0003	0.50	0.0484	0.0020	69.3	1.6	70.7	3.2	97.9	
15.6	8	core	283	22	26	4	0.09	0.02	0.0908	0.0034	0.0135	0.0003	0.61	0.0488	0.0014	86.3	2.0	88.2	3.2	97.8	
15.7	8	core	284	22	26	4	0.09	0.02	0.0848	0.0032	0.0131	0.0003	0.61	0.0469	0.0014	84.0	1.9	82.6	3.0	101.7	
15.8	8	mantle	139	11	31	5	0.22	0.04	0.0809	0.0032	0.0124	0.0003	0.58	0.0472	0.0015	79.6	1.8	79.0	3.0	100.8	
15.9	12	rim	42	3	26	4	0.63	0.11	0.0696	0.0035	0.0105	0.0003	0.48	0.0481	0.0021	67.3	1.6	68.3	3.3	98.6	
15.10	12	core	33	3	24	4	0.72	0.12	0.0671	0.0036	0.0107	0.0003	0.45	0.0457	0.0022	68.3	1.6	65.9	3.5	103.6	
15.11	12	rim	33	3	26	4	0.77	0.13	0.0678	0.0036	0.0109	0.0003	0.45	0.0452	0.0022	69.8	1.7	66.6	3.5	104.8	
15.12	14	rim	102	8	131	20	1.29	0.22	0.0681	0.0029	0.0106	0.0002	0.55	0.0466	0.0016	68.0	1.6	66.9	2.7	101.7	
15.13	14	rim	125	10	166	26	1.32	0.23	0.0691	0.0028	0.0106	0.0002	0.57	0.0471	0.0016	68.2	1.6	67.8	2.7	100.5	
16.1	54s	rim	95	7	195	30	2.05	0.36	0.0739	0.0032	0.0108	0.0003	0.58	0.0496	0.0018	69.4	1.7	72.4	3.0	95.8	
16.2	54s	core	95	7	226	35	2.38	0.41	0.0687	0.0030	0.0106	0.0003	0.57	0.0468	0.0017	68.2	1.7	67.4	2.9	101.1	
16.3	56s	rim	85	7	96	15	1.12	0.19	0.0704	0.0031	0.0112	0.0003	0.57	0.0457	0.0017	71.7	1.8	69.0	3.0	103.8	
16.4	56s	rim	73	6	73	11	1.00	0.17	0.0688	0.0032	0.0105	0.0003	0.55	0.0474	0.0018	67.5	1.7	67.6	3.0	99.8	
16.5	3s	mantle	257	20	5	1	0.02	0.004	0.0990	0.0038	0.0137	0.0003	0.64	0.0523	0.0015	88.0	2.2	95.8	3.5	91.8	
16.6	3s	core	563	44	336	52	0.60	0.10	0.2822	0.0105	0.0401	0.0010	0.67	0.0510	0.0014	253.5	6.2	252.4	8.3	100.4	
16.8	6s	mantle	136	11	15	2	0.11	0.02	0.0987	0.0040	0.0149	0.0004	0.62	0.0481	0.0015	95.2	2.4	95.5	3.7	99.6	
16.9	6s	rim	77	6	22	3	0.29	0.05	0.0845	0.0037	0.0124	0.0003	0.57	0.0494	0.0018	79.5	2.0	82.4	3.5	96.5	
16.10	8s	rim	46	4	64	10	1.39	0.24	0.0717	0.0036	0.0108	0.0003	0.51	0.0481	0.0021	69.3	1.8	70.3	3.4	98.6	
16.11	8s	rim	39	3	47	7	1.20	0.21	0.0725	0.0038	0.0109	0.0003	0.50	0.0484	0.0022	69.7	1.8	71.1	3.6	98.1	
16.12	11s	rim	40	3	35	5	0.89	0.15	0.0733	0.0038	0.0110	0.0003	0.50	0.0483	0.0022	70.6	1.8	71.8	3.6	98.3	
16.13	11s	rim	51	4	57	9	1.12	0.19	0.0747	0.0036	0.0109	0.0003	0.53	0.0499	0.0021	69.7	1.8	73.2	3.4	95.2	
17.1	12s	rim	30	4	32	9	1.05	0.33	0.0838	0.0048	0.0121	0.0004	0.53	0.0503	0.0024	77.3	2.3	81.7	4.5	94.7	
17.2	12s	rim	33	5	18	5	0.55	0.17	0.0775	0.0044	0.0114	0.0003	0.53	0.0491	0.0024	73.4	2.2	75.8	4.2	96.8	
17.3	12s	rim	54	8	50	14	0.92	0.28	0.0708	0.0037	0.0112	0.0003	0.57	0.0457	0.0019	72.0	2.1	69.4	3.5	103.7	
17.4	13s	rim	74	10	86	24	1.16	0.36	0.0724	0.0035	0.0109	0.0003	0.61	0.0480	0.0019	70.1	2.1	70.9	3.3	98.7	
17.5	13s	core	98	14	48	13	0.49	0.15	0.0702	0.0033	0.0110	0.0003	0.63	0.0463	0.0017	70.5	2.1	68.9	3.1	102.3	
17.6	13s	rim	81	11	88	24	1.09	0.34	0.0725	0.0035	0.0108	0.0003	0.61	0.0486	0.0018	69.3	2.0	71.1	3.3	97.5	
17.8	65s	rim	49	7	48	13	0.97	0.30	0.0695	0.0037	0.0111	0.0003	0.56	0.0453	0.0020	71.3	2.1	68.2	3.5	104.5	
17.9	65s	rim	138	19	84	23	0.61	0.19	0.0728	0.0032	0.0113	0.0003	0.66	0.0469	0.0016	72.1	2.1	71.3	3.1	101.1	
17.10	69s	rim	35	5	39	11	1.09	0.34	0.0746	0.0042	0.0109	0.0003	0.53	0.0499	0.0024	69.6	2.1	73.1	4.0	95.2	
17.13	70s	core	272	38	40	11	0.15	0.05	4.8848	0.1940	0.2676	0.0078	0.73	0.1324	0.0036	1528.7	39.6	1799.6	34.0	84.9	
18.1	21s	rim	71	4	80	8	1.14	0.13	0.0735	0.0034	0.0108	0.0003	0.51	0.0493	0.0020	69.3	1.6	72.0	3.2	96.2	
18.2	21s	core	41	2	41	4	1.00	0.12	0.0732	0.0039	0.0111	0.0003	0.46	0.0477	0.0022	71.3	1.7	71.7	3.7	99.4	
18.3	21s	rim	63	3	63	7	0.99	0.12	0.0716	0.0034	0.0108	0.0003	0.50	0.0480	0.0020	69.4	1.6	70.2	3.2	98.8	
18.4	75s	core	416	22	164	17	0.39	0.05	7.9237	0.2814	0.3748	0.0086	0.65	0.1533	0.0042	2052.1	40.4	2222.4	32.5	92.3	
18.5	75s	mantle	676	35	15	2	0.02	0.003	3.5829	0.1273	0.2140	0.0049	0.65	0.1214	0.0033	1249.9	26.1	1545.7	28.6	80.9	
18.6	77s	core	332	17	21	2	0.06	0.01	0.0894	0.0034	0.0134	0.0003	0.61	0.0484	0.0014	85.8	2.0	86.9	3.1	98.7	
18.7	77s	mantle	320	17	12	1	0.04	0.004	0.0803	0.0030	0.0121	0.0003	0.61	0.0480	0.0014	77.8	1.8	78.4	2.9	99.1	
18.10	25s	core	70	4	76	8	1.09	0.13	0.0713	0.0033	0.0108	0.0003	0.51	0.0477	0.0019	69.5	1.6	69.9	3.2	99.4	
18.11	25s	core	37	2	32	3	0.86	0.10	0.0318	0.0022	0.0109	0.0003	0.34	0.0212	0.0014	69.7	1.7	31.8	2.2	219.2	
18.12	25s	core	59	3	52	5	0.89	0.10	0.0805	0.0038	0.0109	0.0003	0.50	0.0534	0.0022	70.1	1.7	78.6	3.6	89.1	
18.13	26s	rim	125	7	164	17	1.32	0.15	0.0697	0.0029	0.0107	0.0002	0.55	0.0473	0.0017	68.5	1.6	68.4	2.8	100.2	
19.1	30s	core	110	4	159	13	1.45	0.13	0.0720	0.0031	0.0108	0.0003	0.54	0.0485	0.0017	68.9	1.6	70.6	2.9	97.7	
19.2	31s	rim	60	2	47	4	0.79	0.07	0.0750	0.0036	0.0109	0.0003	0.50	0.0499	0.0021	70.0	1.7	73.5	3.4	95.2	
19.3	31s	core	38	2	18	1	0.48	0.04	0.0865	0.0045	0.0122	0.0003	0.47	0.0513	0.0023	78.4	1.9	84.3	4.2	93.1	
19.4	31s	rim	78	3	69	6	0.89	0.08	0.0728	0.0033	0.0108	0.0003	0.52	0.0489	0.0019	69.3	1.6	71.3	3.1	97.1	
19.5	32s	rim	79	3	81	7	1.02	0.09	0.0737	0.0033	0.0109	0.0003	0.52	0.0490	0.0019	69.9	1.6	72.2	3.2	96.8	
19.6	38s	rim	56	2	48	4	0.86	0.08	0.0794	0.0038	0.0111	0.0003	0.50	0.0517	0.0022	71.4	1.7	77.6	3.6	92.1	
19.7	38s	core	36	1	35	3	0.97	0.09	0.0731	0.0040	0.0109	0.0003	0.44	0.0485	0.0024	70.0	1.7	71.6	3.8	97.8	
19.8	38s	rim	47	2	39	3	0.83	0.08	0.0829	0.0041	0.0112	0.0003	0.48	0.0535	0.0023	72.0	1.7	80.9	3.9	89.1	
19.9	41s	mantle	94	4	27	2	0.29	0.03	0.0816	0.0035	0.0123	0.0003	0.54	0.0482	0.0018	78.6	1.8	79.6	3.3	98.7	
19.10	41s	core	169	7	10	1	0.06	0.01	0.0876	0.0035	0.0133	0.0003	0.58	0.0480	0.0015	84.9	2.0	85.3	3.2	99.5	
19.11	42s	rim	32	1	28	2	0.86	0.08	0.0748	0.0042	0.0111	0.0003	0.43	0.0488	0.0025	71.3	1.7	73.3	4.0	97.3	
19.12	44s	rim	80	3	86	7	1.08	0.10	0.0718	0.0033	0.0109	0.0003	0.52	0.0480	0.0019	69.7	1.6	70.4	3.1	98.9	
19.13	44s	rim	80	3	82	7	1.02	0.09	0.0754	0.0034	0.0110	0.0003	0.52	0.0499	0.0019	70.3	1.6	73.8	3.2	95.2	
20.1	45s	core	283	6	255	12	0.90	0.05	0.0715	0.0028	0.0109	0.0003	0.60	0.0475	0.0015	70.0	1.6	70.1	2.6	99.8	
20.2	45s	rim	91	2	32	1	0.35	0.02	0.0740	0.0033	0.0112	0.0003	0.53	0.0479	0.0018	71.8	1.7	72.4	3.1	99.1	
20.3	46s	rim	57	1	55	3	0.98	0.05	0.0736	0.0036	0.0106	0.0003	0.49	0.0502	0.0021	68.3	1.6	72.2	3.4	94.6	
20.4	46s	rim	45	1	40	2	0.88	0.04	0.0712	0.0037	0.0106	0.0003	0.46	0.0485	0.0022	68.3	1.6	69.9	3.5	97.7	
20.5	48s	rim	25	1	21	1	0.83	0.04	0.0875	0.0051	0.0112	0.0003	0.43	0.0564	0.0030	72.1	1.8	85.2	4.8	84.6	
20.6	48s	rim	41	1	41	2	0.99	0.05	0.0717	0.0038	0.0108	0.0003	0.45	0.0479	0.0023	69.5	1.7	70.3	3.6	98.9	
20.7	49sa	core	77	2	87	4	1.14	0.06	0.0698	0.0032	0.0107	0.0003	0.51	0.0474	0.0019	68.6	1.6	68.5	3.1	100.1	
20.8	49sa	rim	36	1	47	2	1.29	0.07	0.0783	0.0042	0.0108	0.0003	0.45	0.0526	0.0025	69.2	1.7	76.5	4.0	90.4	
20.9	50s	core	338	8	77	4	0.23	0.01	3.0926	0.1100	0.1962	0.0045	0.65	0.1143	0.0031	1154.8	24.3	1430.9	27.7	80.7	
20.10	50s	rim	41	1	44	2	1.10	0.06	0.0771	0.0040	0.0110	0.0003	0.46	0.0510	0.0024	70.4	1.7	75.4	3.8	93.3	
20.11	71s	rim	134	3	107	5	0.80	0.04	0.0754	0.0031	0.0112	0.0003	0.56	0.0488	0.0017	71.9	1.7	73.8	3.0	97.4	
20.12	71s	rim	129	3	132	6	1.03	0.05	0.0709	0.0030	0.0106	0.0002	0.56	0.0487	0.0017	67.8	1.6	69.6	2.8	97.4	
20.13	73s	rim	44	1	41	2	0.95	0.05	0.0745	0.0039	0.0108	0.0003	0.46	0.0500	0.0023	69.3	1.7	72.9	3.7	95.0	
63.6	3-65s	mantle	259	13	4	0	0.02	0.002	0.0914	0.0170	0.0142	0.0007	0.27	0.0467	0.0084	90.8	4.4	88.8	15.8	102.3	
63.7	3-65s	core	238	12	75	7	0.31	0.04	3.6419	0.2245	0.2150	0.0085	0.64	0.1228	0.0058	1255.6	45.2	1558.7	49.1	80.5	
63.8	3-65s	mantle	229	11	6	1	0.02	0.003	0.0918	0.0191	0.0153	0.0008	0.24	0.0434	0.0088	98.2	4.9	89.2	17.8	110.1	
63.9	3-65s	rim	194	10	6	1	0.03	0.004	0.0675	0.0202	0.0108	0.0006	0.19	0.0452	0.0133	69.4	3.9	66.3	19.2	104.7	
Rejected spots																					**Remarks**
5.1	3s	rim	114	10	20	4	0.18	0.04	0.0733	0.0070	0.0120	0.0004	0.38	0.0444	0.0039	76.6	2.7	71.8	6.6	106.7	irregular signal
5.2	3s	core	270	25	32	6	0.12	0.02	0.1345	0.0075	0.0189	0.0006	0.57	0.0517	0.0024	120.6	3.8	128.1	6.7	94.1	irregular signal
16.7	3s	mantle	333	26	19	3	0.06	0.01	0.1105	0.0042	0.0164	0.0004	0.65	0.0488	0.0014	105.0	2.6	106.4	3.9	98.6	irregular signal
17.7	65s	rim	67	9	47	13	0.70	0.22	0.0853	0.0041	0.0124	0.0004	0.61	0.0501	0.0019	79.2	2.3	83.1	3.9	95.2	irregular signal
17.11	69s	core	171	24	17	5	0.10	0.03	0.0953	0.0041	0.0148	0.0004	0.68	0.0468	0.0015	94.4	2.7	92.4	3.8	102.2	irregular signal
17.12	70	mantle	290	40	32	9	0.11	0.03	1.4798	0.0589	0.1002	0.0029	0.73	0.1071	0.0029	615.6	17.0	922.1	24.4	66.8	irregular signal
18.8	78s	rim	116	6	51	5	0.43	0.05	0.0896	0.0037	0.0135	0.0003	0.56	0.0482	0.0016	86.3	2.0	87.1	3.4	99.0	irregular signal
18.9	78s	rim	130	7	53	6	0.41	0.05	0.1048	0.0042	0.0158	0.0004	0.58	0.0480	0.0016	101.2	2.3	101.2	3.9	100.0	irregular signal
63.5	3-65s	mantle	78	4	80	9	1.03	0.12	0.0619	0.0431	0.0118	0.0009	0.11	0.0381	0.0264	75.5	5.9	61.0	41.3	123.8	irregular signal

MK02M (Busetsu granite)
Sequences: 44, 45

Spot no.	Grain no.	Position	U (ppm)	±	Th (ppm)	±	Th/U	±	Isotope ratios $^{207}Pb/^{235}U$	±	$^{206}Pb/^{238}U$	±	ρ	$^{207}Pb/^{206}Pb$	±	Age (Ma) $^{206}Pb/^{238}U$	±	$^{207}Pb/^{235}U$	±	% Conc.	Remarks
44.1	45s	rim	1155	108	1324	247	1.15	0.24	0.0727	0.0036	0.0110	0.0005	0.90	0.0481	0.0010	70.4	3.2	71.3	3.4	98.7	
44.2	46s	rim	570	53	384	72	0.67	0.14	0.0700	0.0038	0.0109	0.0005	0.84	0.0466	0.0014	69.9	3.1	68.7	3.6	101.8	
44.3	46s	rim	488	45	221	41	0.45	0.09	0.0725	0.0040	0.0112	0.0005	0.83	0.0472	0.0015	71.5	3.2	71.1	3.8	100.6	
44.4	1a	core	457	43	207	39	0.45	0.09	0.0719	0.0040	0.0109	0.0005	0.82	0.0478	0.0015	69.9	3.2	70.5	3.8	99.3	
44.5	1s	rim	836	78	698	130	0.83	0.17	0.0730	0.0037	0.0109	0.0005	0.88	0.0487	0.0012	69.6	3.1	71.5	3.6	97.4	
44.6	4s	core	328	31	112	21	0.34	0.07	5.2266	0.2413	0.3148	0.0141	0.97	0.1204	0.0013	1764.5	69.6	1857.0	40.1	95.0	
44.7	4s	rim	3820	356	96	18	0.03	0.01	0.0731	0.0034	0.0111	0.0005	0.95	0.0479	0.0007	71.0	3.2	71.6	3.3	99.1	
44.8	24s	core	911	85	548	102	0.60	0.13	0.0703	0.0036	0.0107	0.0005	0.88	0.0476	0.0011	68.8	3.1	69.0	3.4	99.6	
44.9	24s	rim	592	55	323	60	0.54	0.11	0.0729	0.0039	0.0109	0.0005	0.85	0.0486	0.0014	69.8	3.1	71.5	3.7	97.7	
44.10	72s	rim	654	61	319	59	0.49	0.10	0.0706	0.0037	0.0107	0.0005	0.85	0.0480	0.0013	68.3	3.1	69.3	3.6	98.7	
44.11	72s	rim	324	30	97	18	0.30	0.06	0.0714	0.0042	0.0107	0.0005	0.77	0.0484	0.0018	68.7	3.1	70.0	4.0	98.0	
44.12	27s	rim	2196	205	358	67	0.16	0.03	0.0728	0.0035	0.0112	0.0005	0.93	0.0473	0.0008	71.5	3.2	71.3	3.3	100.3	
44.13	28s	rim	649	60	643	120	0.99	0.21	0.0731	0.0039	0.0109	0.0005	0.86	0.0488	0.0013	69.6	3.1	71.6	3.7	97.2	
45.1	29s	mantle	353	26	138	20	0.39	0.06	0.0804	0.0046	0.0124	0.0006	0.80	0.0470	0.0016	79.4	3.6	78.5	4.3	101.2	
45.2	29s	rim	1714	124	944	137	0.55	0.09	0.0739	0.0036	0.0113	0.0005	0.93	0.0474	0.0009	72.4	3.2	72.4	3.4	100.0	
45.3	30s	mantle	493	36	14	2	0.03	0.005	0.0945	0.0050	0.0140	0.0006	0.86	0.0491	0.0013	89.4	4.0	91.7	4.6	97.5	
45.4	30s	rim	1051	76	337	49	0.32	0.05	0.0736	0.0037	0.0114	0.0005	0.90	0.0467	0.0010	73.3	3.3	72.1	3.5	101.6	
45.5	82s	rim	1067	77	381	55	0.36	0.06	0.0751	0.0038	0.0116	0.0005	0.90	0.0472	0.0010	74.0	3.3	73.5	3.6	100.7	
45.6	82s	rim	1333	97	606	88	0.45	0.07	0.0731	0.0036	0.0114	0.0005	0.91	0.0465	0.0009	73.1	3.3	71.7	3.4	102.0	
45.7	34s	core	630	46	275	40	0.44	0.07	0.0784	0.0041	0.0120	0.0005	0.86	0.0472	0.0013	77.2	3.5	76.6	3.9	100.8	
45.8	34s	rim	210	15	102	15	0.49	0.08	0.0694	0.0045	0.0107	0.0005	0.70	0.0470	0.0022	68.7	3.2	68.1	4.3	100.8	
45.9	36s	rim	346	25	260	38	0.75	0.12	0.0765	0.0044	0.0117	0.0005	0.79	0.0475	0.0017	74.9	3.4	74.9	4.2	100.0	
45.10	86s	rim	527	38	272	39	0.52	0.08	0.0734	0.0040	0.0115	0.0005	0.84	0.0463	0.0014	73.7	3.3	72.0	3.8	102.4	
45.12	40s	core	489	35	238	34	0.49	0.08	0.0691	0.0038	0.0109	0.0005	0.82	0.0461	0.0015	69.7	3.1	67.9	3.6	102.7	
45.13	40s	rim	497	36	207	30	0.42	0.07	0.0734	0.0040	0.0112	0.0005	0.83	0.0476	0.0014	71.8	3.2	71.9	3.8	99.8	
Rejected spots																					**Remarks**
45.11	86s	mantle	90	7	33	5	0.37	0.06	0.3282	0.0195	0.0135	0.0006	0.80	0.1762	0.0063	86.5	4.1	288.2	15.0	30.0	irregular signal

GY89A (Busetsu granite)
Sequences: 46, 47

Spot no.	Grain no.	Position	U (ppm)	±	Th (ppm)	±	Th/U	±	Isotope ratios $^{207}Pb/^{235}U$	±	$^{206}Pb/^{238}U$	±	ρ	$^{207}Pb/^{206}Pb$	±	Age (Ma) $^{206}Pb/^{238}U$	±	$^{207}Pb/^{235}U$	±	% Conc.	Remarks
46.1	1s	rim	269	20	113	17	0.42	0.07	0.0749	0.0046	0.0110	0.0005	0.75	0.0496	0.0020	70.2	3.2	73.4	4.3	95.7	
46.4	14s	core	697	52	238	36	0.34	0.06	0.1014	0.0051	0.0160	0.0007	0.89	0.0460	0.0011	102.2	4.6	98.1	4.8	104.2	
46.5	14s	rim	764	57	397	60	0.52	0.09	0.1008	0.0051	0.0151	0.0007	0.89	0.0484	0.0011	96.6	4.3	97.5	4.7	99.0	
46.6	19s	rim	1926	145	162	24	0.08	0.01	0.0695	0.0034	0.0107	0.0005	0.93	0.0473	0.0009	68.3	3.1	68.2	3.2	100.2	
46.7	19s	core	182	14	139	21	0.76	0.13	0.2507	0.0133	0.0359	0.0016	0.85	0.0506	0.0014	227.5	10.1	227.1	10.9	100.2	
46.9	69s	core	378	28	58	9	0.15	0.03	5.3407	0.2464	0.3348	0.0150	0.97	0.1157	0.0013	1861.8	72.9	1875.4	40.2	99.3	
46.10	69s	core	364	27	178	27	0.49	0.08	5.4434	0.2511	0.3435	0.0154	0.97	0.1149	0.0013	1903.6	74.3	1891.7	40.4	100.6	
46.11	71s	rim	150	11	254	38	1.70	0.28	0.0723	0.0052	0.0109	0.0005	0.65	0.0483	0.0026	69.6	3.2	70.8	4.9	98.3	
46.13	71s	rim	486	37	34	5	0.07	0.01	0.0744	0.0041	0.0115	0.0005	0.83	0.0469	0.0015	73.7	3.3	72.9	3.9	101.2	
47.1	79s	rim	1141	166	51	15	0.04	0.01	0.0714	0.0036	0.0110	0.0005	0.90	0.0472	0.0010	70.3	3.2	70.0	3.4	100.4	
47.2	34s	core	253	37	139	40	0.55	0.18	0.2079	0.0109	0.0301	0.0014	0.87	0.0501	0.0013	191.2	8.5	191.8	9.2	99.7	
47.3	34s	rim	693	101	77	22	0.11	0.04	0.0709	0.0037	0.0108	0.0005	0.86	0.0477	0.0013	69.1	3.1	69.5	3.5	99.4	
47.4	89s	core	95	14	58	17	0.62	0.20	0.2581	0.0151	0.0367	0.0017	0.78	0.0510	0.0019	232.2	10.4	233.2	12.3	99.6	
47.5	89s	rim	1253	182	151	44	0.12	0.04	0.0725	0.0036	0.0110	0.0005	0.91	0.0480	0.0010	70.3	3.1	71.1	3.4	98.9	
47.6	90s	core	165	24	96	28	0.58	0.19	0.0676	0.0048	0.0108	0.0005	0.66	0.0454	0.0024	69.2	3.2	66.4	4.5	104.2	
47.7	90s	rim	89	13	45	13	0.50	0.16	0.0748	0.0062	0.0114	0.0005	0.57	0.0475	0.0032	73.2	3.5	73.3	5.9	100.0	
47.8	91s	rim	934	136	270	79	0.29	0.09	0.0763	0.0039	0.0116	0.0005	0.89	0.0478	0.0011	74.2	3.3	74.7	3.6	99.4	
47.9	91s	core	385	56	50	14	0.13	0.04	5.1409	0.2371	0.3197	0.0143	0.97	0.1166	0.0013	1788.5	70.4	1842.9	40.0	97.0	
47.10	93s	rim	1702	247	182	53	0.11	0.03	0.0723	0.0035	0.0112	0.0005	0.92	0.0467	0.0009	71.9	3.2	70.8	3.3	101.5	
47.11	93s	core	329	48	220	64	0.67	0.22	0.3048	0.0150	0.0428	0.0019	0.91	0.0516	0.0010	270.2	11.9	270.2	11.8	100.0	
47.12	93s	rim	2575	374	513	149	0.20	0.06	0.0730	0.0035	0.0111	0.0005	0.94	0.0477	0.0008	71.0	3.2	71.5	3.3	99.4	
47.13	95s	core	395	57	537	156	1.36	0.44	0.0707	0.0040	0.0107	0.0005	0.80	0.0479	0.0017	68.6	3.1	69.4	3.8	98.9	
Rejected spots																					**Remarks**
46.2	4s	rim	281	21	67	10	0.24	0.04	0.0800	0.0048	0.0119	0.0005	0.76	0.0487	0.0019	76.3	3.5	78.1	4.5	97.6	irregular signal
46.3	4s	core	341	26	267	40	0.78	0.13	0.0805	0.0046	0.0124	0.0006	0.79	0.0470	0.0017	79.6	3.6	78.6	4.4	101.2	irregular signal
46.8	69s	rim	827	62	91	14	0.11	0.02	0.0732	0.0038	0.0112	0.0005	0.88	0.0472	0.0012	72.1	3.2	71.7	3.6	100.5	irregular signal
46.12	71s	core	490	37	23	3	0.05	0.01	0.0927	0.0049	0.0130	0.0006	0.85	0.0519	0.0015	83.0	3.7	90.1	4.6	92.2	irregular signal

GY03D (~20 cm thick leucosome in metatexite)
Sequences: 41, 42, 43

Spot no.	Grain no.	Position	U (ppm)	±	Th (ppm)	±	Th/U	±	Isotope ratios $^{207}Pb/^{235}U$	±	$^{206}Pb/^{238}U$	±	ρ	$^{207}Pb/^{206}Pb$	±	Age (Ma) $^{206}Pb/^{238}U$	±	$^{207}Pb/^{235}U$	±	% Conc.	
41.1	3s	inner rim	792	47	6	1	0.01	0.001	0.1007	0.0051	0.0151	0.0007	0.90	0.0485	0.0011	96.4	4.3	97.5	4.7	98.9	
41.2	3s	core	254	15	367	44	1.45	0.19	11.0508	0.5094	0.4811	0.0216	0.97	0.1666	0.0018	2532.0	94.6	2527.4	43.9	100.2	
41.3	6s	outer rim	3327	198	12	1	0.004	0.000	0.0872	0.0041	0.0131	0.0006	0.95	0.0481	0.0007	84.2	3.8	84.9	3.8	99.2	
41.4	6s	core	1422	85	104	12	0.07	0.01	1.1100	0.0512	0.1082	0.0049	0.97	0.0744	0.0008	662.6	28.3	758.2	25.0	87.4	
41.5	7s	inner rim	331	20	17	2	0.05	0.01	0.1069	0.0059	0.0155	0.0007	0.82	0.0502	0.0016	98.8	4.5	103.1	5.4	95.9	
41.6	7s	core	504	30	135	16	0.27	0.04	0.2184	0.0107	0.0306	0.0014	0.92	0.0517	0.0010	194.6	8.6	200.6	9.0	97.0	
41.7	7s	outer rim	2718	162	12	1	0.004	0.001	0.0940	0.0044	0.0142	0.0006	0.95	0.0480	0.0007	90.9	4.1	91.3	4.1	99.6	
41.8	8s	core	403	24	138	16	0.34	0.05	4.8498	0.2238	0.3068	0.0138	0.97	0.1147	0.0012	1724.9	68.2	1793.6	39.6	96.2	
41.9	8s	core	470	28	111	13	0.24	0.03	4.6304	0.2135	0.2955	0.0132	0.97	0.1137	0.0012	1668.9	66.3	1754.8	39.3	95.1	
41.10	8s	inner rim	254	15	28	3	0.11	0.01	0.1002	0.0058	0.0155	0.0007	0.78	0.0470	0.0017	98.9	4.5	96.9	5.4	102.0	
41.11	9s	core	226	13	55	7	0.24	0.03	2.0814	0.0974	0.1367	0.0061	0.96	0.1104	0.0015	826.2	34.9	1142.7	32.6	72.3	
41.12	9s	outer rim	3375	201	14	2	0.004	0.001	0.0959	0.0045	0.0145	0.0007	0.95	0.0479	0.0007	92.8	4.1	93.0	4.2	99.9	
41.13	9s	outer rim	3828	228	11	1	0.003	0.000	0.0942	0.0044	0.0144	0.0006	0.96	0.0476	0.0007	91.9	4.1	91.4	4.1	100.5	
42.1	11s	core	669	58	900	156	1.35	0.26	0.3157	0.0150	0.0445	0.0020	0.94	0.0514	0.0008	280.7	12.3	278.6	11.7	100.8	
42.2	11s	outer rim	2367	204	7	1	0.003	0.001	0.0914	0.0044	0.0137	0.0006	0.94	0.0485	0.0008	87.4	3.9	88.8	4.1	98.5	
42.3	13s	core	240	21	150	26	0.62	0.12	0.1401	0.0078	0.0209	0.0009	0.81	0.0487	0.0016	133.0	6.0	133.1	7.0	99.9	
42.4	13s	outer rim	4635	400	15	3	0.003	0.001	0.0965	0.0045	0.0146	0.0007	0.96	0.0481	0.0006	93.2	4.2	93.5	4.2	99.7	
42.5	15s	core	1366	118	1260	218	0.92	0.18	0.2671	0.0125	0.0374	0.0017	0.96	0.0518	0.0007	236.9	10.4	240.4	10.1	98.5	
42.6	15s	inner rim	709	61	57	10	0.08	0.02	0.0959	0.0049	0.0144	0.0007	0.88	0.0481	0.0012	92.5	4.1	93.0	4.5	99.5	
42.7	18s	core	473	41	501	87	1.06	0.20	0.2775	0.0135	0.0398	0.0018	0.92	0.0506	0.0009	251.6	11.1	248.7	10.8	101.2	
42.8	18s	outer rim	3289	284	35	6	0.01	0.00	0.0988	0.0047	0.0149	0.0007	0.95	0.0482	0.0007	95.1	4.2	95.7	4.3	99.4	
42.9	19s	core	292	25	53	9	0.18	0.03	4.6994	0.2173	0.2967	0.0133	0.97	0.1149	0.0013	1674.9	66.5	1767.1	39.5	94.8	
42.10	19s	outer rim	3674	317	14	2	0.004	0.001	0.0925	0.0043	0.0138	0.0006	0.95	0.0485	0.0007	88.5	3.9	89.8	4.0	98.5	
42.11	20s	core	2429	210	1263	218	0.52	0.10	0.1235	0.0058	0.0173	0.0008	0.95	0.0516	0.0007	110.8	4.9	118.2	5.3	93.8	
42.12	20s	inner rim	799	69	12	2	0.01	0.003	0.1047	0.0052	0.0161	0.0007	0.90	0.0472	0.0010	102.9	4.6	101.1	4.8	101.8	
42.13	20s	outer rim	3694	319	14	2	0.004	0.001	0.0890	0.0042	0.0134	0.0006	0.95	0.0480	0.0007	86.0	3.8	86.6	3.9	99.4	
43.2	28s	core	2848	145	1481	151	0.52	0.06	0.1824	0.0085	0.0262	0.0012	0.96	0.0505	0.0006	166.8	7.4	170.1	7.3	98.0	
43.3	31s	outer rim	4651	237	14	1	0.003	0.000	0.0875	0.0041	0.0130	0.0006	0.96	0.0489	0.0007	83.1	3.7	85.1	3.8	97.5	
43.4	31s	core	381	19	16	2	0.04	0.005	0.1623	0.0084	0.0196	0.0009	0.87	0.0602	0.0015	124.9	5.6	152.7	7.4	81.7	
43.5	41s	core	823	42	443	45	0.54	0.06	0.2078	0.0100	0.0301	0.0014	0.94	0.0500	0.0009	191.3	8.5	191.7	8.4	99.8	
43.6	41s	outer rim	4561	233	26	3	0.01	0.001	0.0895	0.0042	0.0131	0.0006	0.96	0.0494	0.0007	84.1	3.8	87.0	3.9	96.7	
43.7	43s	outer rim	3203	163	12	1	0.004	0.000	0.0912	0.0043	0.0138	0.0006	0.95	0.0480	0.0007	88.2	3.9	88.6	4.0	99.6	
43.8	46s	core	285	15	176	18	0.62	0.07	0.1846	0.0097	0.0265	0.0012	0.86	0.0506	0.0014	168.4	7.5	172.0	8.3	97.9	
43.9	46s	core	1678	86	842	86	0.50	0.06	0.1846	0.0087	0.0267	0.0012	0.95	0.0501	0.0007	169.9	7.5	172.0	7.5	98.7	
43.10	53s	outer rim	4132	211	17	2	0.004	0.000	0.0876	0.0041	0.0131	0.0006	0.96	0.0484	0.0007	84.1	3.7	85.3	3.8	98.6	
43.11	53s	inner rim	869	44	57	6	0.07	0.01	0.1025	0.0051	0.0157	0.0007	0.90	0.0473	0.0010	100.5	4.5	99.0	4.7	101.5	
43.13	54s	inner rim	1215	62	16	2	0.01	0.002	0.0952	0.0047	0.0145	0.0007	0.92	0.0476	0.0009	92.8	4.1	92.3	4.3	100.5	
Rejected spots																					**Remarks**
43.1	28s	outer rim	5877	300	256	26	0.04	0.005	0.1546	0.0072	0.0116	0.0005	0.97	0.0965	0.0011	74.5	3.3	146.0	6.3	51.0	mixed analysis
43.12	54s	core	814	42	52	5	0.06	0.01	0.1287	0.0064	0.0175	0.0008	0.91	0.0534	0.0011	111.7	5.0	122.9	5.7	90.8	irregular signal

GY47A (Pegmatite)
Sequences: 9, 27

Spot no.	Grain no.	Position	U (ppm)	±	Th (ppm)	±	Th/U	±	Isotope ratios $^{207}Pb/^{235}U$	±	$^{206}Pb/^{238}U$	±	ρ	$^{207}Pb/^{206}Pb$	±	Age (Ma) $^{206}Pb/^{238}U$	±	$^{207}Pb/^{235}U$	±	% Conc.	
9.1	1	core	936	64	37	5	0.04	0.01	3.6126	0.1500	0.2382	0.0086	0.87	0.1100	0.0022	1377.4	45.1	1552.3	33.6	88.7	
9.2	1	core	492	34	28	4	0.06	0.01	4.4928	0.1873	0.2891	0.0105	0.87	0.1127	0.0023	1636.9	52.7	1729.6	35.2	94.6	
9.3	1	rim	1021	70	6	1	0.01	0.001	0.0906	0.0045	0.0143	0.0005	0.74	0.0458	0.0015	91.7	3.3	88.0	4.2	104.2	
9.4	1s	core	234	16	56	8	0.24	0.04	5.2519	0.2208	0.3378	0.0123	0.86	0.1127	0.0024	1876.3	59.4	1861.1	36.5	100.8	
9.5	1s	core	575	39	309	42	0.54	0.08	7.4527	0.3091	0.4047	0.0147	0.87	0.1336	0.0027	2190.4	67.7	2167.3	37.8	101.1	
9.6	1s	rim	1648	113	10	1	0.01	0.001	0.0959	0.0044	0.0144	0.0005	0.79	0.0482	0.0014	92.3	3.3	93.0	4.1	99.3	
9.7	2s	rim	1239	85	5	1	0.004	0.001	0.0894	0.0043	0.0136	0.0005	0.76	0.0475	0.0015	87.4	3.2	86.9	4.0	100.5	
9.8	2s	core	242	17	163	22	0.67	0.10	0.2406	0.0130	0.0338	0.0013	0.69	0.0515	0.0020	214.6	7.8	218.9	10.7	98.0	
9.9	3s	rim	1305	90	7	1	0.01	0.001	0.0933	0.0045	0.0146	0.0005	0.77	0.0464	0.0014	93.3	3.4	90.6	4.1	103.0	
9.10	3s	core	1068	73	715	98	0.67	0.10	0.1720	0.0079	0.0258	0.0009	0.80	0.0483	0.0013	164.5	5.9	161.1	6.8	102.1	
9.11	3s	rim	2775	190	11	2	0.004	0.001	0.0906	0.0040	0.0140	0.0005	0.82	0.0470	0.0012	89.5	3.2	88.0	3.8	101.7	
9.12	4s	rim	2544	175	14	2	0.01	0.001	0.0945	0.0042	0.0144	0.0005	0.82	0.0476	0.0012	92.2	3.3	91.7	3.9	100.6	
27.9	1s	rim	1818	68	12	1	0.01	0.001	0.0923	0.0036	0.0141	0.0005	0.94	0.0476	0.0006	90.0	3.3	89.7	3.3	100.4	
27.10	2s	rim	1858	70	26	2	0.01	0.001	0.1048	0.0040	0.0141	0.0005	0.95	0.0539	0.0006	90.2	3.3	101.2	3.7	89.1	
27.11	2s	rim	1458	55	9	1	0.01	0.001	0.0921	0.0036	0.0141	0.0005	0.93	0.0474	0.0007	90.2	3.3	89.4	3.4	100.9	
27.12	3s	rim	1598	60	8	1	0.01	0.000	0.0900	0.0035	0.0137	0.0005	0.94	0.0476	0.0007	87.8	3.2	87.5	3.3	100.4	
27.13	3s	rim	2308	87	16	1	0.01	0.001	0.0954	0.0036	0.0139	0.0005	0.95	0.0500	0.0006	88.7	3.2	92.5	3.4	95.8	
Rejected spots																					**Remarks**
9.13	4s	mixed	1298	89	82	11	0.06	0.01	0.1191	0.0055	0.0178	0.0007	0.79	0.0484	0.0014	113.9	4.1	114.2	5.0	99.7	mixed analysis
27.8	1s	rim	3201	121	34	3	0.01	0.001	0.1018	0.0038	0.0154	0.0006	0.97	0.0479	0.0005	98.7	3.6	98.5	3.5	100.3	irregular signal

Table S3

Representative amphibole analyses from sample GY33A.

Grain	1	1	1	1	1	1	1	1	2	2	2	2	2	2	2	2	2
Spot	1	2	3	4	5	6	7	8	12	13	14	15	16	17	18	19	20
Position	rim	rim	rim	rim	rim	rim	core	core	rim	rim	rim	rim	rim	rim	rim	core	core
SiO_2	42.28	43.14	43.00	44.52	42.48	43.38	44.27	44.11	43.07	42.99	42.44	43.23	42.92	43.26	42.91	43.68	43.71
TiO_2	1.08	1.13	0.96	1.12	1.03	1.09	1.26	1.32	0.82	1.08	1.07	1.07	1.00	1.06	1.22	1.40	1.40
Al_2O_3	11.30	10.71	10.99	9.02	11.61	10.71	9.29	9.50	11.35	10.73	11.01	10.08	11.17	11.30	10.56	9.46	9.56
Cr_2O_3	0.03	0.06	0.01	b.d.	0.04	0.07	0.07	0.09	b.d.	b.d.	0.02	b.d.	0.04	0.02	0.04	0.01	b.d.
FeO	21.86	22.14	20.69	21.41	22.37	22.22	22.03	21.44	21.98	22.16	22.39	22.00	22.17	21.79	23.01	22.05	21.03
MnO	0.62	0.46	0.65	0.69	0.51	0.62	0.72	0.97	0.66	0.50	0.55	0.47	0.64	0.86	0.52	0.63	0.73
MgO	6.25	6.40	6.30	7.08	5.79	6.29	6.74	6.69	5.87	6.42	6.20	6.35	5.96	6.00	6.38	6.35	6.43
CaO	11.80	11.45	11.71	11.49	11.62	11.59	11.75	11.27	11.86	11.50	11.58	11.42	11.60	11.52	11.80	10.91	10.89
BaO	b.d.	0.03	0.01	0.06	0.03	b.d.	b.d.	0.03	b.d.	0.05	0.05	0.15	0.01	b.d.	0.13	b.d.	0.04
Na_2O	1.26	1.28	1.14	1.04	1.26	1.32	1.19	1.26	1.12	1.18	1.24	1.08	1.22	1.28	1.15	1.24	1.35
K_2O	1.39	1.37	1.31	1.09	1.49	1.38	1.21	1.26	1.52	1.37	1.43	1.36	1.38	1.54	1.35	1.19	1.30
F	b.d.	b.d.	0.02	0.01	b.d.	0.03	0.06	b.d.	0.03	0.01	0.07	b.d.	b.d.	0.01	0.05	0.07	b.d.
Cl	0.19	0.17	0.18	0.16	0.18	0.17	0.18	0.20	0.17	0.18	0.17	0.17	0.17	0.18	0.17	0.21	0.20
O=F	b.d.	b.d.	0.01	b.d.	b.d.	0.01	0.03	b.d.	0.01	b.d.	0.03	b.d.	b.d.	0.01	0.02	0.03	b.d.
O=Cl	0.04	0.04	0.04	0.04	0.04	0.04	0.04	0.04	0.04	0.04	0.04	0.04	0.04	0.04	0.04	0.05	0.04
Total (wt.%)	98.00	98.29	96.90	97.63	98.35	98.83	98.69	98.08	98.38	98.11	98.15	97.34	98.23	98.77	99.22	97.13	96.59
Number of O	23	23	23	23	23	23	23	23	23	23	23	23	23	23	23	23	23
Si	6.52	6.62	6.65	6.83	6.53	6.62	6.75	6.76	6.60	6.61	6.54	6.70	6.59	6.60	6.56	6.76	6.78
Ti	0.13	0.13	0.11	0.13	0.12	0.12	0.14	0.15	0.09	0.12	0.12	0.12	0.12	0.12	0.14	0.16	0.16
Al	2.05	1.94	2.00	1.63	2.10	1.93	1.67	1.72	2.05	1.94	2.00	1.84	2.02	2.03	1.90	1.73	1.75
Cr	b.d.	0.01	b.d.	b.d.	b.d.	0.01	0.01	0.01	b.d.	b.d.	b.d.	b.d.	0.01	b.d.	0.01	b.d.	b.d.
Fe	2.82	2.84	2.67	2.75	2.88	2.84	2.81	2.75	2.82	2.85	2.89	2.85	2.85	2.78	2.94	2.85	2.73
Mn	0.08	0.06	0.08	0.09	0.07	0.08	0.09	0.13	0.09	0.07	0.07	0.06	0.08	0.11	0.07	0.08	0.10
Mg	1.44	1.46	1.45	1.62	1.33	1.43	1.53	1.53	1.34	1.47	1.43	1.47	1.36	1.37	1.45	1.47	1.49
Ca	1.95	1.88	1.94	1.89	1.91	1.90	1.92	1.85	1.95	1.89	1.91	1.90	1.91	1.88	1.93	1.81	1.81
Ba	b.d.	b.d.	b.d.	b.d.	b.d.	b.d.	b.d.	b.d.	b.d.	b.d.	b.d.	0.01	b.d.	b.d.	0.01	b.d.	b.d.
Na	0.38	0.38	0.34	0.31	0.37	0.39	0.35	0.37	0.33	0.35	0.37	0.32	0.36	0.38	0.34	0.37	0.41
K	0.27	0.27	0.26	0.21	0.29	0.27	0.24	0.25	0.30	0.27	0.28	0.27	0.27	0.30	0.26	0.24	0.26
F	b.d.	b.d.	0.01	b.d.	b.d.	0.01	0.03	b.d.	0.01	b.d.	0.03	b.d.	b.d.	0.01	0.02	0.03	b.d.
Cl	0.05	0.04	0.05	0.04	0.05	0.04	0.05	0.05	0.04	0.05	0.04	0.04	0.04	0.05	0.04	0.05	0.05
Total cation	15.63	15.58	15.51	15.46	15.61	15.59	15.52	15.51	15.56	15.58	15.62	15.54	15.57	15.57	15.61	15.47	15.49

b.d.: below detection limit.

Table S4

Representative amphibole analyses from sample GY81B.

Grain	1	1	1	1	1	1	1	1	1	1	1	1	1	2	2	2	2	2	2	2	2	2
Spot	1	2	3	4	5	6	7	8	9	10	11	12	13	14	15	16	17	18	19	20	21	22
Position	rim	rim	rim	rim	rim	rim	rim	rim	rim	rim	core	core	core	rim	rim	rim	rim	rim	rim	rim	core	core
SiO_2	43.83	42.90	44.06	44.37	43.40	44.26	45.25	44.35	44.19	43.79	43.93	44.78	43.58	43.73	43.80	44.07	44.32	44.19	44.40	44.81	43.05	43.55
TiO_2	1.31	1.22	1.24	1.29	1.27	1.24	1.26	1.30	1.08	1.20	1.33	1.16	1.77	1.27	1.10	1.29	1.55	1.20	1.57	1.25	2.01	2.16
Al_2O_3	10.78	12.00	10.49	10.13	10.67	9.76	9.79	9.26	10.60	9.97	10.01	9.67	9.53	10.11	10.30	10.14	10.03	9.89	9.85	10.03	9.70	9.33
Cr_2O_3	0.04	b.d.	0.03	0.04	0.01	0.02	0.05	0.01	b.d.	0.03	b.d.	0.05	b.d.	b.d.	b.d.	b.d.	0.01	b.d.	b.d.	0.01	0.04	0.07
FeO	21.02	21.79	21.13	22.26	20.99	21.83	21.62	21.71	21.85	21.15	21.99	21.52	21.25	20.54	19.57	20.65	20.82	21.21	21.03	22.72	22.24	21.13
MnO	0.78	0.64	0.69	0.80	0.48	0.61	0.71	0.71	0.49	0.71	0.66	0.78	0.54	0.55	0.64	0.62	0.73	0.57	0.52	0.64	0.71	0.59
MgO	6.49	5.94	6.53	6.80	6.69	7.09	6.98	6.98	6.49	6.56	6.62	6.88	6.55	6.67	6.54	6.78	6.73	6.93	7.24	7.02	6.65	6.35
CaO	11.32	11.68	11.43	11.48	11.40	11.20	11.54	11.10	11.42	11.38	11.04	11.68	10.99	11.74	11.63	11.65	11.63	11.57	11.38	11.56	10.87	11.11
BaO	0.06	0.12	b.d.	b.d.	b.d.	0.04	0.04	b.d.	0.04	0.04	b.d.	b.d.	0.03	0.07	b.d.	b.d.	0.12	b.d.	0.04	0.05	0.04	0.06
Na_2O	1.18	1.06	1.01	1.06	0.95	1.00	0.95	1.11	0.99	1.10	1.19	0.87	1.14	1.03	0.94	0.93	1.09	1.05	0.95	0.88	1.21	1.29
K_2O	1.02	1.28	1.01	0.98	1.04	0.95	0.83	0.82	1.06	0.98	1.06	0.91	0.95	1.02	1.04	0.96	0.94	0.92	0.96	0.90	1.04	1.13
F	b.d.	b.d.	b.d.	b.d.	b.d.	b.d.	b.d.	b.d.	b.d.	b.d.	b.d.	b.d.	b.d.	b.d.	b.d.	b.d.	b.d.	b.d.	b.d.	b.d.	b.d.	b.d.
Cl	0.15	0.15	0.12	0.13	0.13	0.13	0.12	0.12	0.13	0.13	0.14	0.13	0.15	0.14	0.14	0.13	0.14	0.13	0.14	0.12	0.21	0.26
O=F	b.d.	b.d.	b.d.	b.d.	b.d.	b.d.	b.d.	b.d.	b.d.	b.d.	b.d.	b.d.	b.d.	b.d.	b.d.	b.d.	b.d.	b.d.	b.d.	b.d.	b.d.	b.d.
O=Cl	0.03	0.03	0.03	0.03	0.03	0.03	0.03	0.03	0.03	0.03	0.03	0.03	0.03	0.03	0.03	0.03	0.03	0.03	0.03	0.03	0.05	0.06
Total (wt.%)	97.94	98.74	97.70	99.32	96.99	98.09	99.12	97.43	98.31	97.00	97.93	98.39	96.44	96.83	95.66	97.17	98.08	97.61	98.02	99.95	97.71	96.97
Number of O	23	23	23	23	23	23	23	23	23	23	23	23	23	23	23	23	23	23	23	23	23	23
Si	6.69	6.54	6.73	6.71	6.68	6.75	6.81	6.81	6.73	6.75	6.73	6.80	6.76	6.74	6.79	6.76	6.75	6.76	6.75	6.73	6.64	6.74
Ti	0.15	0.14	0.14	0.15	0.15	0.14	0.14	0.15	0.12	0.14	0.15	0.13	0.21	0.15	0.13	0.15	0.18	0.14	0.18	0.14	0.23	0.25
Al	1.94	2.15	1.89	1.81	1.94	1.76	1.74	1.68	1.90	1.81	1.81	1.73	1.74	1.84	1.88	1.83	1.80	1.78	1.76	1.78	1.76	1.70
Cr	0.01	b.d.	b.d.	b.d.	b.d.	b.d.	0.01	b.d.	b.d.	b.d.	b.d.	0.01	b.d.	b.d.	b.d.	b.d.	b.d.	b.d.	b.d.	b.d.	0.01	0.01
Fe	2.68	2.78	2.70	2.81	2.70	2.79	2.72	2.79	2.78	2.73	2.82	2.73	2.76	2.65	2.54	2.65	2.65	2.71	2.67	2.85	2.87	2.73
Mn	0.10	0.08	0.09	0.10	0.06	0.08	0.09	0.09	0.06	0.09	0.09	0.10	0.07	0.07	0.08	0.08	0.09	0.07	0.07	0.08	0.09	0.08
Mg	1.48	1.35	1.49	1.53	1.53	1.61	1.57	1.60	1.47	1.51	1.51	1.56	1.51	1.53	1.51	1.55	1.53	1.58	1.64	1.57	1.53	1.46
Ca	1.85	1.91	1.87	1.86	1.88	1.83	1.86	1.83	1.86	1.88	1.81	1.90	1.83	1.94	1.93	1.91	1.90	1.90	1.85	1.86	1.80	1.84
Ba	b.d.	0.01	b.d.	b.d.	b.d.	b.d.	b.d.	b.d.	b.d.	b.d.	b.d.	b.d.	b.d.	b.d.	b.d.	b.d.	0.01	b.d.	b.d.	b.d.	b.d.	b.d.
Na	0.35	0.31	0.30	0.31	0.28	0.30	0.28	0.33	0.29	0.33	0.35	0.26	0.34	0.31	0.28	0.28	0.32	0.31	0.28	0.26	0.36	0.39
K	0.20	0.25	0.20	0.19	0.20	0.19	0.16	0.16	0.21	0.19	0.21	0.18	0.19	0.20	0.21	0.19	0.18	0.18	0.19	0.17	0.20	0.22
F	b.d.	b.d.	b.d.	b.d.	b.d.	b.d.	b.d.	b.d.	b.d.	b.d.	b.d.	b.d.	b.d.	b.d.	b.d.	b.d.	b.d.	b.d.	b.d.	b.d.	b.d.	b.d.
Cl	0.04	0.04	0.03	0.03	0.03	0.03	0.03	0.03	0.03	0.03	0.04	0.03	0.04	0.04	0.04	0.03	0.04	0.03	0.04	0.03	0.05	0.07
Total cation	15.44	15.51	15.41	15.47	15.43	15.45	15.38	15.43	15.43	15.44	15.48	15.40	15.41	15.43	15.36	15.39	15.41	15.44	15.40	15.44	15.50	15.43

b.d.: below detection limit.

Table S5.

Area	Pluton	Age (Ma)	Error (Ma)	Exposed Area (m²)	Pulse
Mikawa	Kamihara W	**98.9**	**0.8**	52681691	99-95 Ma
Mikawa	Kamihara W	**99.4**	**0.9**	52681691	99-95 Ma
Mikawa	Kamihara E	**96.0**	**1.0**	75405830	99-95 Ma
Mikawa	Kiyosaki	**94.7**	**0.7**	6620551	99-95 Ma
Mikawa	81-75 Ma Hbl-Bt tonalite (Hazu)	**81.1**	**1.0**	10915494	81-75 Ma
Mikawa	81-75 Ma Hbl-Bt tonalite (Hazu)	**81.1**	**1.0**	10915494	81-75 Ma
Mikawa	81-75 Ma Hbl-Bt tonalite (Hazu)	**75.0**	**1.0**	10915494	81-75 Ma
Mikawa	78-75 Ma (Hbl)-Bt granite (Goyu)	**77.6**	**0.6**	7589369	81-75 Ma
Mikawa	78-75 Ma (Hbl)-Bt granite (Goyu)	**77.1**	**0.6**	7589369	81-75 Ma
Mikawa	Tenryukyo	**75.0**	**1.0**	89061024	81-75 Ma
Mikawa	Shinshiro	**69.5**	**0.3**	78345569	75-69 Ma
Mikawa	Shinshiro	**70.6**	**1.0**	78345569	75-69 Ma
Mikawa	Mitsuhashi	**73.2**	**0.7**	30821457	75-69 Ma
Mikawa	Inagawa	**74.7**	**0.7**	469664293	75-69 Ma
Mikawa	Inagawa	**69.2**	**0.5**	469664293	75-69 Ma
Mikawa	Inagawa	**73.0**	**3.0**	469664293	75-69 Ma
Mikawa	Busetsu	**69.5**	**0.4**	340997532	75-69 Ma
Mikawa	Busetsu	**70.9**	**0.9**	340997532	75-69 Ma
Mikawa	Busetsu	**70.8**	**1.4**	340997532	75-69 Ma
Mikawa	Mafic	**71.5**	**1.1**	62488213	75-69 Ma
Mikawa	Mafic	**72.4**	**1.2**	62488213	75-69 Ma
Yanai	Shimokuhara	**105.0**	**3.0**	25152535	
Yanai	Namera	**105.0**	**2.0**	3578271	
Yanai	Soo	**100.6**	**1.0**	9075680	
Yanai	Gamano	**101.0**	**1.9**	163871347	
Yanai	Gamano	**100.0**	**1.0**	163871347	
Yanai	Gamano	**94.7**	**1.0**	163871347	
Yanai	Gamano	**96.2**	**3.0**	163871347	
Yanai	Gamano	**95.3**	**1.0**	163871347	
Yanai	Kibe	**98.0**	**1.0**	14856263	
Yanai	Kibe	**97.6**	**1.0**	14856263	
Yanai	Iwakuni	**95.6**	**1.0**	19197476	

Surface exposure of each pulse is chalculated as a total of surface exposure of each granitoid belonging to each pulses. The pulse names of each granitoids are listed in the 'Pulse' column.

Figure 12 was prepared with data presented in the table above.

Areas: Mikawa area (eastern part of the Ryoke belt); Yanai area (western part of the Ryoke belt)

Pluton: Pluton name following correlations in Skrzypek et al. (2016) and Takatsuka et al. (2018)

Age / Error (Ma): All available U－Pb zircon ages for the plutons considered. References can be found in Skrzypek et al. (2016), Takatsuka et al. (2018) and the present study.

Exposed area (m²): Exposed pluton area is calculated using the seamless geological map of Japan, scale 1: 200,000 (July 3, 2012 version) and for map extents corresponding to those of Fig.1 in Skrzypek et al. (2016) and Fig. 1 in the present study.

Calculation method: For each pluton, all available U－Pb zircon data are used to calculate an age probability density curve assuming a Gaussian distribution for each Age/Error pair. Each curve is then scaled so that its area corresponds to the exposed pluton area. The thick black curve represents the sum of all probability density curves for the individual plutons.

Limitations: Defining the age of a pluton based on a single sample cannot account for age heterogeneity. The assumption that a whole pluton preserves a single age within a 2－3 Ma error seems to be mostly valid, except when several facies are identified (Inagawa granite in the Mikawa area, Gamano granodiorite in the Yanai area). The estimated exposed pluton area is restricted to arbitrary map extents; the actual proportions may slightly vary.